Deliverable 1.24

PI-based Assessment of the Results of WP2-WP4. Ongoing Integration Action

September 2015

Agreement n.:	308974
Duration	November 2012 – October 2017
	DTU Wind

The research leading to these results has received funding from the European Community's Seventh Framework Programme under grant agreement

Document information

Document Name:	PI-based Assessment on the Results of WP2-WP4. Ongoing Integration Action
Document Number:	Deliverable 1.24
Author:	P. Chaviaropoulos (NTUA) G. Sieros, D.Lekou, K. Bacharoudis (CRES) C. Tibaldi, T. Barlas, F. Zahle, H.A. Madsen,F. Rasmussen (DTU) A.B. Abrahamsen (DTU) T. P. Philippidis, G. Roukis (UPAT) A. Croce (POLIMI) D. Kaufer (RAMBOLL) J.A. Armendariz (CENER)
Document Type	Report
Dissemination level	PU
Review:	P. Chaviaropoulos
Date:	September 2015
WP:	WP1: Conceptual Design
Task:	Task 1.2: Assessment of Innovation at the Subsystems Level
Approval:	Approved by WP Leader

TABLE OF CONTENTS

LIST OF FIGURES & TABLES

CHAPTER 1 INTRODUCTION

1.1 Scope and Objectives

The objective of this report is to summarise and evaluate the main innovative concepts proposed by the technical work-packages 2 to 4 for turbines rated at 10MW. The evaluation will prioritize the best innovations on the basis of the performance indicators (PIs) proposed in Deliverable D1.22.

The innovative concepts that are evaluated at the components level comprise:

- Three solutions for blade aerodynamic design (WP2)
- Three solutions for blade structural design (WP2)
- Two different drivetrain solutions, a super conducting and a pseudo direct drive (WP3)
- Two offshore support structure concepts, one for fixed and another for floating substructures (WP4)

The deliverable is concluded with a comparison of the PIs (see D1.22) derived for the proposed innovative concepts against the PIs of the reference design. The emphasis is put on the Levelized Cost of Electricity (LCOE) and its main entries, researched in INNWIND.EU, CAPEX and Capacity Factor. Before any PI evaluation, each concept is assessed for its structural integrity and its cost performance following the procedures described in Deliverable D1.23.

1.2 Overview of the report

In the following ten Chapters we present in detail the individual innovative concepts selected from WPs 2 to 4. In each Chapter there is an introductory section addressing the state of the art and the motivation for researching the concept, a brief description of the concept and the anticipated pros and cons from its application in the turbine design. In the next section we investigate the structural integrity of the proposed solution, starting from the design layout and dimensioning and proceeding to the load cases considered and its structural integrity verification according to the recommendations of Deliverable D1.23. In the next section we appreciate the impact of the proposed design on LCOE. We investigate separately its impact on the Annual Energy Production (AEP), on CAPEX and on OPEX. When relevant, we proceed to an LCOE sensitivity analysis and we conclude its Chapter with some main findings, conclusions and recommendations.

The ten Chapters that follow address the following innovative concepts:

Chapter 2 LOW INDUCTION ROTOR *(Ref WP2, CRES and NTUA)*
The concept, which has been presented in detail in D2.11, suggest the use of a larger, less loaded, rotor as a strategy for increasing the wind turbine capacity factor and reducing the wake losses without burdening rotor and turbine loads. In the present report the LIR concept has been combined with a newly designed family of low-lift airfoils presented in D2.12.

Chapter 3 TWO-BLADED TURBINE *(Ref WP2, DTU)*
The concept has been presented in detail in D2.11 and further researched, combined with an innovative offshore support structure, in D1.32. Using integrated

aero/structural design it is investigated whether a 2-bladed rotor of larger diameter than the reference can substantially reduce the turbine CAPEX without compromising the capacity factor or increasing the support structure loads.

Chapter 4 ACTIVE BLADE CONTROL WITH FLAPS (*Ref WP2, DTU*)

Active flaps are used for load control. In the past decade at DTU the design of such a system has been explored and it is oriented towards flexible elastomer trailing edge geometry, activated by pressure fluid, referred to as Controllable Rubber Trailing Edge Flap. The aeroelastic optimization of the DTU 10MW RWT blade equipped with active trailing edge flaps is carried out using a simple individual flap controller close to industry standards.

Chapter 5 INNOVATIVE INNER BLADE STRUCTURE (*Ref WP2, CRES, UP*)

The redesign of the RWT blade using an internal truss structure instead of the traditional spar-box concept is presented in this section. Two designs are presented using glass-epoxy and carbon-epoxy materials. Noting that the manufacturing cost for the build-up of internal truss structures, including the joints of the truss members is quite uncertain for structures of size, the main expected benefit from the concept is a significant reduction of blade mass.

Chapter 6 BEND-TWIST COUPLED BLADE (*Ref WP2, POLIMI*)

The 10MW RWT Rotor is redesigned employing bend-twist coupling (BTC). BTC is a passive load control strategy where the blade, when loaded, deforms so as to induce aerodynamic load reduction. Passive load mitigation by BTC can be obtained by exploiting the anisotropic mechanical properties of composite materials.

Chapter 7 INTEGRATED BLADE DESIGN WITH BEND-TWIST COUPLING FOR INDIVIDUAL PITCH CONTROLLED ROTORS (*Ref WP2, POLIMI*)

A 10MW BTC blade is designed employing an integrated blade design approach based on constrained optimization. Individual pitch control (IPC) is used in parallel to further mitigate loads. The possibility offered by the synergetic adoption of BTC and IPC of lowering the loads allowed to increase as much as possible the rotor diameter, operation that concerns a worsening of loads, but that has the main goal of increase the energy production.

Chapter 8 SUPERCONDUCTING GENERATOR (*Ref WP3, DTU and DELFT*)

There are two SC generator options considered, the MgB2 option and the RBCO (High temperature superconducting Rare Earth–Barium–Copper-Oxide) one. The high price for the RBCO tape is indicating that MgB2 is most likely the fastest technology to be implemented. It should however be said that RBCO is considered to become the cheapest technology in the long run, because the tapes are produced of little and in-expensive materials, but presently using a very expensive production methods.

Chapter 9 PDD GENERATOR (*Ref WP3, MAGNOMATICS and U-SHEFFIELD*)

A magnetic gear is combined with an electrical machine to realize a magnetically geared drive of high torque density. The magnetic pseudo direct-drive (PDD) generator is realizing the possibility of applying magnetic gears in wind turbines. In a PDD generator, the magnetic gear and the electrical generator are mechanically as well as magnetically integrated.

Chapter 10 BOTTOM MOUNTED OFFSHORE SUPPORT STRUCTURE (*Ref WP4, RAMBOLL*)

The concept has been presented in detail in D4.31 and adopted as the INNWIND.EU 10MW Reference Jacket. Mass and cost functions for this reference have been established. The assessment of the material, welding and assembly costs has been performed in D4.12 which results in a cost saving potential of up to 20%.

Chapter 11 SEMI-SUB FLOATER DESIGN (*Ref WP4, CENER*)

A new conceptual design of a floating platform for a 10MW wind turbine is presented for the first time in the project. It is an asymmetric semi-submersible floater from steel designed for a sea depth of 200m. The concept has been presented in more detail in D4.33. This design is adopted as the INNWIND.EU 10MW Reference Floater.

Following ***Chapters 2 to 11*** with the presentations of the individual innovative concepts there is ***Chapter 12*** where their synthesis and cross-comparison is attempted with emphasis on their impact on LCOE.

CHAPTER 2 LOW INDUCTION ROTOR

2.1 Introduction to the Innovative Concept

2.1.1 State of the art and motivation

The increase in turbine size to levels beyond 10MW is motivated by the drive to reduce the kWh cost for offshore applications. Thereto it should be realized that for offshore applications, the rotor cost as a percentage of the total cost of Energy (CoE) is much less compared to onshore applications. Since the rotor remains the only energy producing component it is possible to increase the energy production by increasing the rotor diameter at a favorable overall cost balance. Moreover, increasing rotor diameter for a constant rated power improves the capacity factor leading to less variability in wind power which is a major advantage for utilities.

As recent developments indicate, for given nominal power this design philosophy leads to: larger diameter, lower solidity and higher tip speed. Such design philosophy leads to long slender blades with thicker airfoils running at high tips speeds. Moreover active and passive flow and load control devices offer interesting design options in order to further reduce load levels that are investigated in a large number of projects.

This is illustrated in Figure 2.1-1 from [1] where calculations performed with a standard design tool indicate that less loaded rotors make it possible to increase the rotor diameter at the same loads giving lower cost of wind energy. Hence these rotors would operate at a lower axial induction factor than 1/3 (i.e. the axial induction factor where maximum power coefficient CP is found). Instead axial induction factors in the range from 0.19 to 0.28 are more optimal from a cost of energy point of view.

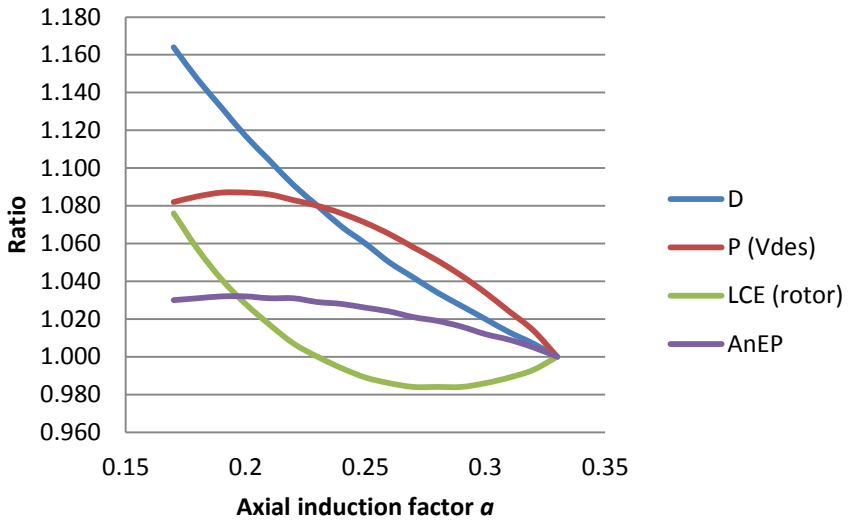

Figure 2.1-1 *Characteristic properties of rotors with the same root bending moment designed for different values of the axial induction factor. Plots are presented for the rotor diameter (D), the power production at design wind speed P (Vdes), the levelized cost of energy (LCE) (rotor contribution only) and the annual energy production (AnEP). All properties are divided by their corresponding reference values (a = 1/3)*

The concept of low induction rotors (LIR) was further assessed in D2.11 "New aerodynamics rotor concepts specifically for very large offshore wind turbines" and presented in [2]. A LIR variant of the INNWIND.EU 10MW RWT was, thus, produced corresponding to an axial induction factor α=0.2 (as opposed to 0.33, typical for Cp_max designs). The resulting blade has a radius increased by 13% and operates at a design CL=0.8, meaning that a new family of airfoils is needed in order to implement the design properly. Such a low-lift family of airfoils has been designed and assessed by the authors as part of their contribution in D2.12 "New airfoils for high rotational speed wind turbines".

Comparison of key performance parameters to the RWT indicated a 3.5% improvement in AEP compared to the RWT, along with a 10% reduction in thrust. Earlier analysis has shown that due to their increased energy capture, at the single turbine but also at the wind farm level, LIRS may be one of the contributing technologies for reducing the levelised cost of energy of large offshore wind farms. Nevertheless, the viability of the LIR concept can only be confirmed through detailed structural designs which will show whether the extra cost of the larger blades and the extra tower cost, due to its increased hub height, are compensated by the increased capacity factor that LIRs promise to deliver in large offshore wind farms.

2.1.2 Brief description of the concept

It is useful to introduce the background for the design that is proposed. We use the standard definitions for Tip-Speed-Ratio (TSR or λ), blade section lift to drag ratio k and the radius fraction x according to Eq. (1). We denote V the ambient wind speed, ω the rotational speed and R the rotor radius and B is the number of blades.

$$\lambda = \omega R/V \qquad k = C_L/C_D \qquad x = r/R \tag{1}$$

We introduce the non-dimensional lift distribution $\Lambda(\lambda,x)$ as

$$\Lambda(\lambda, x) = \frac{c(\lambda, x)C_L}{R} \tag{2}$$

where $c(\lambda,x)$ is the chord distribution and C_L the lift coefficient.

For a pitch-controlled, variable speed HAWT design and for a given rotor radius the classical rotor aerodynamic design problem would seek to maximize the energy capture by maximizing the power coefficient C_P. According to the BEM theory this would happen for an axial induction value α=1/3 and would correspond to a TSR design value λ which gets larger (along with $C_{P,MAX}$) as the aerodynamic performance of the blades k gets better (higher). As design λ increases the non-dimensional lift distribution $\Lambda(\lambda,x)$ gets smaller and, for the same family of blade profiles, the rotor solidity gets lower.

For a variable speed rotor, the design λ value (and therefore $C_{P,MAX}$) can be maintained over a range starting from a minimum wind speed, defined by the low-end capability of the variable-speed power conversion system, up to a maximum wind speed which is limited by the rotor maximum tip-speed, either for restraining noise or centrifugal loading. We shall call this maximum wind speed, where $C_P = C_{P,MAX}$, "design wind speed". Usually, the pitch variable speed turbines have their design wind speed just below their rated speed.

Suppose that we have an initial (reference) wind turbine and we want to add some freedom in our design by redesigning the rotor, letting its radius free, but respecting all

turbine related constrains (the rated rotational speed and power, the hub loading etc). We will assume for simplicity that the new rotor will use the same family of airfoils (same *k*, considering Reynolds number effects as secondary at the scale of our interest).

Let R_0 be the initial rotor radius and let subscript "0" denote the reference design, the one with α=1/3 corresponding to maximum C_P. The new design problem is formulated as:

$$\frac{C_P(\lambda,\alpha)\cdot R^2}{C_{P0}(\lambda_0,\alpha_0)\cdot R_0^2} \rightarrow max, \quad subject\ to\ \frac{C_M(0)(\lambda,\alpha)\cdot R^3}{C_{M0}(0)(\lambda_0,\alpha_0)\cdot R_0^3} \cong 1 \qquad (3)$$

That is: "maximize the power output up to the design wind speed without exceeding the initial aerodynamic root blade moment". By eliminating the radius dependence the optimization problem (3) can be recast as:

$$\frac{C_P(\lambda,\alpha)}{C_{M(0)}(\lambda,\alpha)^{2/3}} \rightarrow max \qquad (4)$$

The solution of the optimization problem (4) for α, given $\lambda=\lambda_0$, is shown at the right of Figure 2.1-2. The resulting value is α=0.187. As a result, the optimal rotor will have a larger radius; will capture more energy at its design conditions; and will be less loaded than the initial one (design C_T and $C_{M(r)}$ will be smaller), operating at a lower axial induction value α~0.20 instead of α_0=0.33. In other words, we can sacrifice C_P in order to increase energy capture with a larger rotor diameter, while maintaining the aerodynamic bending moments at their initial level. This is feasible thanks to the special shape of the C_P and $C_{M(0)}$ curves, where moving a little left from the optimum α at the C_P curve the power coefficient loss is milder than the corresponding reduction of bending moments in the C_M plot.

This analysis summarizes the justification for moving to higher tip speeds and larger diameters for the proposed design.

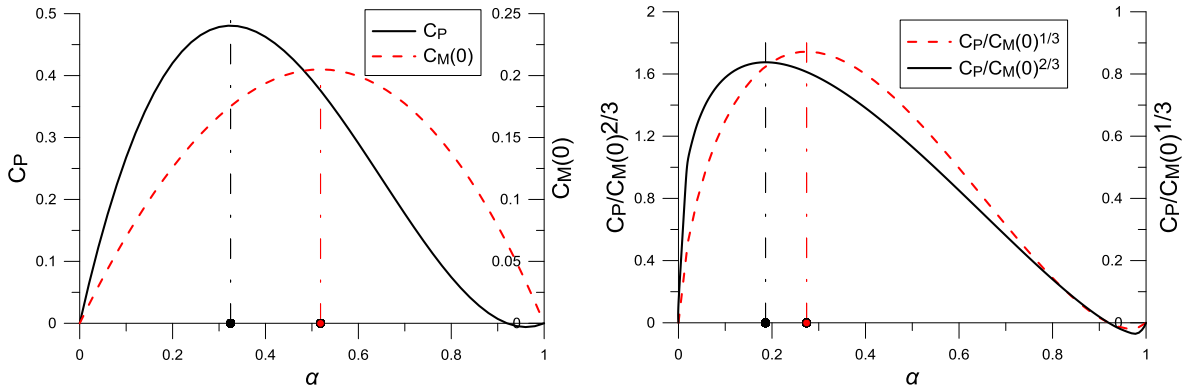

Figure 2.1-2 Plots of non-dimensional coefficients, candidates for blade optimization, versus axial induction coefficient α

2.1.3 Anticipated PROS and CONS

The LIR design assumes chord and thickness distributions which are quite close to those of the RWT 10MW blade. This makes sense as long as the maximum blade root flapping

moment is maintained. Then, a first thought is that by stretching the blade by an R/R_0 (= 1.13) factor and maintaining the reference sectional properties the normal stresses due to bending would be unaltered, ensuring the structural integrity of the new design. Nevertheless, things are not that simple. Apart from possible local buckling failures, such a blade stretching would increase its mass by R/R_0, increase its maximum tip deflection by $(R/R_0)^2$ and reduce its natural frequencies by $1/(R/R_0)^2$. The later would change significantly the dynamics of a large blade getting, in this case, its first natural frequency down from 4P close to 3P. The significant increase of the maximum blade deflection is also problematic. To remedy both problems one should increase the LIR blade stiffness and a possible way for doing so is, in this case, to replace the glass spar of the InnWind.EU RWT with a carbon spar. This would definitely increase the cost of the blades more than the anticipated linear increase by R/R_0. The possibility of slightly increasing the blade chord is still an option for reducing mass and increasing the stiffness, this however would put more pressure on the aerodynamic performance.

Earlier analysis has shown that due to their increased energy capture, at the single turbine but also at the wind farm level, LIRS may be one of the contributing technologies for reducing the levelised cost of energy of large offshore wind farms. Nevertheless, the viability of the LIR concept can only be confirmed through detailed structural designs which will show whether the extra cost of the larger blades and the extra tower cost, due to its increased hub height, are compensated by the increased capacity factor that LIRs promise to deliver in large offshore wind farms.

To proceed to a proper evaluation of the concept we therefore had to design not only aerodynamically but also structurally and re-evaluate its cost. For the reasons mentioned above the LIR blade is a hybrid design with carbon spar and glass skin. This design is presented and structurally assessed in the following section.

2.2 Assessment of the Structural Integrity of the Proposed Design

2.2.1 Design layout and dimensioning

Aerodynamic design of the LIR blade

The design of the blade planform, for a given airfoil family, requires the derivation of chord, thickness and twist distributions that result in optimum energy yield for the wind turbine. The reference blade was used as a starting point for the design and the constrains imposed on the new design were as follows:

- The length of the blade is increased, with a radius of 100.75m, keeping the same rotating speed.
- The thrust is constrained to remain less or equal to the thrust of the reference blade ($T \leq T_{ref}$), keeping the tower bending moment levels in check.
- Bending moment at the root blade is constrained in a similar manner ($M_{root} \leq M_{root-ref}$), so as to keep the loads on the blade similar to the reference blade.
- The maximum torque is also constrained not to exceed the reference value.

The result is a low induction blade, with reduced power density, but similar loads to the reference design. For the derivation of the optimum planform design a constrained optimization problem is setup, where the free variables are:

- Chord length at 3-4 different positions along the span. In this case a distribution that is very similar to the reference blade is used with identical values for maximum chord and root diameter in order to simplify the structural design.
- Blade twist value at 3-4 different positions along the span.
- Blade thickness and position where thickness switches to minimum value.
- Design Tip Speed Ratio. This is used to define the operating schedule for the wind turbine before pitching.

For the optimization problem a typical BEM method is used, calculating the operating envelope from cut-in to cut-off wind speeds. The resulting power is weighed based on the probability for a Weibull function with (c=10.38, K=2.0 – reference values). The objective function is then the capacity factor for the given wind conditions.

Optimization is performed using an evolutionary method to calculate optimum values for the free variables. The resulting blade shape is shown in Figure 2.2-1 (top). For the same planform design two different airfoil geometries were used, the original FFA airfoils and optimised airfoils, as shown in Figure 2.2-2. The resulting optimum twist distribution for all cases is shown in Figure 2.2-1 (bottom).

The new airfoils have been designed to exhibit maximum L/D at lower lift values (Figure 2.2-3), so as to be better suited for the low induction rotor.

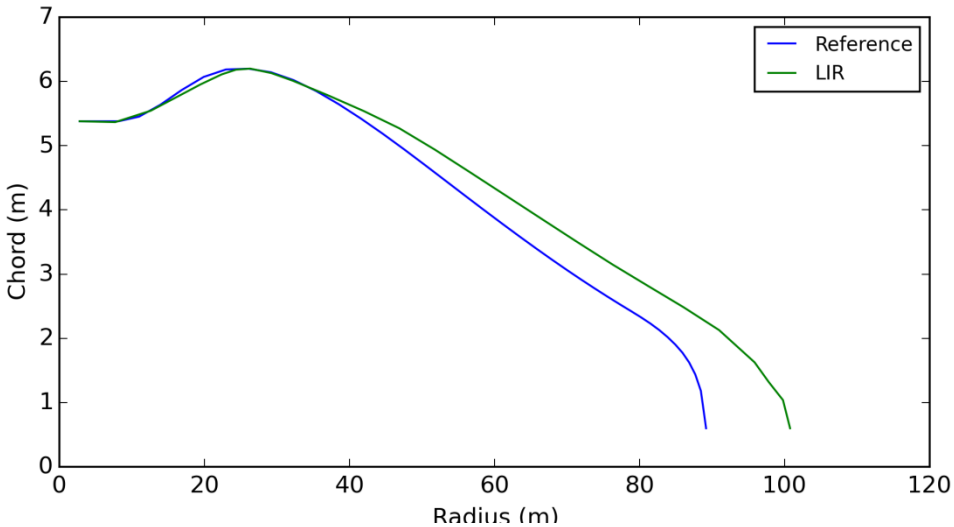

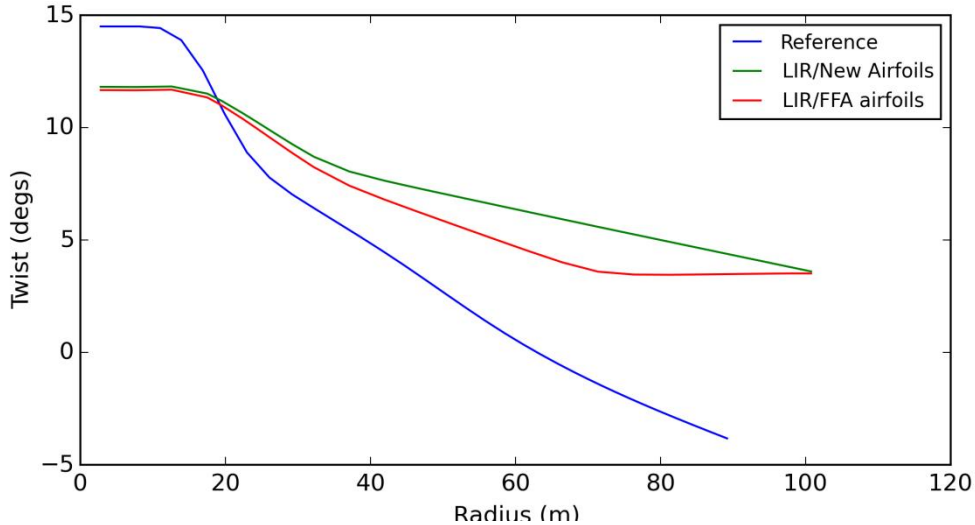

Figure 2.2-1 Planform characteristics of the LIR designs. Chord (up) and twist (down) distributions

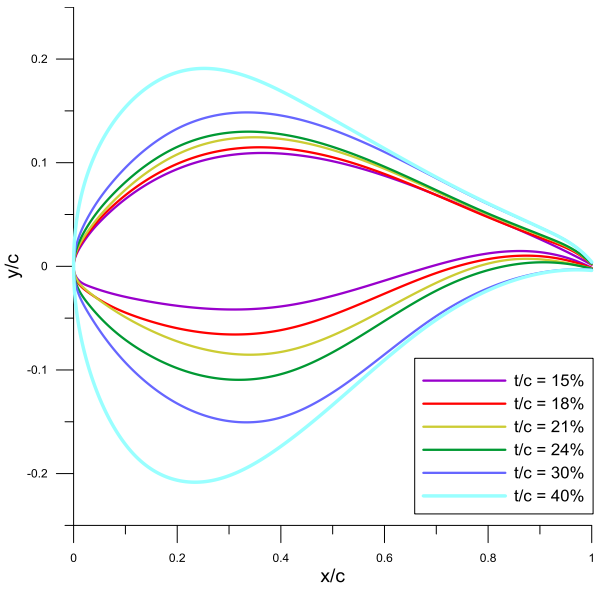

Figure 2.2-2 The 10-90/20-80 Low Lift family profiles used in the present LIR design [3]

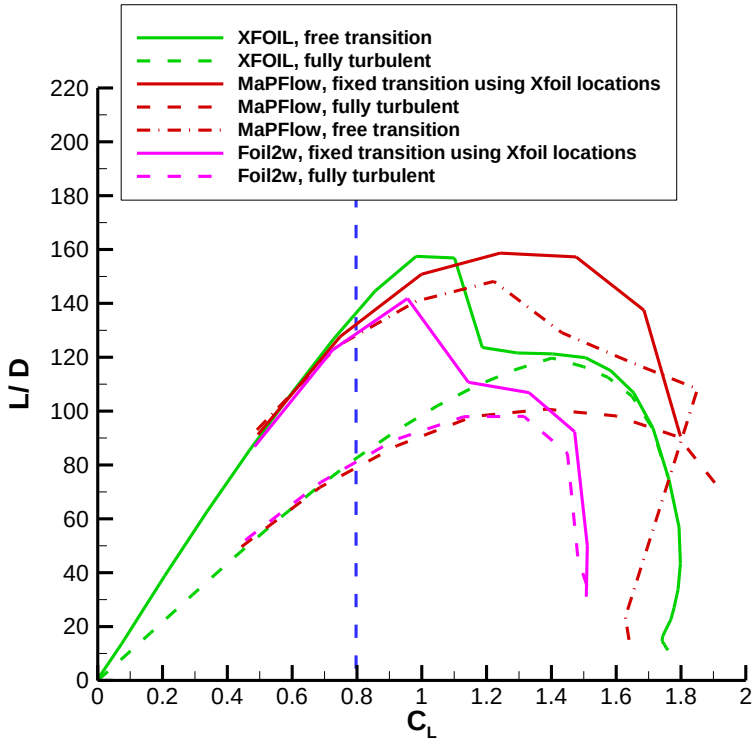

Figure 2.2-3 Performance (L/D) of the 24% LL 10-90 airfoil for transitional and fully turbulent flow conditions. The (more conservative) RANS results obtained with MaPFlow [3] are used in the present context

Structural design of the LIR blade

For the structural investigations performed the LIR blade is based on the geometric characteristics of the reference INNWIND.EU blade. To match the aerodynamic design the modification concerned the prolongation of the z-axis node coordinates (along the blade length) of the reference blade by a factor of 1.13 resulting in a new blade of 100.758 m (LIR blade).

The design of the LIR blade complying with the structural integrity requirements (as described in the following) was achieved with the introduction of carbon uniaxial layers on selective locations along the blade length to improve the stiffness of the blade keeping at the same time the mass of the blade as low as possible. Additionally, glass fibre layers with 90° fiber orientation in relation to the blade axis were introduced mainly on the suction side of the blade to increase strength against transverse stresses.

2.2.2 Load cases considered (from D1.23) and Results Obtained

The loading of the LIR blade was estimated by the reference wind turbine blade loading, as this was used during the benchmark exercise within INNWIND.EU WP2. Following the aerodynamic design of the blade the solution to be acceptable for the reference wind turbine would mean that the root bending moments for the longer blade would be kept the same as the reference blade. Therefore, for deflection and strength estimations the LIR blade was subjected to 13% lower concentrated aerodynamic loads in both the edgewise and flapwise directions.

2.2.3 Structural integrity verification

To verify the suitability of the blade design for the wind turbine, as well as to verify the structural integrity, modal analysis, static strength analysis and buckling analysis were performed. The constraints set in order to have a feasible solution for the reference 10MW wind turbine, were as follows:

Dynamic behaviour	natural frequencies of the blade were to be as close as possible to the reference wind turbine blade. Avoidance of the 6p, 9p, etc. frequencies of the reference wind turbine.
Stiffness, Strength	Stiffness and strength of the LIR blade should be comparable to the reference blade.
Elastic stability	The LIR blade should perform comparable to the reference blade or even better. The loading applied to verify the structural design against elastic stability is considered the same extreme load case scenario as that used for the verification of stiffness and strength.

The analysis procedure used to verify the structural integrity of the blade was identical to that used in the benchmark study. The results of the analysis tools for the reference blade were compared with that of the other partners. Still in order to assure validity of results, the output data from the structural analysis procedure are compared against those of the reference wind turbine blade. For reference purposes, modal, stiffness and strength analysis, as well as elastic stability estimations were performed using finite elements commercial code NISA II/EMRC, while the blade model comprised of shell elements suitable for modelling multi-layered composite materials.

The results of the final solution proposed are presented in the following.

Modal analysis: The first six natural frequencies of the blade are presented in Table 2.1. It is clear that all the calculated frequencies of the LIR blade are close to the ones of the reference INNWIND.EU blade with the LIR blade frequencies however to be below the reference blade frequency values (except for the first natural frequency which are equal).

Table 2.1 - Natural frequencies of the blade (all frequencies in Hz)

Mode No.	LIR blade	INNWIND.EU blade
1	0.640	0.640
2	0.897	0.959
3	1.807	1.849
4	2.686	2.863
5	3.644	3.763
6	5.469	5.824

Results of the tip displacement in the x (edge) and y (flap) direction can be seen in Table 2.2. The LIR blade is stiffer both in flap- and edge-wise direction comparing with the reference blade.

Table 2.2 - Tip deflection

Blade	Ux (edge) [m]	Uy (flap) [m]
LIR	1.817	15.556
INNWIND.EU	2.322	18.529

Strength analysis was performed calculating the Tsai-Wu failure index. Contour plots of the maximum Tsai-Wu value among the various layers for every element is presented in Figure 2.2-4 for both sides of the rotor blade (pressure and suction side). Critical part of the blade comprises the suction side especially in the spar cap, see Figure 2.2-4d. More specifically, the Tsai Wu failure index for the elements from 38.79 m to 61.30 m from the blade root varies between 1.09 and 1.11. The failure mode is related to the failure of the carbon layers in the fiber direction. Reminding that the INNWIND.EU reference blade indicated a maximum Tsai-Wu failure index equal to 2.756 (using CRES calculations), the current blade design is considered adequate.

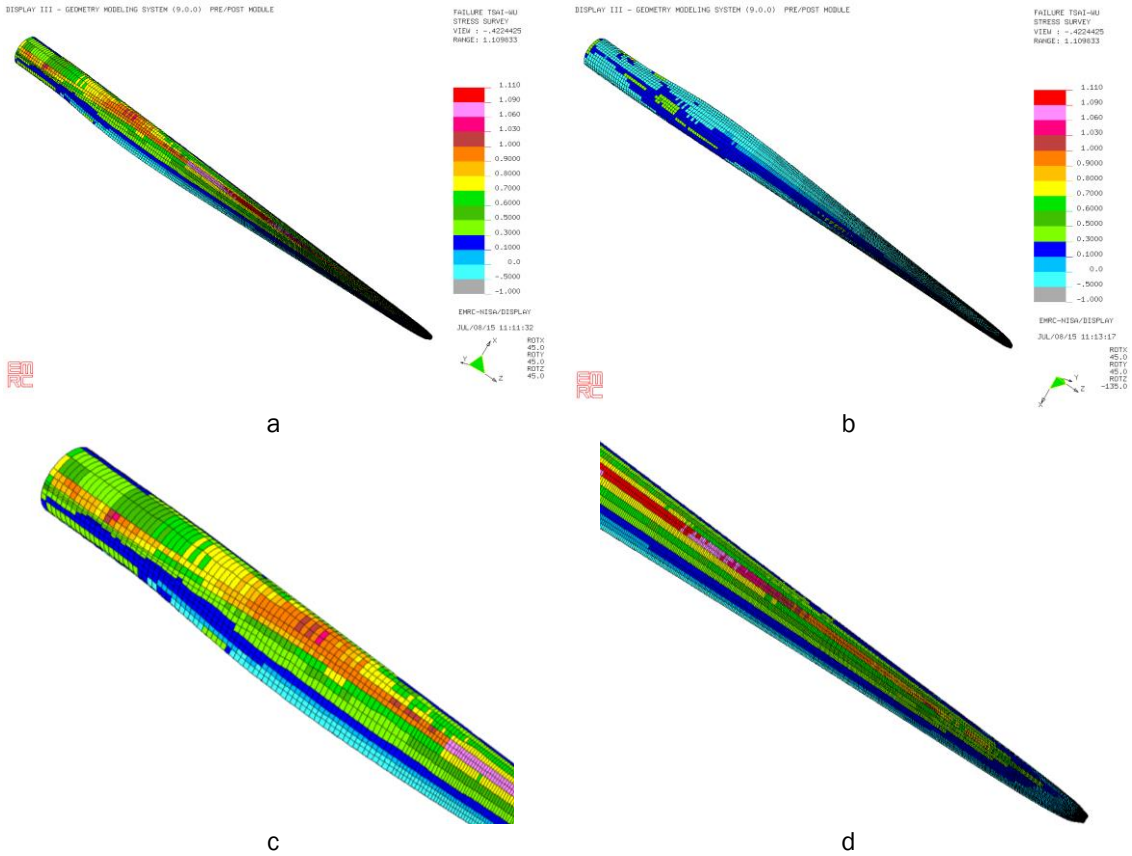

Figure 2.2-4 Tsai-Wu failure criterion a) at the suction side b) at the pressure side c) a detail in the inboard part of the suction side d) a detail in the outboard part in the suction side of the LIR blade

Buckling analysis was performed considering safety factors for the stiffness properties of the glass and carbon fabrics as also done within the benchmark. More specifically, the values of the stiffness properties were divided by a factor 2.042. The value of the factor was adopted following GL requirements. The first critical buckling load factor was calculated equal to 0.97 while the respective eigen-mode is presented in Figure 2.2-5. The

critical location comprises the suction side of the blade, see Figure 2.2-5b, as well as the shear webs (A & B), see Figure 2.2-5c. More specifically, buckling is observed in the spar cap of the blade root and in the spar cap, leading and trailing panels in the outboard part (near the tip) at the suction side of the blade. Moreover, the shear webs in the outboard part (near the tip) of the blade also buckle. Regarding the failure in the outboard part, it should be said that concentrated forces of high value were applied at this location in the FE blade model and thus the respective failure mode correspond to this modelling defect. A direct comparison with the reference blade (buckling load factor 0.875) indicates that the LIR blade is quite adequate considering elastic stability.

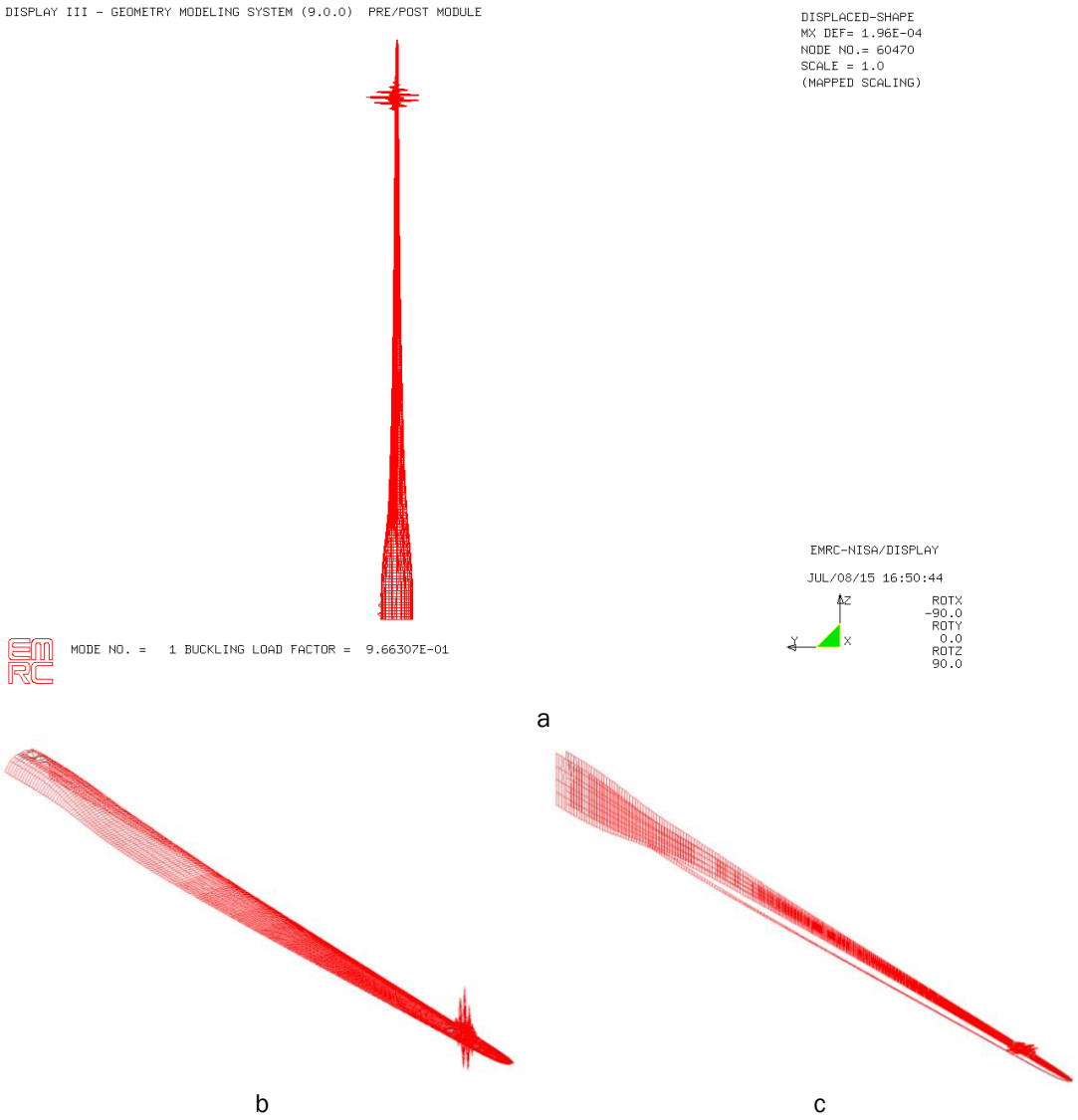

Figure 2.2-5 First eigen-mode of the LIR blade a) left side b) suction side c) shear webs (A & B & C)

The design of the LIR blade that complies with structural integrity requirements resulted in a blade which mass (as well as the mass of the carbon layers used in the lamination schemes) are shown in the first two columns of Table 2.3. In the same table, the center of gravity for the whole blade is also superimposed while a comparison with the reference blade is also performed. The z axis corresponds to the axis along the blade, x axis corresponds to the in-plane blade axis and y to the out-of-plane blade axis, following the

global coordinate system introduced in the benchmark of the structural analysis tools within INNWIND.EU project. It is highlighted that the new blade design is heavier compared to the reference one about 2415 kg while the ratio of the carbon-layer mass to the overall blade mass is 15.92%. Concerning the spar caps, the mass of the carbon layers is 6332.5 kg close to the mass of the unidirectional glass fabric (6477.95 kg).

Table 2.3 - Global blade properties

Blade	Overall mass [kg]	Carbon [kg]	C.G. z [m]	C.G. x [m]	C.G. y [m]
LIR blade	44785.90	7127.89	31.69	-0.21	0.11
INNWIND.EU blade	42371.20	---	28.80	-0.16	0.04

It can be concluded that the introduction of carbon fabrics permits an efficient design of a 100 m rotor blade with respect to modal, stiffness, strength and buckling analysis. At the same time, the mass of the blade was kept in low values, increased only 5.6% in comparison to the mass of the 90 m INNWIND.EU reference blade design.

2.3 LCOE Impact of the Proposed Design

2.3.1 Effect on Annual Energy Production

Wind turbine capacity factor

The wind turbine capacity factor calculated for LIR as a result of its planform optimization procedure is 0.545. This is 7.5% higher than the capacity factor of RWT which for the reference wind speed Rayleigh distribution with 9.2m/s mean is 0.507. Notable is the fact that when the same planform optimization is attempted with the original 10MW RWT high lift FFA profiles, the capacity factor would be 0.530 corresponding to a 4.5% improvement compared to the RWT. Thus, from the total 7.5% wind turbine capacity factor increase 4.5% comes from the LIR concept and another 3.0% comes from the use of dedicated low lift airfoils. The improvement of AEP is a consequence of the increased LIR energy production below rated wind speed (see Figure 2.3-1).

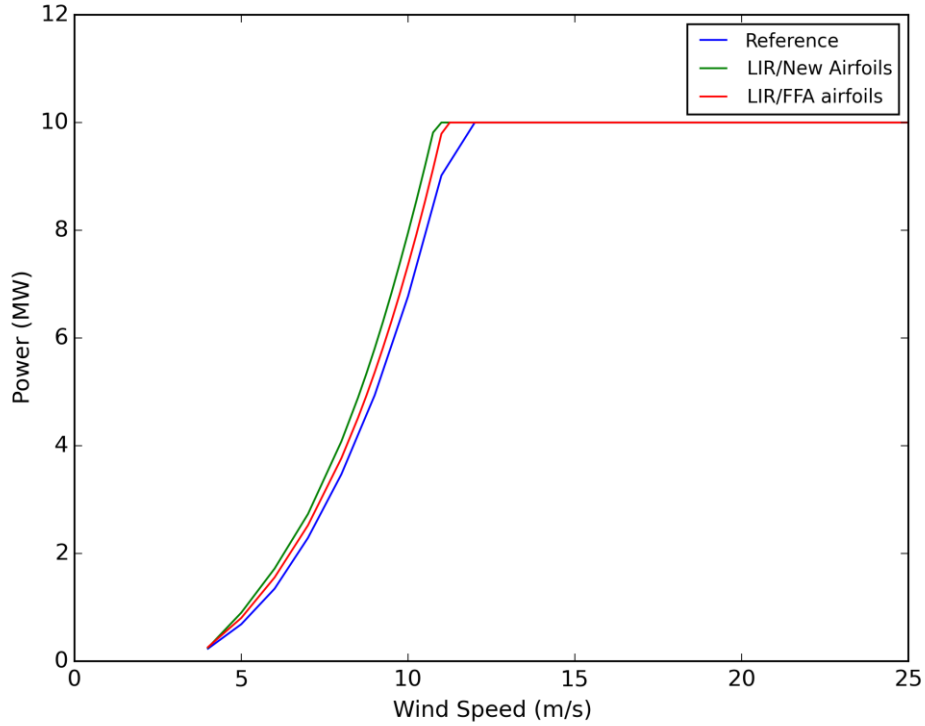

Figure 2.3-1 Power Curves comparison, LIR against RWT. The LIR designs are considered, one with the original FFA profiles and one with the newly designed low lift profiles

Wind farm wakes

As already discussed in [4], LIRs are operating with reduced wake losses due to their lower thrust coefficients. The calculations presented in [4] support a reduction of the wind farm wake losses from 9% for the RWT to 7.5% for LIR, an improvement which directly reflects to the wind farm capacity factor as well.

Other wind farm losses including availability losses

We do not expect the LIR to affect the reliability of the turbine and, therefore, its availability losses.

2.3.2 Effect on CAPEX

Using a LIR instead of the original one of the 10MW RWT is affecting the CAPEX of the following turbine subcomponents

Blades

As already discussed the need for stiffening the longer blade of the LIR to limit its maximum deflection and trim its natural frequencies is satisfied by replacing the original all-glass blade with a hybrid one with carbon spar. This necessitates the development of a cost model for hybrid blades, given the fact that carbon fibre is three times more expensive than glass fibre.

The cost-model used is weight-based and is based on the combination of the cost model developed within INNWIND.EU [5] as well as the findings of [6]. The method involves the estimation of the **baseline cost** of a full glass blade, as per [5] and then correcting the cost estimation by the ratio of carbon fibre cost over glass cost. In this method it is assumed that the manufacturing methodology is kept the same for the glass and the hybrid blade. Although not completely true, the technological development in manufacturing technology does allow the assumption of keeping the same manufacturing cost.

In setting up the cost model the various terms entering the cost of the blade as presented in [7]. The addition of carbon fibre in the blade (or replacement of glass fibres) changes the material cost involved, while leaving unaffected the costs of labour, tooling, etc. Ref. [7] reports the change of the material cost depending on the size of the blade. The larger the blade the larger the ratio of the material cost in the cost budget. From data of the said reference a linear estimation has been made to enable prediction of material cost ratios over different sized of blade: The empirical equation used is:

*Material cost (%) = 0.18*length +25.3*

Yet, introducing carbon fibres in the blade does not affect all material cost, but only that part that is replacing the glass fibres. Therefore, the cost of adhesives, sandwich cores, etc. will remain unaffected. In [7] it is estimated that the percentage of fibres within the weight of the blade is about 60%.

The weight of the carbon fibres in the blade can be estimated using the mass reported for the carbon/epoxy composite within the blade and assuming that the volume fibre ratio (V_f) is ranging from 55% to 60% (for the unidirectional carbon epoxy and based on the material properties). With this knowledge the ratio of the carbon fibres over all fibres can be estimated.

Applying the above to the data one has:

*Baseline blade cost: 13.084*44785kg-4452.2 = 581,515$ (2002)*

It should be noted that CRES has estimated a weight for the reference blade of 42371.20kg instead of the 41716kg reported for the reference wind turbine. Therefore, a correction for the weight estimation is done multiplying mass data by 0.985. Correcting the baseline blade cost the blade cost assuming all glass manufacturing is 572,454$ (2002).

The material cost ratio estimated for a rotor of 100.758m is: 43.44%

From the carbon layer mass provided the carbon fibres are estimated to 4704.4 kg, leading to a ratio over the whole blade mass of about 10%. When recalculating to percentage of fibres, the carbon fibres used comprise the 17.5% of the total fibres.

Moreover, it is assumed that the carbon fibres cost 3 times as much as the glass fibres.

Based on the above, the correction factor to be applied on the baseline cost estimated is:

(1-0.4344)+0.4344(1-0.6)+0.4344*0.6*(1-0.175)+0.4344*0.6*0.175*3 = 1.09*

Therefore, the cost of the hybrid glass/carbon blade is calculated to: ***624,675$ (2002).***

Tower

The LIR blade is 13% longer than the RWT one. To maintain the blade-platform clearance of RWT we need to increase the turbine hub-height by 13%X90m = 11.7m. Fortunately, the LIR maximum thrust is decreased by 10% compared to the RWT implying that the tower bottom thrust bending moment is maintained and therefore the static loads of the lower tower and the offshore support structure remain unaffected. These extra 12 meters of tower are assumed to burden the tower weight by the weight of a 12m cylinder having the same cross section with the RWT tower-top section. That increases the tower mass by:

Mass_tower_extra = 12(m) linear_mass_tip_section (kg/m) ~12*3 000=36 000 kg*

The new tower cost is calculated for its revised mass using the existing cost model. The cost of the LIR tower is 2.41 M€ (5% increase) compared to 2.29 M€ of the RWT.

Offshore Support Structure

We have demonstrated that the static loads of the offshore support structure are not changing due to the combined effect of larger tower and reduced rotor thrust. Increasing the tower height will lower the first system natural frequency and this will have an impact (positive or negative) on fatigue loads. A detailed investigation of this effect is beyond the context of this report.

Other components

There is a small influence of LIR to other components CAPEX, such as the low speed shaft or the yaw mechanism due to the increasing rotor size. These extra costs are automatically taken into account by the INNWIND.EU cost model [5].

2.3.3 Effect on OPEX

Direct O&M costs, expressed in (€/kW/y) units are not affected by the introduction of LIR. At the same time we do not anticipate any LIR consequences on the turbine availability. Therefore, the replacement of the reference rotor with the LIR doesn't have any positive or negative effect on OPEX.

2.4 LCOE Sensitivity Analysis

The comparison of LIR against the RWT in terms of key Performance Indicators is presented in the following Table.

ROTOR	Blade Mass (tn)	Blade Cost (k€)	Overall CAPEX (k€)	Turbine CF	Wind Farm CF	LCOE (€/MWh)
RWT - 10MW	42	448	31000	0.507	0.430	91.93
LIR – 10MW	45	517	32090	0.545	0.469	86.37

This corresponds to a 6% reduction of LCOE from its reference value 91.93 to 86.37 (€/MWh). The main uncertainty that may affect this figure is the connected to the LIR blade cost. The sensitivity of LCOE to the blade cost expressed as a multiple (1.0 to 1.4) of the cost of the reference blade is presented in Figure 2.4-1. It is seen that even if the LIR blade costs 40% more than the RWT blade, LCOE becomes 87.33 (€/MWh) corresponding to a 5% reduction of its reference value. This is due to the fact that in offshore wind energy the rotor CAPEX attributes a very share to the cost of wind electricity.

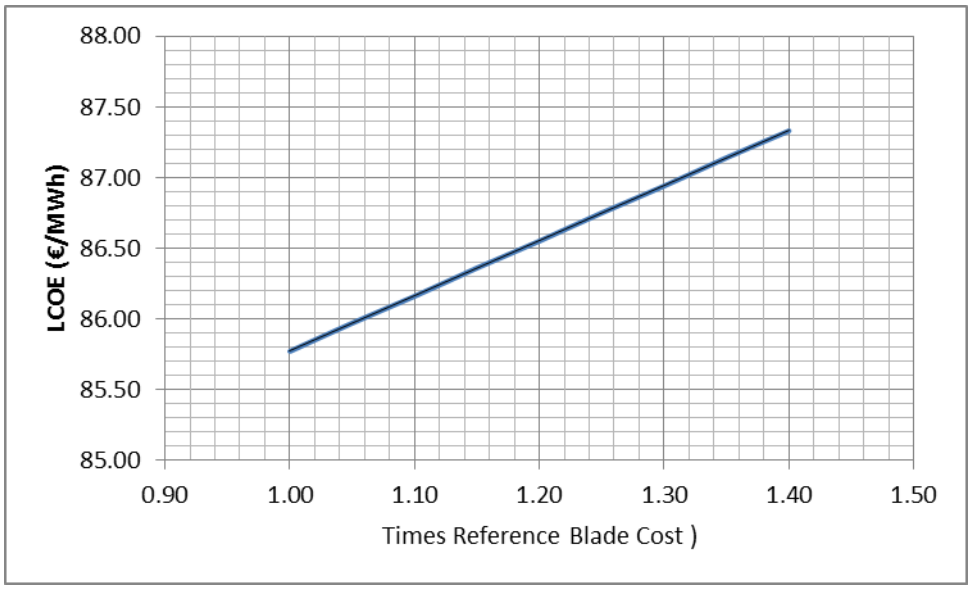

Figure 2.4-1 LCOE sensitivity on LIR blade cost expressed as a multiplier of the RWT blade cost (448 k€)

2.5 Conclusions and Recommendations

A 10 MW Low Induction Rotor has been designed aerodynamically and structurally. The rotor is tested on the 10MW RWT of INNWIND.EU. A hybrid glass-carbon has replaced the original all-glass blade of the RWT. The LIR is 13% longer and the hybrid design aims in increasing the extra requirements for stiffness and strength dye to the larger span. The hybrid blade:

- Has an 8% larger mass than the RWT blade
- Costs 15% more than the RWT blade
- Has a wind turbine capacity factor 7% higher than the RWT blade
- Yields a wind farm capacity factor 9% higher than the RWT blade due to the reduced wake losses corresponding to the lower thrust coefficient of the LIR

Although the turbine CAPEX increases by 4% the overall effect of LIR on LCOE is quite positive reducing it by 6%. The sensitivity of LCOE to the blade cost is relatively low. It is shown however that if a new LIR blade can be designed with the same cost of the RWT blade the LCOE would drop at 85.77 €/MWh.

CHAPTER 3 TWO-BLADED DESIGN CONCEPT

3.1 Introduction

A concept previously investigated in the INNWIND.EU project is the two-bladed concept, both upwind and downwind [8]. The designs of [8] created by a simple scaling of the chord by a factor of 1.5 and a scaling of the material thicknesses of 2/3, resulting in equivalent aerodynamic characteristics but with a factor 2.25 greater stiffness.

In this work we revisit these concepts, and explore the possibilities of increasing the annual energy production by stretching the rotor. The exercise is thus to design new rotors staying within the load envelope of the original DTU 10MW RWT rotor, so the same platform can be used. Since the flap wise stiffness of the two bladed rotor scales with a factor of 2.25 compared to the equivalent three-bladed rotor, an increase in rotor diameter should be possible without violating tip deflection constraints. A simple stretching of the rotor will however lead to greater planform area, thus increasing extreme loads. The stretched design will therefore have to be more slender to stay within the loads envelope.

3.2 Models and Framework

To accomplish designs adhering to the many both geometric and loads constraints, the blades are designed using numerical optimization. The multi-disciplinary wind turbine analysis and optimization tool HawtOpt2 is utilized, in which the aerodynamic shape and structural design are optimized simultaneously tailoring the design aero-elastically to meet the constraints [9]. The HawtOpt2 tool uses OpenMDAO (Open-source Multidisciplinary Design, Analysis, and Optimization Framework [10] to handle the definition of the optimization problem, workflow, dataflow and parallelization of simulation cases. OpenMDAO provides an interface to PyOpt, which has wrappers for several optimization algorithms, and in this work, the gradient-based sequential quadratic programming optimizer SNOPT is used. The tool uses the blade aerodynamic and structural geometric parameterization defined in the open source framework FUSED-Wind [11].

Interfaces have been developed to connect the optimization framework to the finite element cross sectional tool BECAS and to the aeroelastic tool HAWCStab2, that form the core of the analysis capability provided by the tool.

BECAS is used to compute the cross sectional structural and mass properties of the blade, as well as for computing stresses and strains based on extreme loads. The tool is based on a 2D finite element formulation that allows for an exact geometrical description of the section.

The linear high-order aero-servoelastic model implemented in HAWCStab2 uses an unsteady blade element momentum (BEM) model of the rotor and a geometrically non-linear finite beam element model to compute steady-state aerodynamic states, structural deflections and linearized models of the wind turbine. A detailed description of the model is provided by Hansen [12].

A method to evaluate fatigue damage based on a linear model has also been developed recently. The method is frequency based and does therefore not require time domain

simulations, which for gradient-based optimization is central, since the stochastic nature of time-domain simulations with turbulence does not allow for accurate evaluation of gradients of objectives and constraints with respect to the design variables. The method is described in details by Tibaldi et al [13].

A key feature of the tool is that the aero-structural design is solved using a fully coupled monolithic approach in which the aerodynamic and structural design variables are solved for simultaneously enabling detailed aero-elastic tailoring of the blade. Figure 3.2-1 shows a so-called Extended Design Structure Matrix (XDSM) of the workflow. In the present design study fatigue loads were not evaluated or constrained, but included here for completeness.

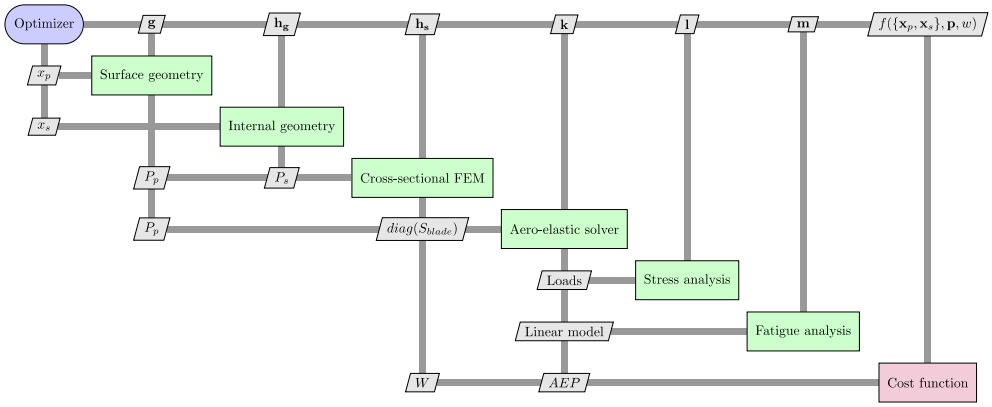

Figure 3.2-1 Extended Design Structure matrix of the aero-structural solution process

3.3 Design Cases

A family of designs are explored in this work with successively increased blade lengths with R = [1., 1.04, 1.08, 1.12] * R_ref, and RPM_max = RPM_max-ref. For the designs where the radius is increased the tip speed will thus increase. The numerical optimization problem that is solved seeks to maximise annual energy production (AEP) while also minimising blade mass. Since these two objectives are conflicting, a pareto front of designs are created to identify the design that best leverages these two objectives.

The design is subject to a number of constraints, the most important listed below:

- Chord < 1.5 * chord_3B-ref
- Relative thickness > 24 %
- Downwind tip deflection @ rated < 1.25 * tip deflection 2B_up @ rated
- Downwind tip deflection @ extreme wind < 1.25 * tip deflection 2B_up @ extreme wind
- Thrust @ rated < T_3B_ref
- Mx_BladeRoot @ rated < 1.5 * Mx_3B_ref
- Mx_BladeRoot @ 70 m/s < 1.5 * Mx_3B_ref
- Cl_oper < 1.35
- Max strain failure index < 1.

The design variables consist of both outer shape and structural geometric parameters:

- Tip speed ratio
- Chord
- Twist
- Relative thickness
- Material thicknesses:
  Spar cap
  Trailing panels
  Trailing edge
  Leading panels
  Leading edge
- Spar caps widths and positions

The total number of design variables was 67. In the present conceptual study realistic constraints were not placed on material thicknesses, which were thus allowed to be reduced below the thickness of one ply. Also note that there is no constraint on the upwind flapwise deflection of the blade, which occurs during shutdown. A preliminary study showed that the upwind deflection at shutdown is approximately equal to the downwind deflection at rated wind speed, which with the above constraints on the tip deflection should be sufficient to maintain tower clearance.

3.4 Results

For each design candidate a number of optimizations with varying weight towards either mass reduction of AEP increase were carried out. In the results presented in the following only the designs with high bias towards energy production will be presented. Figure 3.4-1 and Figure 3.4-2 show the increase in AEP below 14 m/s and the blade mass as function of blade length relative to the reference length of 86.366 m.

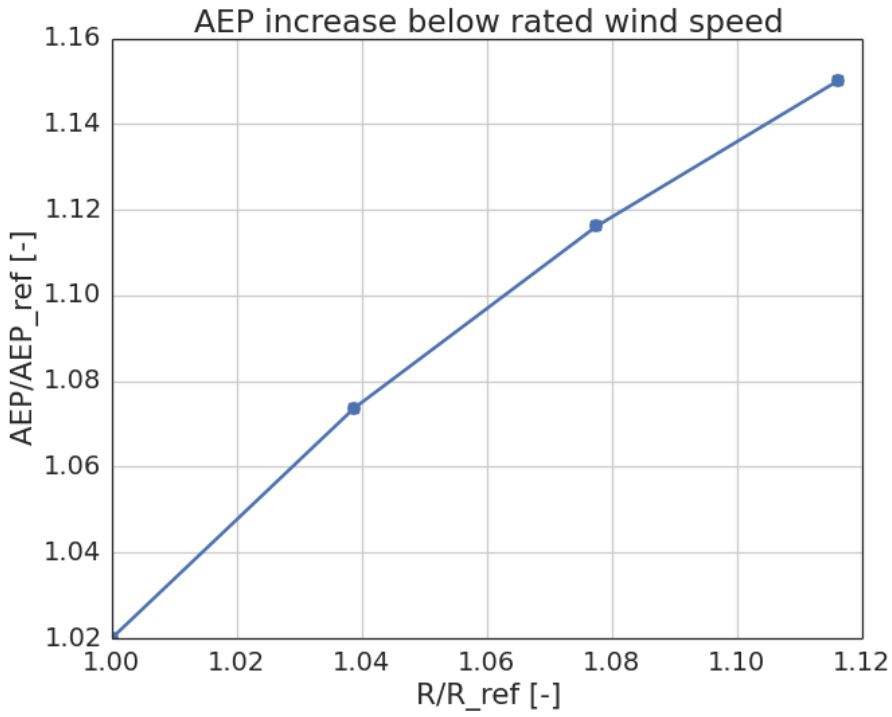

Figure 3.4-1 Increase in annual energy production (AEP) as function of blade length.

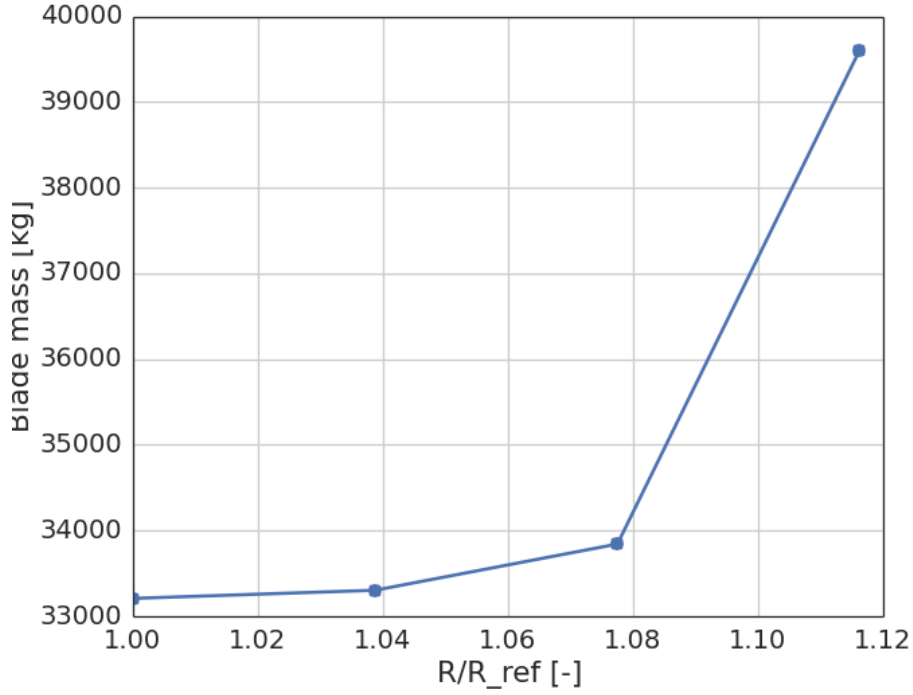

Figure 3.4-2 Blade mass as function of blade length.

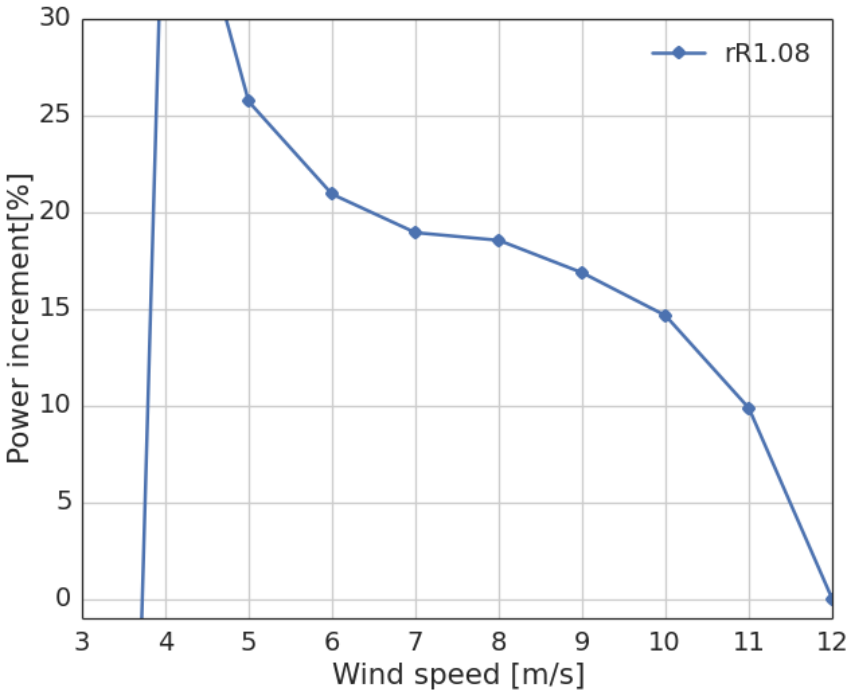

Figure 3.4-3 Power increment of the rR1.08 design relative to the 2B_ref design.

All the stretched designs converge towards an increased tip speed ratio, which is partly driven by the need to avoid hitting the gearbox torque limit, with the rR1.08 design operating at a 16% increased TSR of 8.68. The design with a blade length increase of 8% can achieve an increase in below rated AEP of almost 12%, and almost 23% decrease in the blade mass to 33.7 tonnes from 44 tonnes respecting all the constraints. Figure 3.4-4 to Figure 3.4-7 show the blade planform of the rR1.08 and rR1.12 designs. The optimized blades have a significantly more slender planform towards the tip and a significant reduction in relative thickness on the inner part of the blade due to the increase in allowed tip deflection. The twist distribution of the blade shows a large offset of over four degrees at the tip.

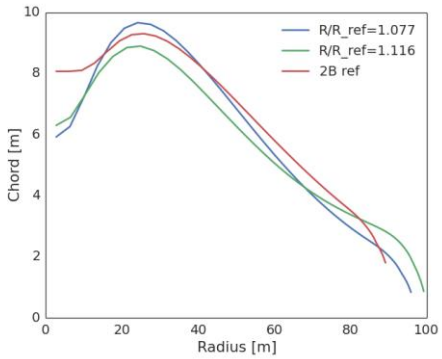

Figure 3.4-4 Chord distribution for the rR1.08 and rR1.12 designs compared to the 2B reference design.

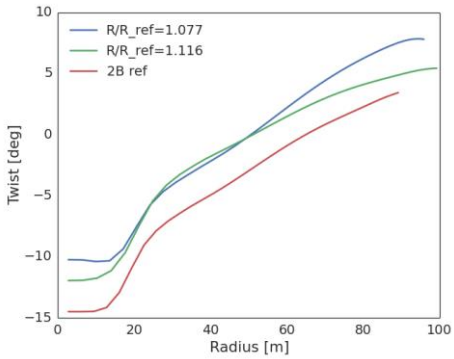

Figure 3.4-5 Twist distribution for the rR1.08 and rR1.12 designs compared to the 2B reference design.

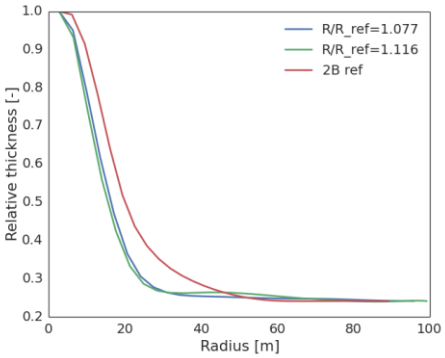

Figure 3.4-6 Relative thickness distribution for the rR1.08 and rR1.12 designs compared to the 2B reference design.

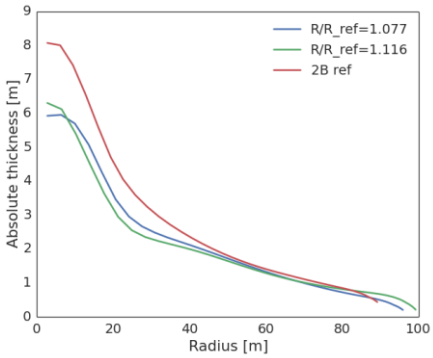

Figure 3.4-7 Absolute thickness distribution for the rR1.08 and rR1.12 designs compared to the 2B reference design.

A number of distributed quantities computed using HAWCStab2 under steady state conditions are shown in Figure 3.4-8 to Figure 3.4-13 for a range of wind speeds. The figures show a quite surprising characteristic, which is that the blade is progressively unloaded on the outer part with increasing wind speed, made possible by a quite extreme reduction of 80% of the torsional stiffness with almost eight degrees torsion at 10 m/s combined with the introduction of an aeroelastic coupling that ensures that the blade torsions towards feather when loaded. The optimized blade thus respects the flapwise root moment and tip deflection constraints while at the same time achieving a significant increase in AEP and simultaneous reduction in mass.

3.4.1 Blade Structural Design

Figure 3.4-14 shows the transparent lofted blade shape of the rR1.08 design viewed from the tip with the internal structure visible at selected sections. One noticeable feature is that the upper and lower spar caps are offset forward of the main axis of the blade and angled approximately 5 deg., most pronounced in the region r/R = 0.4 to r/R = 0.6. The combination of the more forward position of the caps and the introduction of an angle between their centre lines results in a significant modification of the structural pitch along

the blade from negative to 21 degrees at r/R=0.7 appears to be a very efficient means of introducing a coupling that increases the torsional response of the blade.

While these results show interesting directions for future very light-weight aeroelastically coupled blades, it should also be made clear that the optimized blades are not manufacturable, since material thicknesses in some parts of the blade have been reduced too much or even removed entirely in order to enable the large torsional responses. There are however, a number of degrees of freedom that could be introduced in the design process that could allow the optimizer to achieve these couplings without removing so much material. A first step could be to remove one of the two main shear webs connecting the spar caps, which would also reduce the blade mass by 7%. Additionally, the blade could be allowed to sweep moderately or off-axis fibre layups could be introduced in the spar caps.

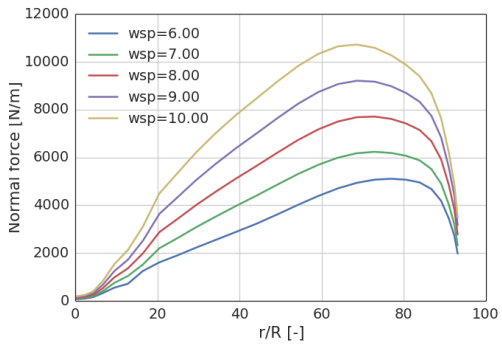

Figure 3.4-8 Distributed normal forces as function of blade fraction for the rR1.08 blade.

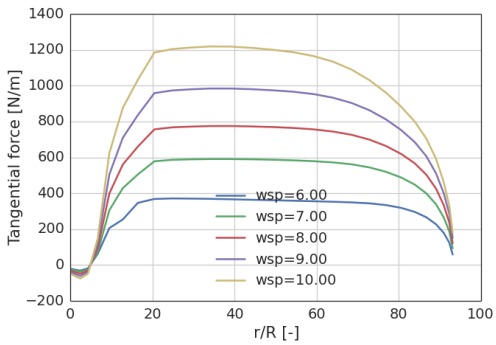

Figure 3.4-9 Distributed tangential force as function of blade fraction for the rR1.08 blade.

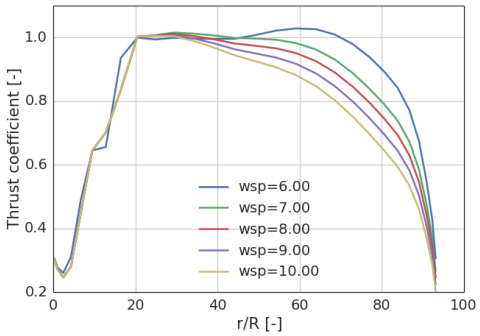

Figure 3.4-10 Local thrust coefficient as function of blade fraction for the rR1.08 blade.

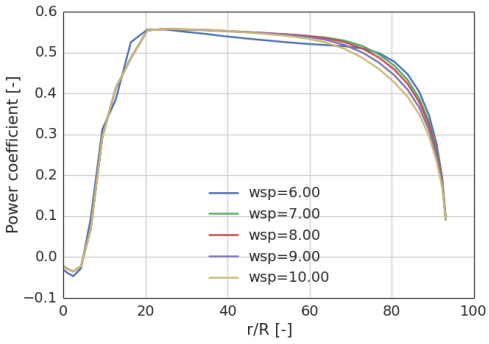

Figure 3.4-11 Local power coefficient as function of blade fraction for the rR1.08 blade.

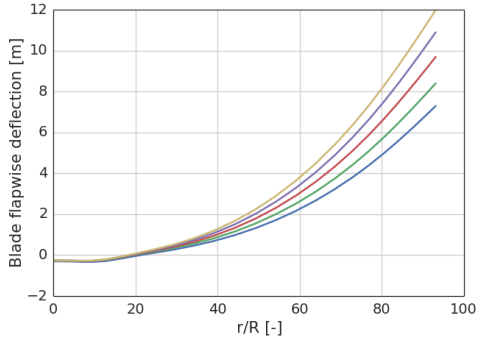

Figure 3.4-12 Blade deflection as function of blade fraction for the rR1.08 blade.

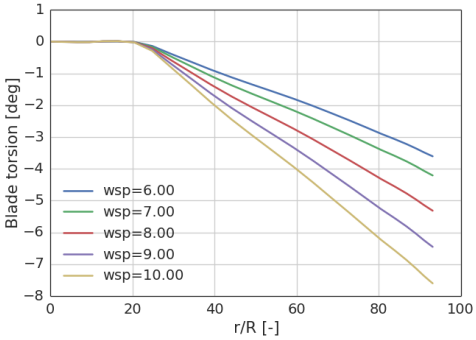

Figure 3.4-13 Blade torsion as function of blade fraction for the rR1.08 blade.

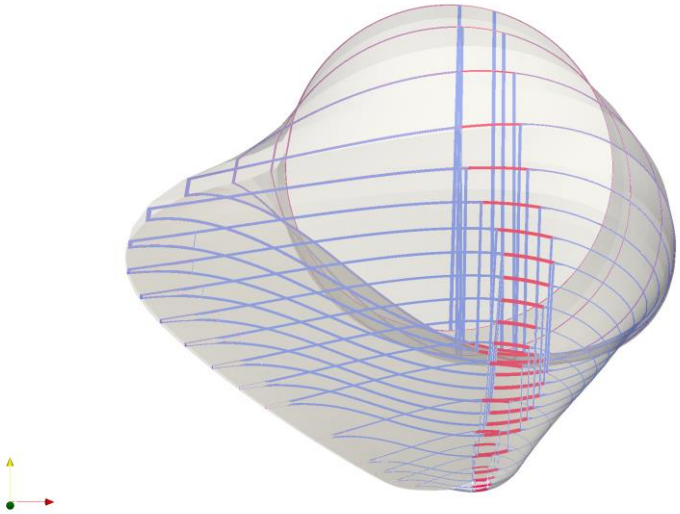

Figure 3.4-14 Lofted blade showing internal structure of the rR1.08 design.

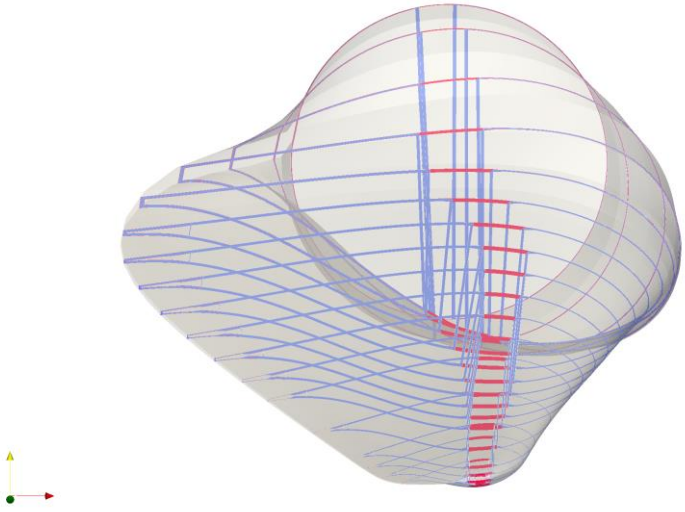

Figure 3.4-15 Lofted blade showing internal structure of the rR1.12 design.

3.4.2 Load Simulations

Load simulations were carried out on the rR1.08 and rR1.12 designs benchmarked against the two-bladed upwind reference rotor. Figure 3.4-16 shows the mean power production computed using HAWC2 for DLC 1.2 and 1.3, which shows that the two stretched rotors achieve 6.2% and 10.1% increases, respectively. As indicated from the steady-state HAWCStab2 simulations, the rR1.08 design achieves a reduction in flapwise

fatigue loads due to the significant torsional coupling described in the previous section, with a 13.8% reduction in the flapwise DEL and a 4% reduction in the edgewise DEL, as shown in Figure 3.4-17 and Figure 3.4-18. The rR1.12 design has significantly less torsional coupling and is heavier, resulting in 10% and 20% increases in flapwise and edgewise DELs, respectively. Looking at Figure 3.4-19 it is however evident that the blades strike the tower during shutdown DLC 5.1. While the blades would probably need more flapwise stiffness to avoid this, a better control strategy would likely also be able to mitigate this. The present downwind rotor configurations do are made with only 2.3 m pre-bend and 5 degrees tilt, but no coning, so the tower strike could also be mitigated with addition of coning, although this would likely reduce the AEP increase somewhat. For future work it is, however, clear that the assumption that the upwind deflection at shutdown is approximately equal to the steady state downwind deflection at rated wind speed, was not correct for these very flexible blades, so a better estimation of the upwind deflection is needed, perhaps requiring time-dependent aeroelastic simulations.

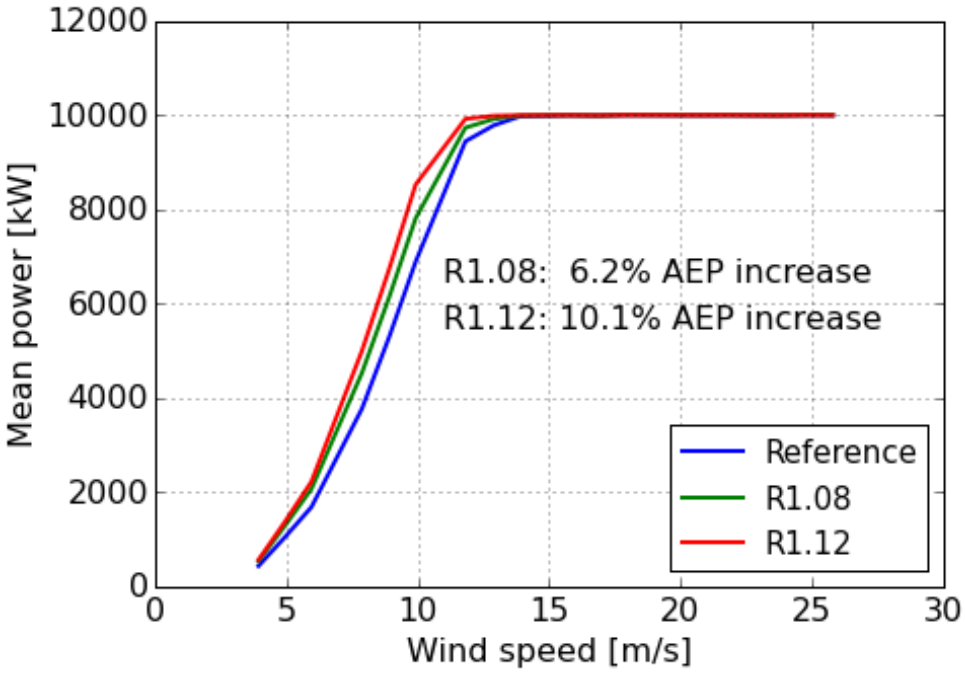

Figure 3.4-16 Mean generator power for the two new designs compared to the two-bladed upwind reference

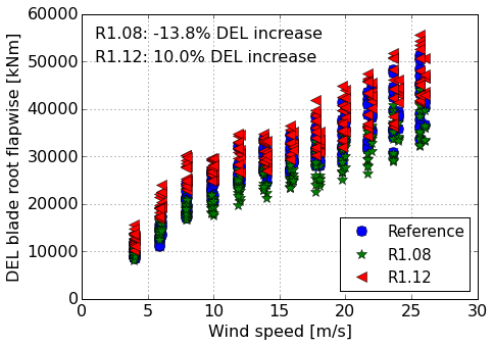

Figure 3.4-17 Flapwise damage equivalent load computed using HAWC2 based on DLC 1.2, 1.3 and 5.1.

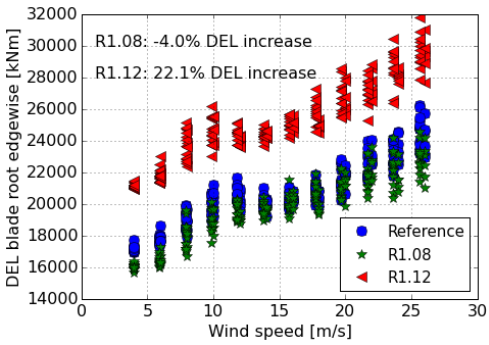

Figure 3.4-18 Edgewise damage equivalent load computed using HAWC2 based on DLC 1.2, 1.3 and 5.1.

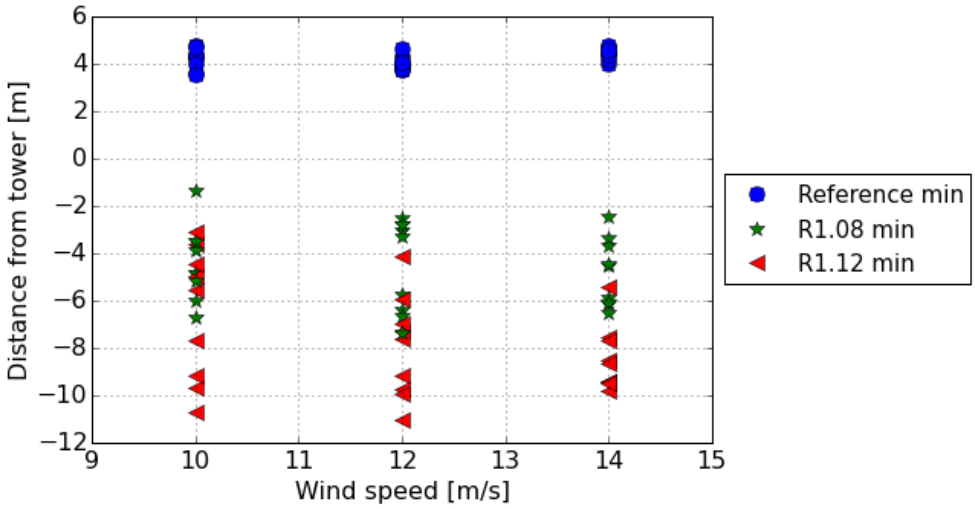

Figure 3.4-19 Tower clearance for DLC 5.1.

3.5 Conclusions

The present conceptual design study of a two-bladed downwind rotor fitted on the DTU 10MW RWT platform showed that it is possible to stretch the rotor considerably to gain an increase in AEP without increasing loads if the blades are designed with aeroelastic couplings which passively alleviate loads. The overall most promising design achieved an AEP increase of 6.2%, with power increases of up almost 20% at below rated wind speeds. While the large unloading of the tip close to rated reduced the efficiency of the rotor, the inner part of the rotor was made significantly more efficient due to the ability to use airfoil sections with lower relative thickness due to the relaxed tip deflection constraints. The study demonstrated that even with an extreme torsional response of up to 8 degrees at the tip at rated wind speed, the rotor was aeroelastically stable under normal operating conditions as well as extreme turbulence conditions, and that the damage equivalent loads in the blade root could be reduced with up to 13% despite the almost 8% increase in radius.

There are several challenges still to be solved, since the present designs were far from manufacturable due to excessive removal of material to achieve the torsional coupling. Other mechanisms need to be put in play to achieve the strong torsional coupling while maintaining a realistic material thickness distribution such as removal of one of the two shear webs connecting the spar caps, sweep and off-axis fibre layups. Also, the present designs experienced tower strikes during shutdown, which also needs to be addressed in future work probably requiring larger flapwise stiffness but more significantly a better control strategy at shutdown than implemented in the present DTU controller.

CHAPTER 4 SMART ROTOR

4.1 Introduction to the Innovative Concept

One of the innovative concepts explored in WP2 of the INNWIND project is the use of active flaps for load control [14], [15]. In the past decade at DTU the design of such a system has been explored and it is oriented towards flexible elastomer trailing edge geometry, activated by pressure fluid, referred to as Controllable Rubber Trailing Edge Flap (CRTEF) [16].

In order to deliver an aeroelastic design of a smart blade for WP1, the aeroelastic optimization of a 10MW wind turbine smart blade equipped with active trailing edge flaps is carried out. The multi-disciplinary wind turbine analysis and optimization tool HawtOpt2 is utilized, in which a simultaneous aerodynamic and structural optimization of a 10 MW wind turbine rotor is carried out with respect to material layups and outer shape. Active trailing edge flaps are integrated in the design taking into account their geometrical and structural implications. The concept of integrating active flaps in a blade design is illustrated Figure 4.1-1, where the blade is designed without a trailing edge (e.g. 10% c) over the whole span going from flatback airfoils on the inner part to an outboard part where active and passive morphing trailing edges (flaps) should be mounted. A trailing edge web is inserted to compensate for the missing trailing edge, and to be used as attachment point for the flap modules (as e.g. implemented in the INDUFLAP project flap prototypes, Figure 4.1-2). The DTU 10MW Reference Wind Turbine blade design [17] is considered as the baseline case.

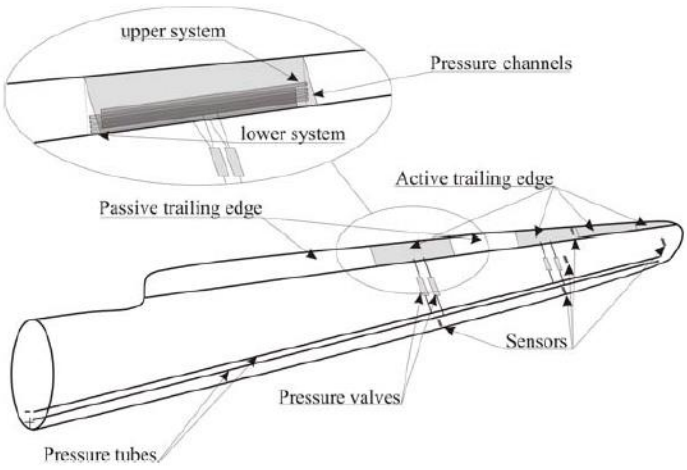

Figure 4.1-1 Concept of integrated active flaps in a blade design.

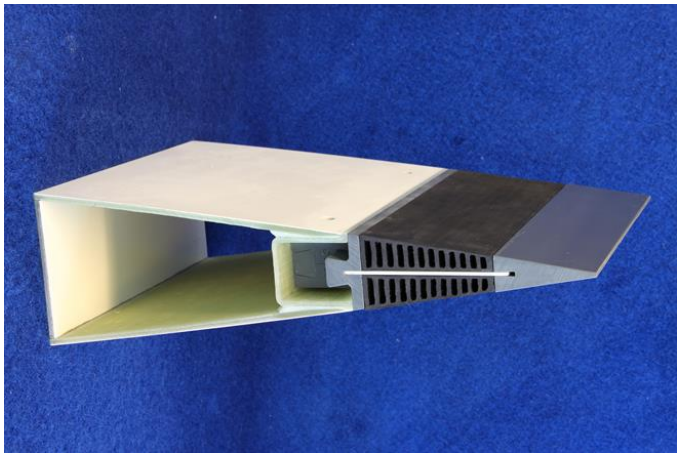

Figure 4.1-2 Integration of the flap system in a blade section structure in the Induflap project [16].

4.2 Modelling environment and configuration

The HawtOpt2 framework is used in this work in a similar fashion as described in [18]. The HawtOpt2 framework uses OpenMDAO (Open-source Multidisciplinary Design, Analysis, and Optimization Framework) [19] to handle the definition of the optimization problem, workflow, dataflow and parallelization of simulation cases. In this work, the gradient-based sequential quadratic programming optimizer SNOPT [20], [21] is used. The development of the HawtOpt2 framework is part of a larger effort named Framework for Unified Systems Engineering and Design of Wind Turbine Plants (FUSEDWind) [22].

Interfaces have been developed to connect the optimization framework to the finite element cross sectional tool BECAS and to the aeroelastic tool HAWCStab2, that form the core of the state-of-the art analysis capability provided by the tool. BECAS [23], [24], [25] allows for the evaluation of the cross sectional structural and mass properties of the blade. The tool is based on a 2D finite element formulation that allows for an exact geometrical description of the section. Different regions with different material and different thicknesses can be specified enabling the description of different layups. The linear high-order aero-servo-elastic model implemented in HAWCStab2 [26], [27] uses an unsteady blade element momentum (BEM) model of the rotor and a geometrically nonlinear finite beam element model to compute steady-state aerodynamic states, structural deflections, and linearized models of the wind turbine.

A method to evaluate fatigue damage based on a linear model is also integrated in the framework but not utilized in this presented work. The method is frequency-domain based and it does therefore not require time-domain simulations. The method is described in detail by Tibaldi et al [28], [29] . Furthermore, the aerodynamic effect of the trailing edge flaps in the linear aeroelastic model is integrated based on [30], utilizing a quasi-steady aerodynamic trailing edge flap model. With this capability, the effect of a flap controller on the fatigue loads can be accounted for.

The blade design is parametrized in terms of outer shape and material layups. The blade planform is described in terms of distributions of chord, twist, relative thickness, and pitch axis aft leading edge. The internal structure is defined by a number of regions which covers a fraction of the cross-sections along the blade Figure 4.2-1). Each region consists

of a number of materials that are placed according to a certain stacking sequence. The planform and internal structure parameters are used as design variables in the optimization problem. In the case of the flap geometry implementation, the connection web to the flap region (web C in Figure 4.2-1) is fixed at 10% of the chord from the trailing edge. The reference blade is made from glass fibre reinforced composites and balsa wood, which is used as sandwich core material. The composite layup of the reference blade is defined in terms of a stacking-sequence of layers representing multidirectional plies. Balsa, uniaxial and triaxial layers are utilized. In the case of the flap geometry, elastomer material layers are utilized for the trailing edge regions, corresponding to (simplified) representative realization of a flexible flap [17].

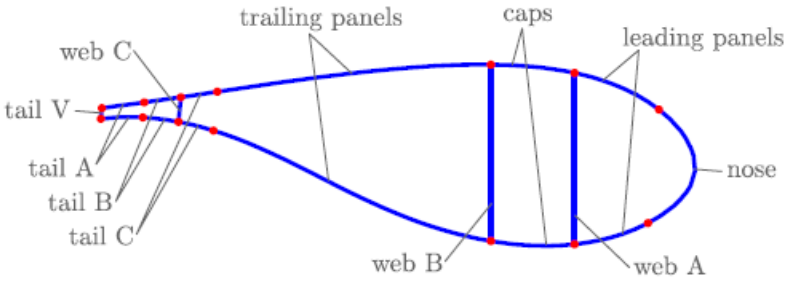

Figure 4.2-1 Blade section layup parametrization [16].

The numerical optimization problem which is solved consists of a cost function to be minimized, subject to several nonlinear constraints. The cost function is a weighted sum of Annual Energy Production (AEP) and blade weight. Both parameters are normalized with their initial reference values. The constraints depend on limits for planform and structural variables, and resulting structural strains. The general process of the optimization framework is shown in Figure 4.2-2. In this work, the precomputed extreme loads and the calculated fatigue loads are not taken into account in the optimization process.

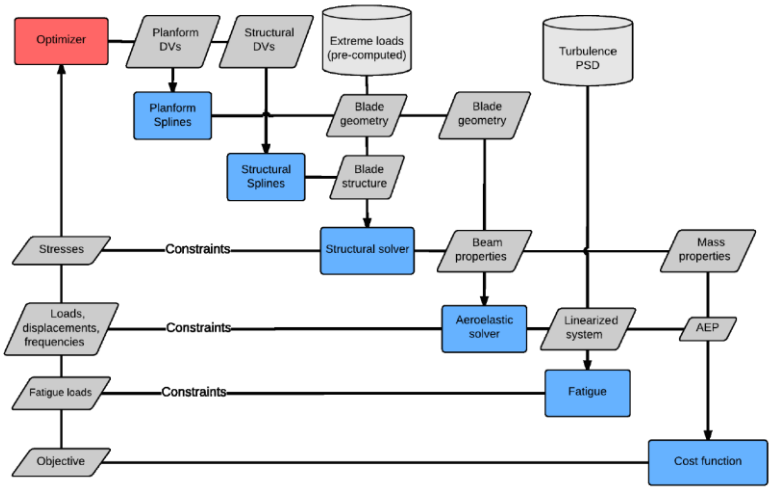

Figure 4.2-2 Extended design structure matrix diagram of the work in HawtOpt2.

During the optimization process, the rotor design is evaluated using HAWCStab2 in the range of operational wind speeds at normal power production, with the corresponding wind input parameters according to the design wind input for the turbine class [31]. AEP and steady state loads are calculated in this process. Furthermore three additional load cases are simulated to account for extreme design loads evaluation, which comprise standstill operation at 50-year extreme wind speed with different pitch settings. The loads estimated with HAWCStab2 are then used to estimate strains on the structure with BECAS. These strains are part of the design constraints to guarantee the solidity of the structure.

The simulated flap configuration is chosen based on prior studies [15], and the agreed common configuration in the WP2 of the INNWIND.EU project. The main flap parameters are shown in Table 4.1. The flap extent on the baseline blade planform is shown in Figure 4.2-3. The flap extends on 30% of the blade span with a constant 10% chordwise length.

Table 4.1 - Main flap parameters.

Flap configuration	
Chordwise extension	10%
Deflection angle limits	±10º
Spanwise length	25.9m (30% blade length)
Spanwise location	59.59m-85.50m (from blade root)
Airfoil	FFA-W3-241

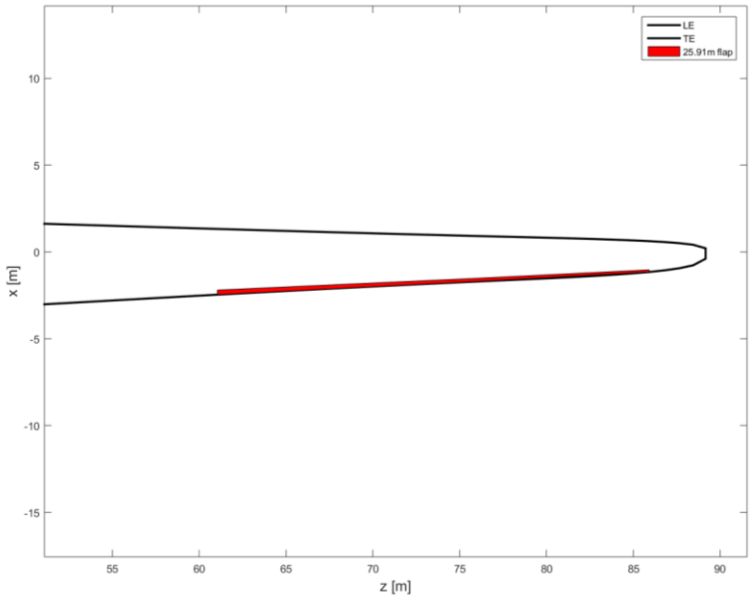

Figure 4.2-3 Flap geometry implemented on the planform of the baseline DTU 10MW RWT blade.

In order to evaluate the target smart blade design, the design cases compared in this work are the ones shown in Table 4.2.

Table 4.2 – Compared design cases

DTU 10MW Reference Wind Turbine (RWT)	
Case 1	Baseline DTU 10MW RWT
Case 2	Optimized baseline
Case 3	Optimized design with flap geometry

The baseline design (Case 1) is referring to the standard design of the DTU 10MW RWT. Case 2 is an optimized version of the DTU 10MW RWT. Case 3 is an optimized version of the DTU 10MW RWT with flap geometry. For the optimization cases, the objective is a compound objective consisting of the weighted sum of mass and AEP where the weight is chosen as 0.875 and 0.900 for Case 3 and Case 2, respectively (low mass biased design). Both the internal structural layout and the blade shape are included in the design variables, allowing the chord, twist, relative thickness and layup thicknesses and web positions to vary utilizing the mentioned design variables. The flap geometry is implemented in the internal layup definition, resulting in a predefined trailing edge web at the 10%c location and an elastomer material definition at the trailing edge; whereas there is no effect of the flaps appearing on the calculated loads.

4.3 Results

This section shows results of not converged optimizations. The designs, even if they have not reached convergence, are considered representative because the constraints are all within acceptable limits.

For both cases, the optimizer pursues the compound objective towards low mass biased design by varying the design variables and satisfying the specified constraints. In Figure 4.3-1 the resulting blade mass and corresponding AEP is shown for the major iteration steps up to iteration 8 and 11. The blade designs achieved (down-right in Figure 4.3-1) have 8% and 13% reduced mass compared to the baseline and while being practically AEP neutral (up to 0.3% increase).

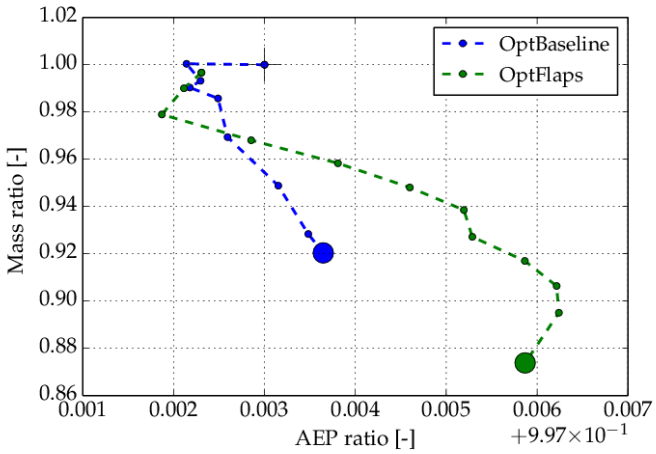

Figure 4.3-1 Resulting mass and AEP ratios (over the baseline case) for the optimization steps. Comparison between optimized baseline and optimized case with the flap geometry.

The resulting design planforms and main structural properties are here compared to the original design. In terms of planform, the optimized designs result in a slightly more slender blade, where the chord is reduced largely at the root and slightly from 40m outboard (Figure 4.3-2). The twist distribution (Figure 4.3-3) is increased (nose up, towards stall) in order to meet the AEP objective.

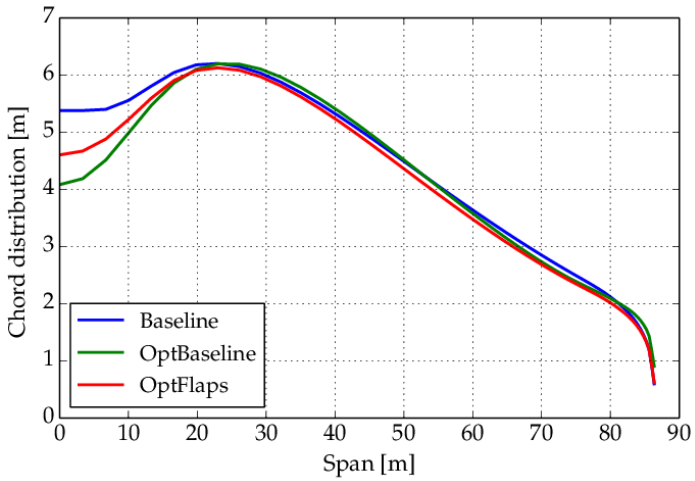

Figure 4.3-2 Chord distribution comparison between baseline, optimized baseline and optimized case with the flap geometry.

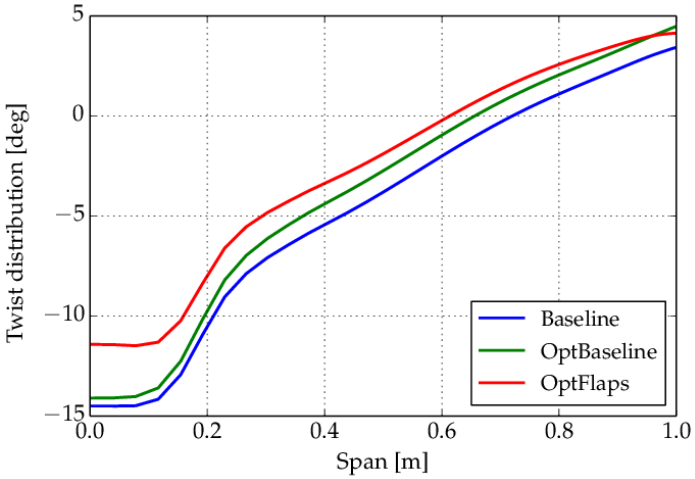

Figure 4.3-3 Twist distribution comparison between baseline, optimized baseline and optimized case with the flap geometry.

In terms of structural properties, the mass distribution resulting in the overall blade mass reduction is compared to the baseline in Figure 4.3-4. Most of the mass reduction originates in the root region. The flap design has lower mass also at the flap region. The major mass reduction cannot therefore be attributed to the modified trailing edge due to the flap implementation. In Figure 4.3-5 and Figure 4.3-6 the flapwise and edgewise stiffness distributions are compared. Both optimized distributions are reduced in the very inner root region, and the edgewise stiffness is also reduced as expected in the flap region

due to the changes to the trailing edge. Furthermore, the torsional moment of inertia of the optimized designs is shown in Figure 4.3-7, where there is no considerable change between the baseline and both optimized designs. The position of the edgewise center of gravity offset from the pitch axis (Figure 4.3-8) in the design with the flap geometry is not considerably affected, except at the very inner root region.

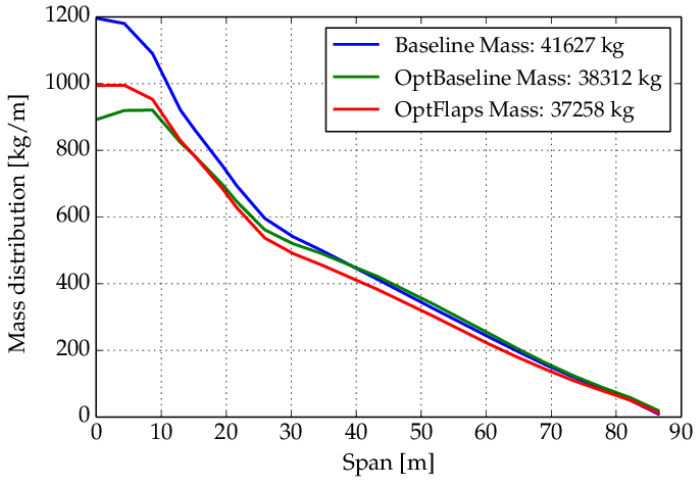

Figure 4.3-4 Mass distribution comparison between baseline, optimized baseline and optimized case with the flap geometry.

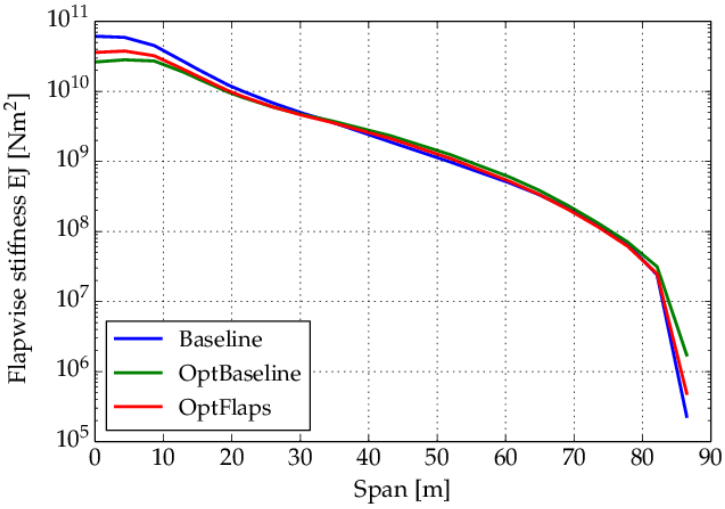

Figure 4.3-5 Flapwise stiffness distribution comparison between baseline, optimized baseline and optimized case with the flap geometry.

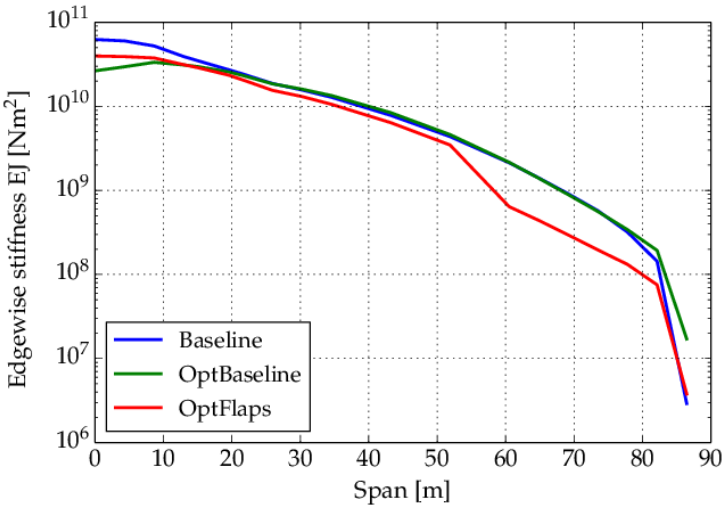

Figure 4.3-6 Edgewise stiffness distribution comparison between baseline, optimized baseline and optimized case with the flap geometry.

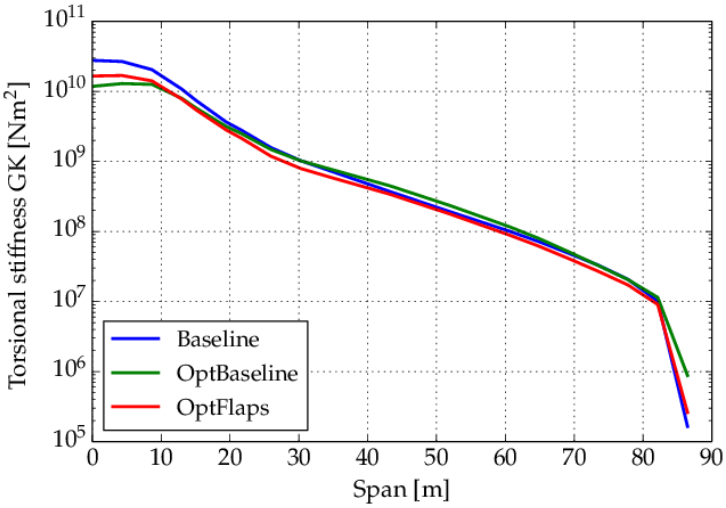

Figure 4.3-7 Torsional stiffness distribution comparison between baseline, optimized baseline and optimized case with the flap geometry.

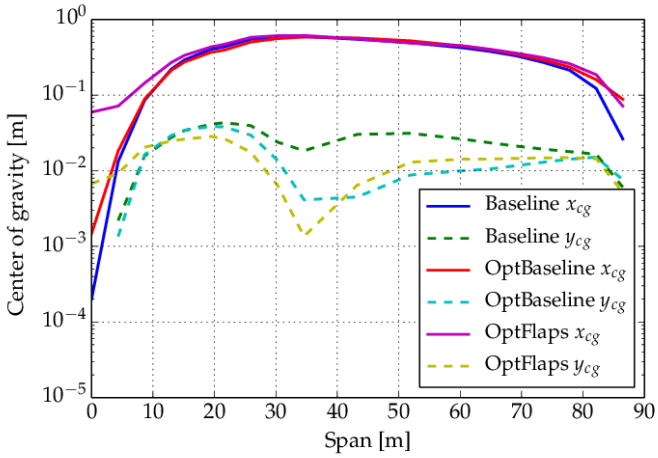

Figure 4.3-8 Center of gravity position distribution comparison between baseline, optimized baseline and optimized case with the flap geometry.

Details of the material layup thicknesses at the trailing edge regions are shown in Figure 4.3-9 and Figure 4.3-10. Regions 0 and 1 correspond to the Tail A and B regions shown in Figure 4.3-11, which are the first trailing edge regions on the suction side. It is seen that at the 69%-99% blade span region the glass fibre layers are replaced by the 'rubber' material corresponding to the representative elastomer material properties. The flap structural geometry parameters are not optimized in this framework, but rather the rest of the structure adapts to the flap presence.

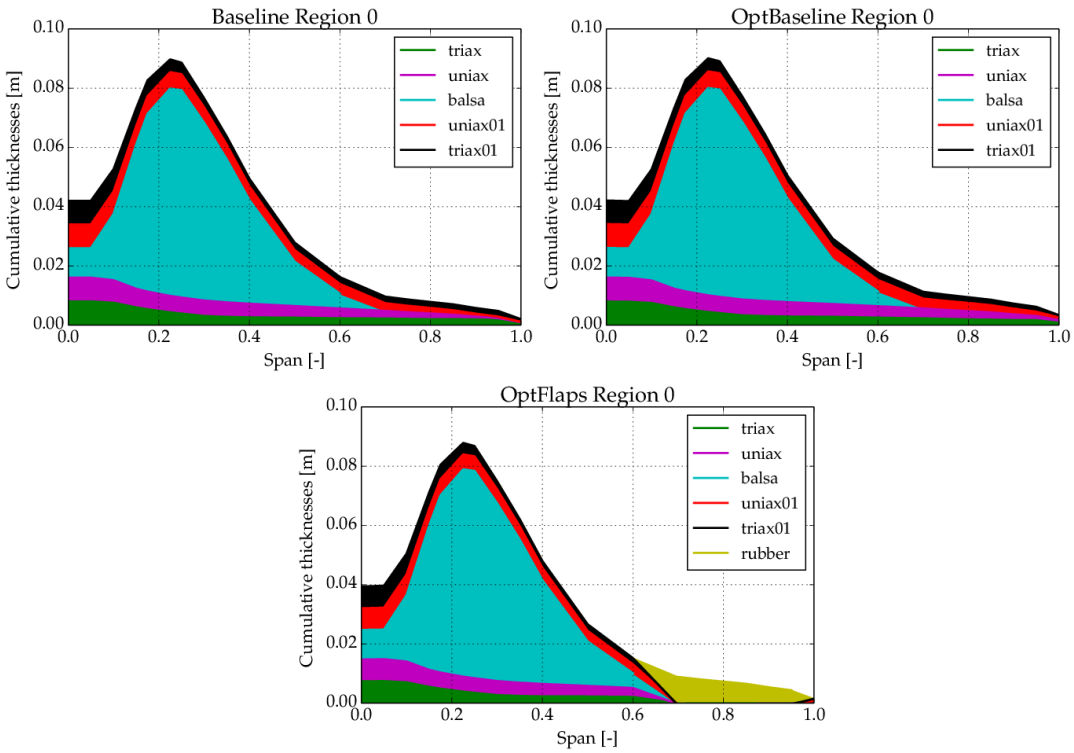

Figure 4.3-9 Thickness distribution for the material layups between baseline, optimized baseline and optimized case with the flap geometry. Region 0 is the first trailing edge panel on the pressure side (Tail A in Figure 4.2-1).

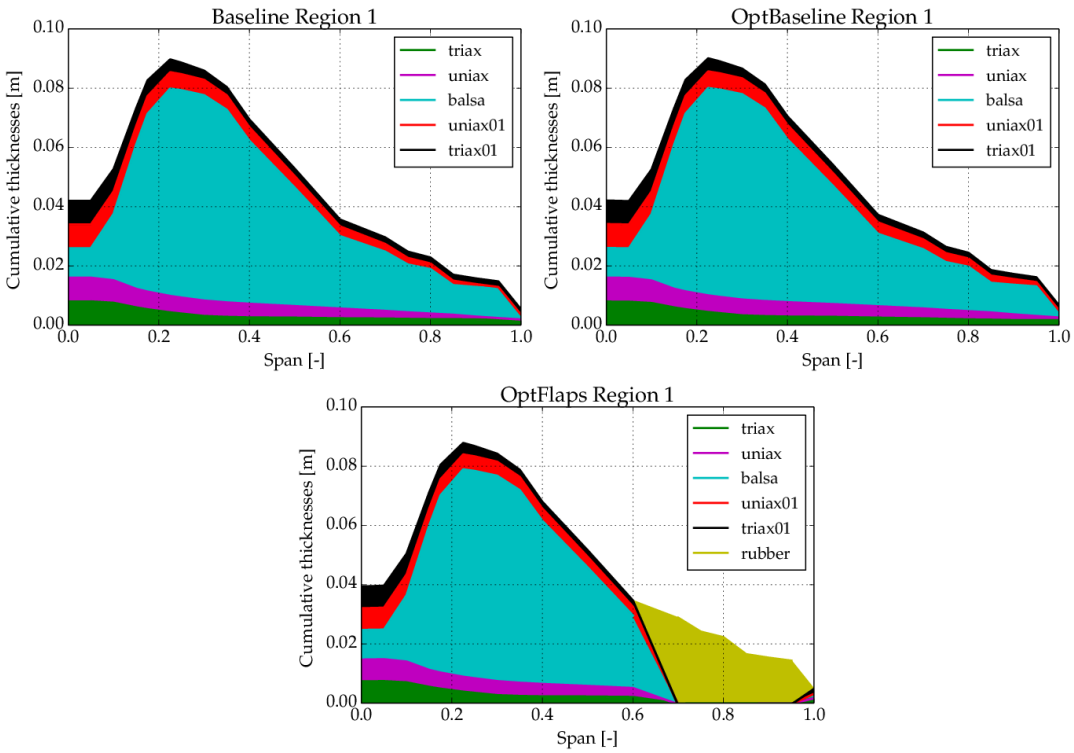

Figure 4.3-10 Thickness distribution for the material layups between baseline, optimized baseline and optimized case with the flap geometry. Region 1 is the second trailing edge panel on the pressure side (Tail B in Figure 4.2-1).

The internal structure geometry is shown for the section at 85% span of the blade (mid-flap region) in Figure 4.3-11, Figure 4.3-12 and Figure 4.3-13 for the baseline design, the optimized design and the optimized design with the flap geometry respectively. The truncated trailing edge with the additional web where the flap geometry is connected is shown, where different colors represent different material layups. Furthermore the optimized designs show the resulting changes in the spar geometry but also the reduced chord at this region.

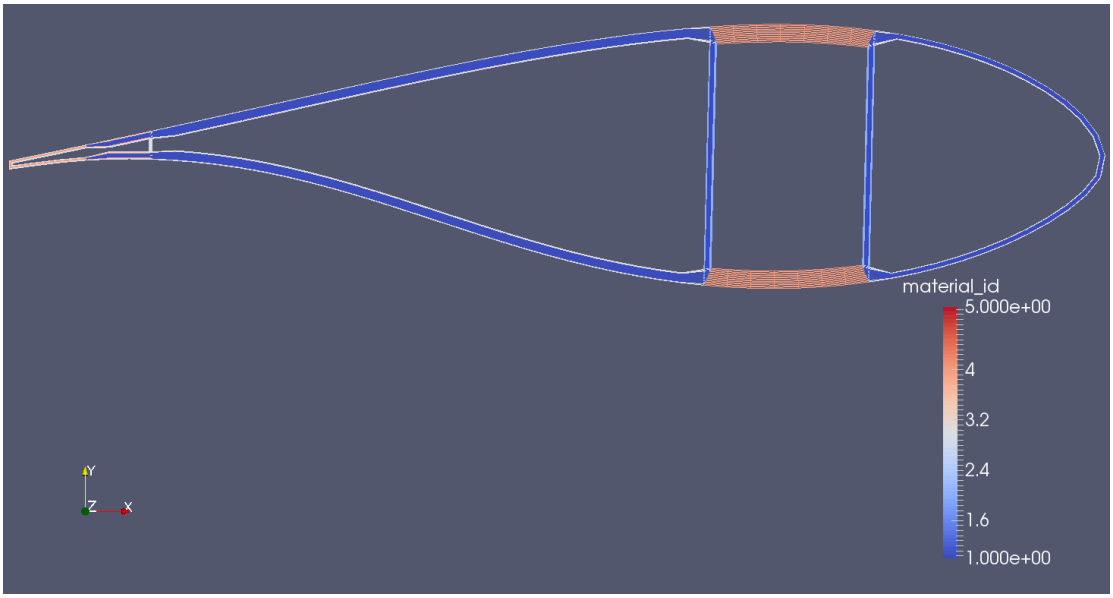

Figure 4.3-11 Internal structure of the baseline design - 85% blade span section.

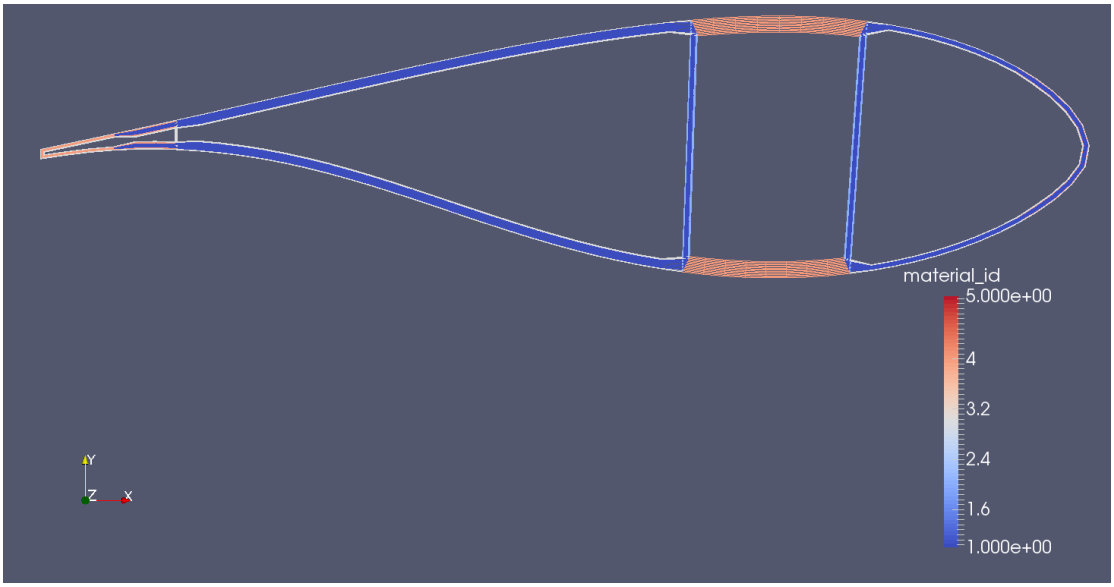

Figure 4.3-12 Internal structure of the optimized baseline design - 85% blade span section.

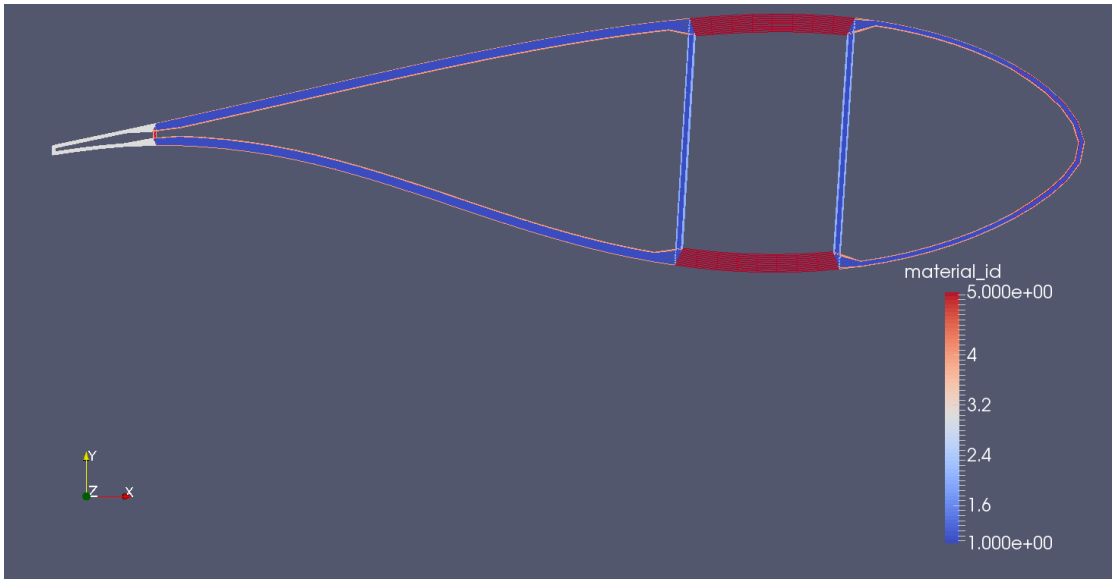

Figure 4.3-13 Internal structure of the optimized design with the flap geometry - 85% blade span section.

In Table 4.3 the blade main structural modes frequencies are shown. The most considerable change is seen for the edgewise mode in both the optimized and the optimized with flap geometry cases. Frequency placement has not been explored in this optimization investigation.

Table 4.3 - Comparison of structural frequencies between cases.

model	baseline	optimized	optimized + flap
1st flap [Hz]	0.610067E+00	0.566878E+00	0.608678E+00
1st edge [Hz]	0.959575E+00	0.849826E+00	0.858058E+00
2nd flap [Hz]	0.175761E+01	0.166357E+01	0.174561E+01
2nd edge [Hz]	0.288871E+01	0.265472E+01	0.220519E+01
3rd flap [Hz]	0.359624E+01	0.340786E+01	0.355314E+01
3rd edge [Hz]	0.580472E+01	0.548027E+01	0.462817E+01
4th flap [Hz]	0.618287E+01	0.589229E+01	0.598585E+01
1st torsion [Hz]	0.667065E+01	0.665577E+01	0.675661E+01

Figure 4.3-14 shows a comparison of the first seven wind turbine aeroelastic modes frequencies and damping between the three designs. A significant reduction in the frequencies of the modes associated with the blades is achieved. The optimized baseline has lower flapwise and edgewise frequencies. The frequencies of the first forward whirling edgewise mode of the two optimized blades approach the 6P external excitation at high wind speeds but they do not overlap. A further investigation should address any potential issue related to these changes. No significant differences are observed on the damping of the aeroelastic modes between the three models.

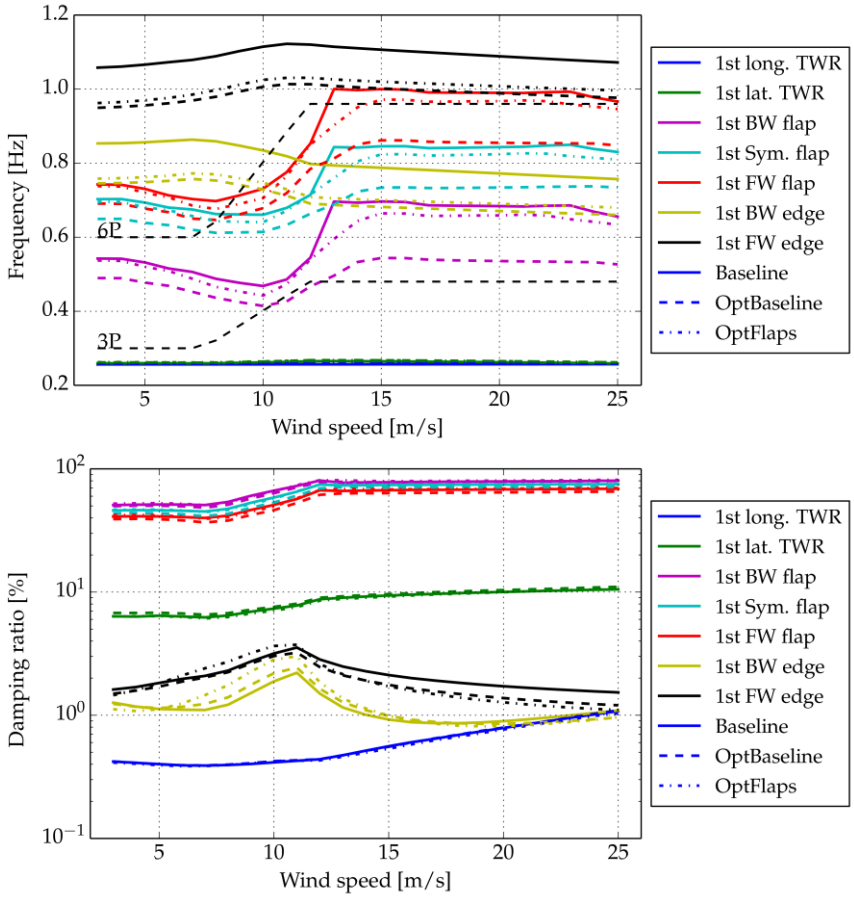

Figure 4.3-14 First seven wind turbine aeroelastic frequencies and damping ratios. Comparison between baseline, optimized baseline and optimized design with the flap geometry.

4.4 Conclusions

The aeroelastic optimization of the DTU 10MW RWT blade equipped with active trailing edge flaps is carried out. The multi-disciplinary wind turbine analysis and optimization tool HawtOpt2 is utilized, in which a simultaneous aerodynamic and structural optimization of the rotor is carried out with respect to material layups and outer shape. Trailing edge flaps are integrated in the design taking into account their geometrical and structural implications with no effect on loads. The optimization results show that such a blade design is feasible within the objectives for low mass biased design with same AEP performance and the specified geometrical and load constraints. A blade design with 13% reduced mass compared to the original DTU 10 MW RWT blade is presented, where the geometry of a 30% blade length flap of 10% chord length is integrated in the trailing edge. This design is also compared to an optimized version of the baseline blade without flap geometry integration and shows a benefit in terms of mass reduction. The main purpose of this investigation is to show the feasibility of such a design which includes the flap together with an optimized blade geometry.

For the next steps, the achieved fatigue load reduction using the active trailing edge flaps should be taken into account. This development has already been implemented as part of

this work and still needs to be evaluated. A simple individual flap controller (IFC) close to industry standards is chosen, where the flap control algorithm is implemented similarily to the individual pitch control as described in [30], including gain scheduling and actuator dynamics. The flap controller is implemented in state-space form and connected in feedback with the resulting full system matrices from HAWCStab2, thus allowing for fatigue load evaluation as described in [29].

CHAPTER 5 INNOVATIVE INNER BLADE STRUCTURE

5.1 State of the art and motivation

State of the art rotor blade design indicates the use of a spar-box as the main load bearing component accompanied by a number of shear-webs depending on the size of the rotor blade. The skins and shear-webs consist of a sandwich structure while the spar caps are dominated by unidirectional fibers in the pitch-axis direction to deliver the desired axial stiffness. Since producing long (>60m) rotor blades using carbon fiber composite materials is still too expensive for commercial wind turbines, glass fiber reinforced composites (GFRP) are preferred from the manufacturers.

The need for longer blades for the new many multi-megawatt machines of the future, even for the existing (>7 MW) designs, where blade weight is a restrictive parameter calls for the need to introduce an economic solution for the use of carbon fiber composite materials in the manufacture of rotor blades. New designs that take advantage of carbon fiber composite structures made of less expensive manufacturing techniques, such as filament winding and pultrusion, have to be established. In that context, the idea to replace the original spar-box beam of the rotor blade by an internal space truss structure was investigated.

5.2 Brief description of the concept

The INNWIND.EU reference blade design [17] recommends two spar caps that consist of unidirectional Gl/Ep composite material, 3 shear-webs of a sandwich structure made of biaxial Gl/Ep fabric and balsa wood and skins, sandwich structures as well, consisting of triaxial and uniaxial Gl/Ep composite materials; balsa wood as core material.

In order to reduce the weight of the reference blade the conceptual design proposed by University of Patras CORE team (UPAT) suggests the replacement of the spar-box and 3rd web with an internal space truss. This will make possible to remove the uniaxial composite material from the rotor blade's skin and reduce the thickness of the triaxial composite material. The internal truss should be able to achieve the axial stiffness and strength of the reference blade.

The truss topology initially consisted of a large number of rods/beams and the modelling of the internal truss was achieved using Beam188 elements while the skin was modelled with Shell181 elements (Figure 5.2-1) of the ANSYS commercial code.

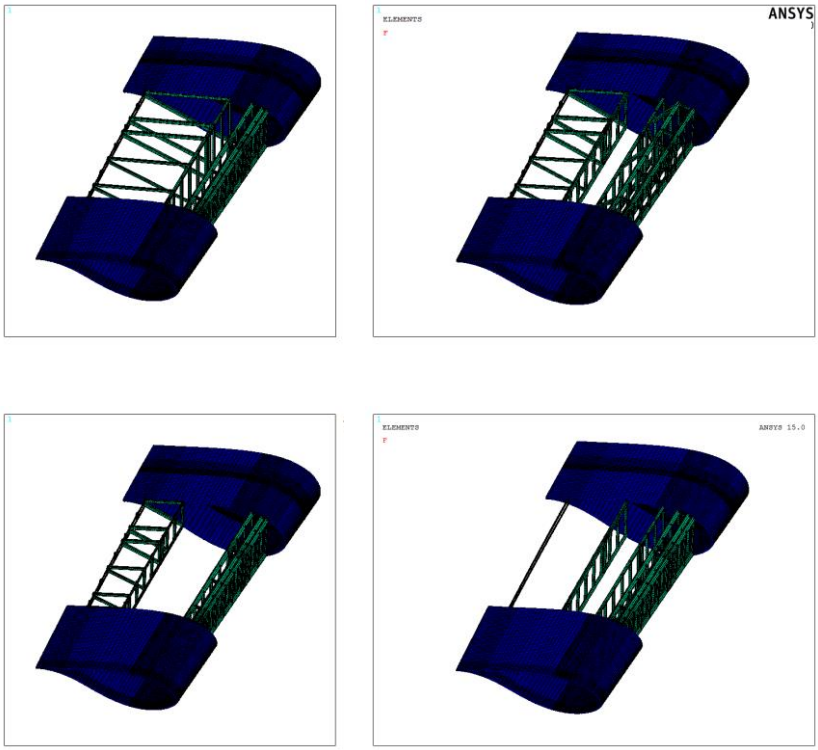

Figure 5.2-1 Examples of tested topologies of the internal truss

The investigation focused into modelling an internal space truss made of Gl/Ep composite materials which would have a stiffness, strength and elastic behaviour close to those of the reference blade while keeping the weight of the blade lower. The main challenge encountered was the local failures of the blade, a numerical artefact due to concentrated forces applied in a small number of nodes (Figure 5.2-2).

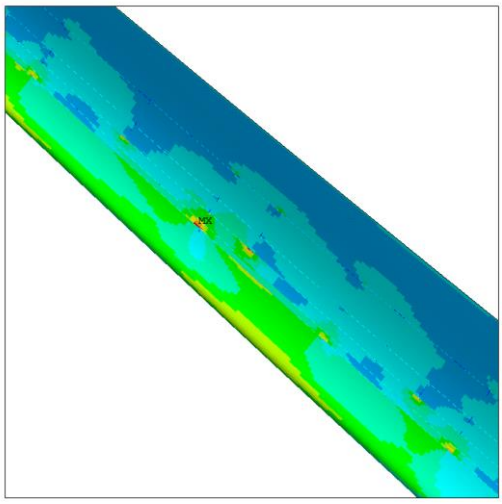

Figure 5.2-2 Local failure due to numerical artifacts

To overcome the situation, the blade was modelled from scratch using only shell element formulation even for each individual beam component of the space truss structure (Figure 5.2-3).

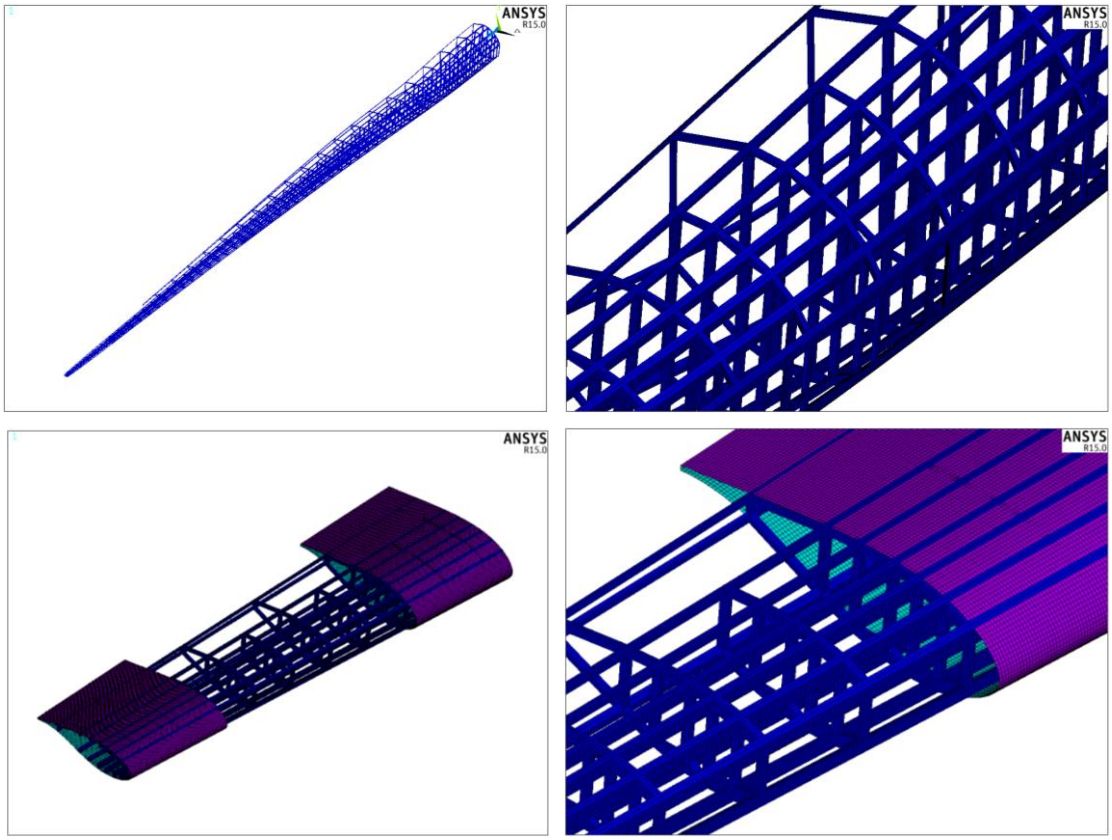

Figure 5.2-3 Blade model using only shell elements

The new FE model of the blade consists of 600,000+ elements and more than 3,000,000 degrees of freedom. Any change in the truss topology or layup configuration in the course of this investigation needs more than 24 hours to complete and up to 36 hours for one strength or buckling analysis run-time in fast PC servers. As a result, due to time limitations, in the final design for this report the internal truss is modelled with Beam188 elements.

5.3 Anticipated PROS and CONS

The main advantage of the conceptual design proposed by UPAT CORE Team is that it offers to the manufacturer the ability to use composite materials produced by mass production techniques, e.g. filament winding and pultrusion instead of prepregs and fabrics, thus less expensive. Moreover, the control during the production of such structures is higher than in manual prepreg or fabric laying type composite materials, leading to better quality structures.

Furthermore, the modular construction of the space truss facilitates the implementation of modular blade concepts with known advantages in the transportation as well as the repair and the maintenance of the rotor blade.

The main disadvantage of the concept is the complexity in joining the various elements. More specifically, in the locations where more than 2 beams meet the joint calculation and construction is a challenging task.

5.4 Assessment of the structural integrity of the proposed design

5.4.1 Design layout and dimensioning

Since the idea behind the implementation of a space truss instead of the traditional spar-box beam of the reference blade was to introduce an economic and efficient solution for the use of carbon fiber composite materials in rotor blades, two (2) final blade designs are presented. The first one is solely a GFRP construction along with balsa wood as core material where needed, while in the second one some of the beams of the space truss are made of C/Ep material.

The internal truss topology is kept the same for the 2 models and is presented in Figure 5.4-1. Eventually, information on beam dimensioning and their exact position into the blade might be made available upon request; due to space limitations such details are not presented it in this report.

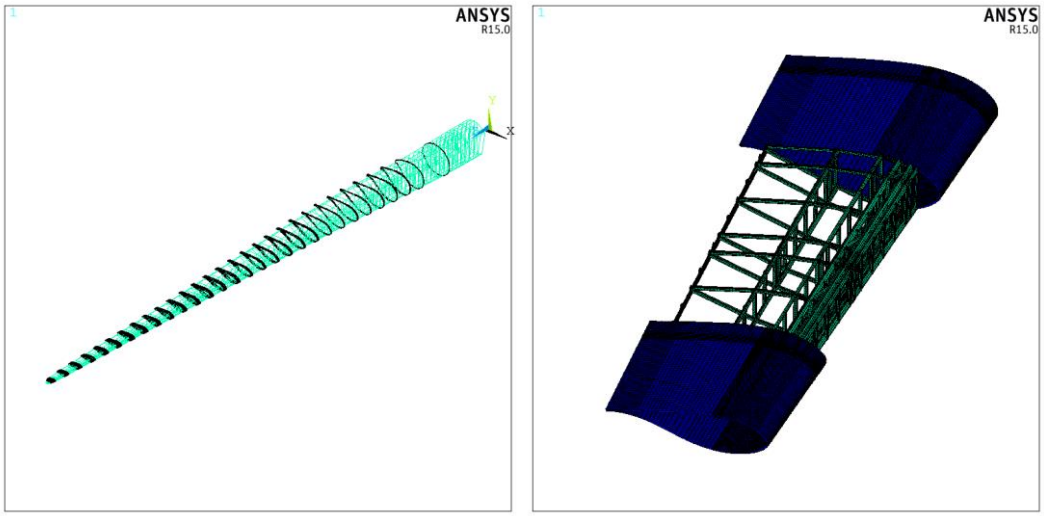

Figure 5.4-1 Truss Topology

In both cases the skin of the blade consists only of triaxial fabric and balsa wood in a sandwich form of [triax/balsa/triax], as per the reference wind turbine blade.

The FE model in ANSYS is based on a Reissner – Mindlin shell formulation. The skin consists of 4-node multilayer shell181 elements while the truss consists of 2-node beam188 elements. The triaxial, uniaxial fabric and balsa wood properties were all based on the benchmark input provided by the coordinators while the CFRP mechanical properties are presented in Table 5.1.

Table 5.1 - Typical mechanical properties of T700S C/Ep composite

Property	Value
E_1	148.51 [GPa]
E_2	9.03 [GPa]
G_{12}	5.55 [GPa]
v_{12}	0.225 [GPa]
Xt	768.84 [MPa]
Xc	537.98 [MPa]
Yt	5.49 [MPa]
Yc	31.43 [MPa]
S	28.46 [MPa]
Density	1600 kg/m^3

It is noted here that in the failure stress values presented in Table 5.1, the characteristic values are divided by a material safety factor of 2.205 according to GL design guidelines. For the elastic stability analysis a safety factor of 2.042 was applied in the elastic constants as described in the input provided by the coordinators for the structural benchmark.

The total mass of each of the materials used in the 2 blade models is presented in Table 5.2 while coordinates of the mass-centre of the blade are presented in Table 5.3.

Table 5.2 - Overall mass for each material

Material	Reference Blade	Gl/Ep Blade	C/Ep Blade
Triaxial	11319.0 [kg]	8472.6 [kg]	8472.6 [kg]
Biaxial	4076.6 [kg]	-	-
Balsa	5074.8 [kg]	5411.0 [kg]	5411.0 [kg]
Uniaxial (Glass)	21908.9 [kg]	26049.0 [kg]	5367.0 [kg]
Uniaxial (Carbon)	-	-	11591.0 [kg]
Total	**42379.3 [kg]**	**39932.6 [kg]**	**30841.6 [kg]**

Table 5.3 - Coordinates of mass centre

	Reference Blade	Gl/Ep Blade	C/Ep Blade
X coordinate [m]	-0.158	0.300	0.124
Y coordinate [m]	0.035	0.009	0.031
Z coordinate [m]	28.800	35.046	33.600

It is noted that the first section of the FE model is at 2.8 m.

5.4.2 Structural integrity verification

The constraints set for verifying the structural integrity of the new structural blade design were the same as those for the reference wind turbine. Analysis was performed against stiffness, strength under extreme loads as well as elastic stability. The loading imposed on the blade to verify its performance was that used in the benchmark exercise performed within INNWIND.EU project. The target for the design was that the new blade should perform the same or better than the reference wind turbine blade.

The comparison between the 2 models that are presented and the reference blade in terms of load carrying capacity, elastic stability and tip deflection are presented in Table 5.4 while some selective results are presented in Figure 5.4-2 to Figure 5.4-5.

Table 5.4 - Mechanical performance of various blade models

	Reference Blade	Gl/Ep Blade	C/Ep Blade
Tip Deflection [m]	20.6	24.18	11.52
Buckling critical Load factor	0.97	0.739	0.946
Strength multiplication factor	0.55	0.313	0.37

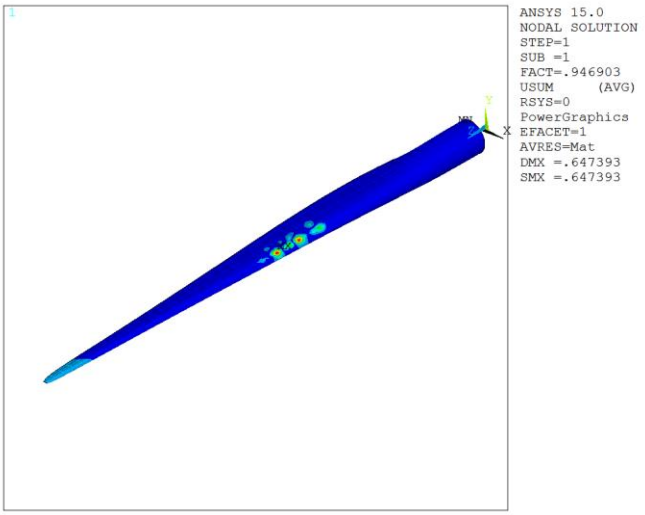

Figure 5.4-2 1st Buckling mode shape, C/Ep Blade

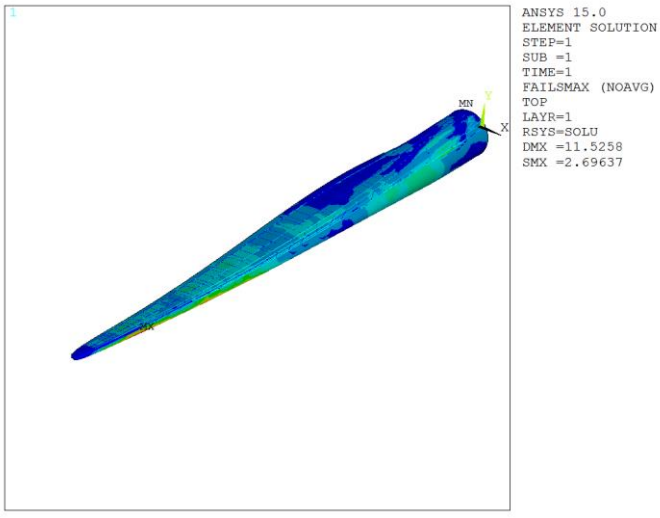

Figure 5.4-3 Failure pattern of C/Ep blade under the reference load

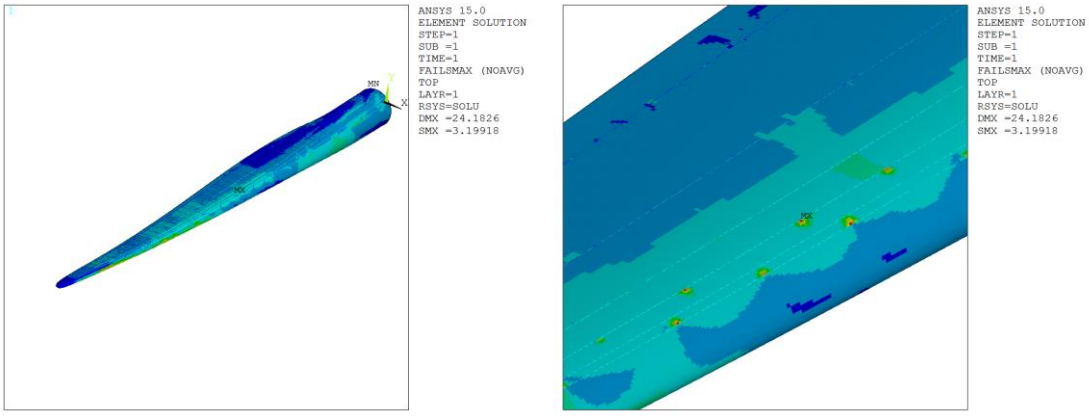

Figure 5.4-4 Failure pattern of Gl/Ep blade under the reference load

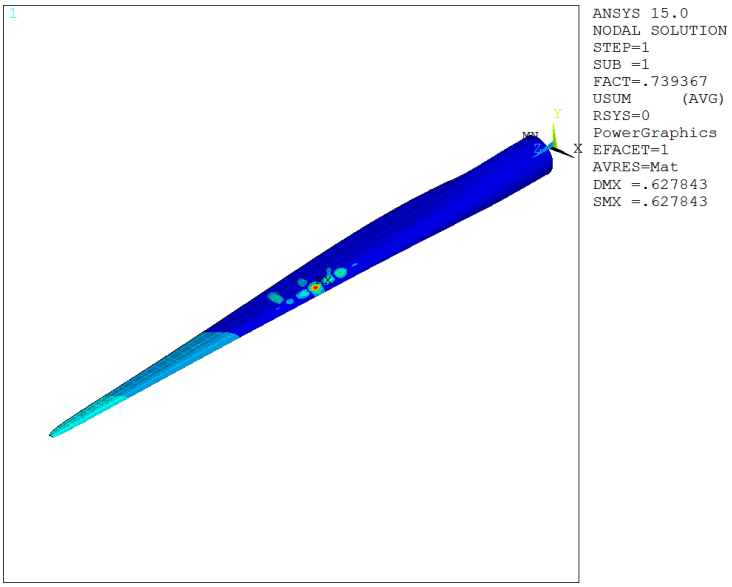

Figure 5.4-5 1st Buckling mode shape, Gl/Ep Blade

A comparison of the natural frequencies is presented in Table 5.5, while indicatively the modes shapes of the C/Ep blade are presented in Figure 5.4-6.

Table 5.5 - Natural frequency comparison

Mode Number	Reference Blade	Gl/Ep Blade	C/Ep Blade
1	0.6095	0.3828	0.6767
2	0.9477	0.5470	0.7553
3	1.7486	1.2741	2.0568
4	2.8333	1.9344	2.5921
5	3.5714	2.5895	3.7984

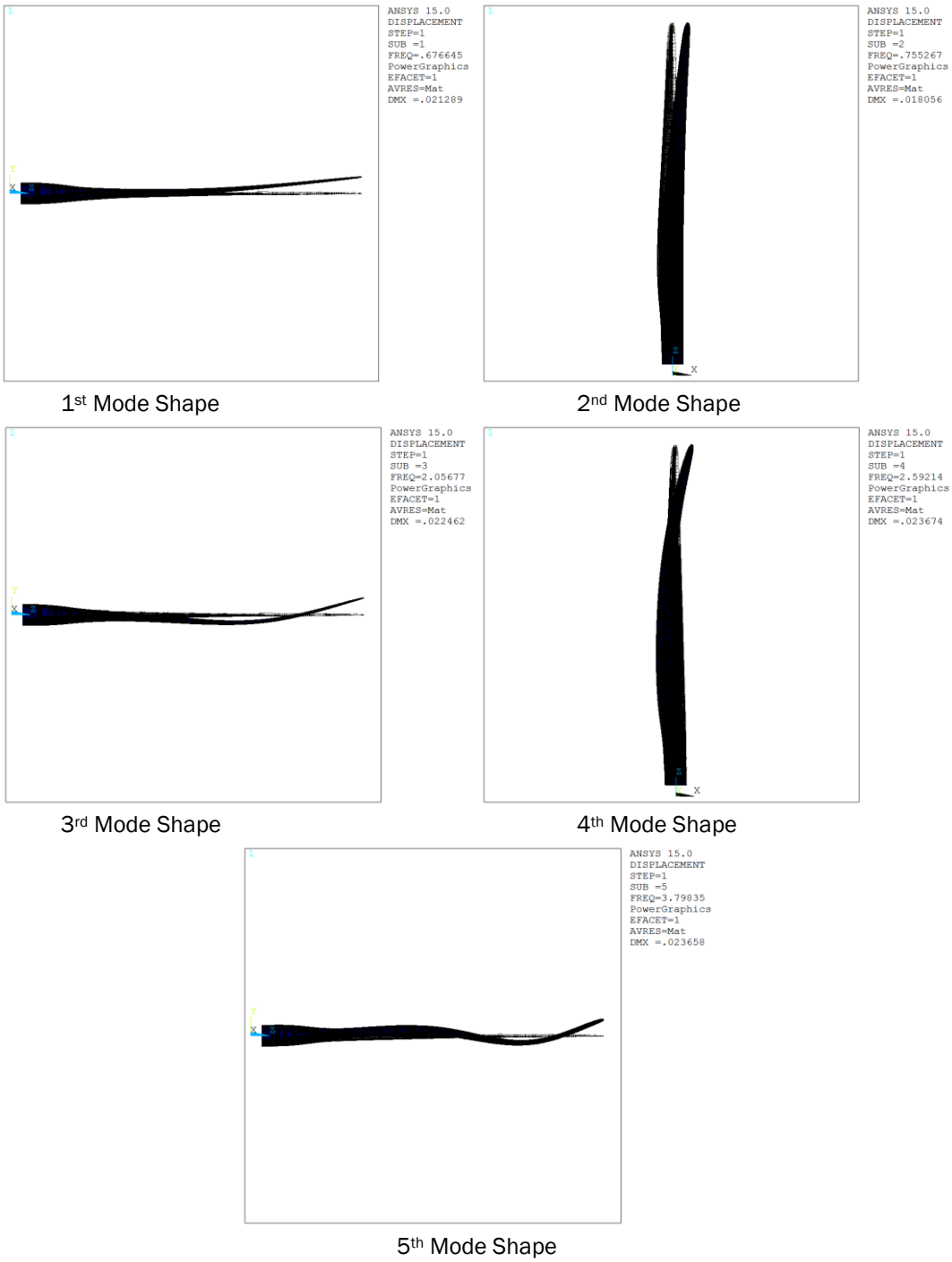

Figure 5.4-6 Mode Shapes, C/Ep Blade

At this stage it should be also noted that no aeroelastic calculations were performed to identify the loading on the blade employing the new design. The mass reduction achieved is expected to lead also to a reduction of the loading of the blade.

5.5 LCOE Impact of the Proposed Design

Since there are no alterations on the aerodynamic design of the reference blade, there is no effect on the annual energy production by the structural design concept proposed. The same goes for the OPEX, since the wind turbine blade has no additional systems, while the design life of the blade covers the design life time of the wind turbine without foreseen replacements of parts under regular maintenance procedures. The innovative internal structural solution presented will, nevertheless, have an impact on the levelized cost of energy (LCOE) through the effect of the design on the CAPEX.

It should be noted that at this stage of technology maturity for the innovative structural solution investigated the cost estimation is rather difficult and based only on knowledge of the cost of the internal structural parts (truss members). The effect of the manufacturing cost for the build-up of the internal truss structure including the joints of the truss members is unknown for structures of size similar to the wind turbine blade in study. Thus, uncertainty in cost estimations is inherent for this solution.

The cost model used is therefore weight based only; it is assumed that the manufacturing savings from using standardized truss members will compensate the labour cost of joining the truss members. For the solution employing carbon fibres, the cost model, suitable for hybrid blades, presented under Section 2.3.2, is used.

It shall be noted that the results of UPAT within the benchmark showed the mass of the reference blade to be 42379.3kg, instead of 41716kg used in the CAPEX estimations within the present report. Thus, a correction factor of 41716/42379.3 = 0.984 will be used to UPAT mass results for all blade cases. The cost of the all glass blade incorporating an internal truss structure (of glass/epoxy truss members) is directly estimated (in prices of 2002) using the cost model of INNWIND.EU as *13.084*(0.984*39932.6)-4452.2=509,666$* instead of 541,360$ for the cost of the reference blade. This in turn results for the LCOE to 91.27€/MWh, instead of 91.93€/MWh for the reference wind turbine; i.e. leading to a minimal LCOE reduction.

For the case of the hybrid carbon/glass blade, the procedure presented in Section 2.3.2 is used, employing the conservative ratio of cost of Carbon fibres over Glass to 3.

Baseline for the case:

13.084(0.98*30841.6)-4452= 392,623$*

Ratio of using carbon over all glass for a 89m rotor:

(1-0.4134) + (0.4134)(1-0.60)+0.4134*0.6*(1-0.4)+0.4134*0.6*0.4*3 =* ***1.198***

Therefore cost of the hybrid blade is estimated to: 470,532$

This cost, when inserted in the cost estimation tool of INNWIND.EU results in a LCOE of 91.38 €/MWh, which indicates a potential of reducing the LCOE of the reference wind turbine by 0.6%.

5.6 Conclusions and recommendations

The structural design of an internal truss instead of the traditional spar-box faces a lot of challenges when Gl/Ep materials are used. The most important one is the elastic instability of the blade's skin. A replacement of the sandwich structure with a more flexible material seems an appropriate solution to be investigated.

On the other hand, the replacement of the Gl/Ep longitudinal beams with C/Ep ones improves the performance of the blade significantly. The results show that by replacing the 45% of the Gl/Ep with C/Ep beams in the space truss the stiffness of the blade will improve by almost 100%, already with a ca. 27% lighter blade than the reference. This suggests that a much lighter construction might be finally achieved that will compensate for any cost increase due to material or assembly and joining complexities.

CHAPTER 6 BEND-TWIST COUPLED BLADE

6.1 Introduction to the Innovative Concept

6.1.1 State of the art and motivation

In this project PoliMI presents a structural solution based on the so called Bend-Twist Coupling (BTC), a solution aimed to achieve a particular behavior of the blade: its structure, when loaded, deforms so as to induce a load reduction. In fact BTC implies that, when the blade bends because of increased loads, the ensuing change of twist will affect the aerodynamic loading through a change in angle of attack. Passive load mitigation by BTC can be obtained by exploiting the anisotropic mechanical properties of composite materials [32], [33].

This form of load alleviation is in principle very attractive because of its passive nature: there are no actuators which may fail, no moving parts which may wear out, and no need for sensors, all characteristics that are very interesting for wind turbines where simplicity, low maintenance and high availability are keys to reducing the Cost of Energy (CoE). However, as usual in the design of wind turbines or other complex engineering systems, the benefits of BTC blades may be accompanied by other undesirable effects, such as a reduction in power production, an increase of weight and of manufacturing complexity and thus possibly cost.

Modern approach to BTC is to twist the blade sections so as to decrease the angle of attack, the so called twist-to-feather concept [34], [35]. This method showed significant fatigue damage reduction. To analyse the behaviour of such design solution, aeroelastic simulation models have been developed where the level of coupling between blade bending and twisting was obtained by directly modifying the beam stiffness sectional properties.
In order to better understand the real benefits of BTC, in this project PoliMI has followed the approach presented in [36], where parametric studies, obtained changing the coupling, have been performed within a design framework in order to compare optimal blades which simultaneously satisfy all the design constraints.

6.1.2 Brief description of the concept

In order to find the optimal solution for the specified blade, a series of parametric studies is done by rotating the plies of the spar caps and/or of the skin for the whole span-wise extension of the blade. For each solution the blade design is performed with a constrained optimization-based procedure that sizes the structural blade elements by minimizing a cost function [37].

All design requirements are treated as constraints, therefore all converged solutions are viable according to the conditions that have been imposed by the designer, and therefore they could all be adopted. The design optimization software, an evolution described in [38] and [37], performs the design using a multi-level approach.

The method includes 2D finite element models for sectional characterization and analysis, aero-servo-elastic multibody models for load calculation according to certification rules, and detailed 3D finite element models for detailed stress-strain, fatigue and buckling

analysis. The optimizer operates at and iterates among the various levels, so as to deliver in reasonable computational times a cost-minimizing design solution that also satisfies all desired design constraints at the finest description level, i.e. the detailed 3D model.

Optimization-based Multi-level Method for Blade Design

Optimization tools for rotor blades have been recently developed to aid the design process of these complex structures, and a review of the literature is offered in [37]. In this work, we use the design approach developed in [38] based on the earlier results of [37], and implemented in the code Cp-Max (Code for Performance Maximization). For computational efficiency, the design is performed as a sequence of nested optimizations that operate at various description levels of the blade: a quasi-3D “coarse" representation which is made up of a 2D FEM cross-sectional model together with a spatial beam model and a detailed “fine" 3D FEM model.

At first, the blade structural configuration and material properties are defined. Next, the sectional structural configuration is parametrized, thereby defining the design variables, which include the thickness of skin, shear webs, spar cap, and the area of leading and trailing edge reinforcements. Such variables are defined for selected span-wise stations, and interpolated elsewhere along the span using shape functions. Sectional models are defined using either 2D finite element meshes modeling the stack sequence of plies or using equivalent panels. From the sectional models, fully-populated stiffness matrices are computed using the code ANBA (Anisotropic Beam Analysis), based on the anisotropic beam theory of [39]. The stiffness matrices obtained in this way are used for defining a geometrically exact shear and torsion-deformable beam model [40]. The resulting beam is used in a complete aero-servo-elastic model of the machine, implemented here with the comprehensive non-linear finite-element-based multibody dynamics simulator Cp-Lambda (Code for Performance, Loads, Aero-Elasticity by Multi-Body Dynamic Analysis) [41] [42].

Transient design load cases (DLCs) are simulated using the aero-servo-elastic model. The results are post-processed to determine the maximum tip deflection and to extract at a number of span-wise verification sections the envelope loads, i.e. the maximum and minimum values of the internal stress resultants. At each verification section, maximum stresses and strains are computed at a number of verification spots on the cross section from the envelope loads, using recovery relations [39] obtained by the sectional analysis with ANBA. At the same verification spots, fatigue damage is computed from the stress time histories through rainflow counting and the associated Markov matrices. The computed maximum tip deflection and the maximum stresses, strains and fatigue at each verification spot for each verification section are enforced as inequality constraints for the optimization problem, including the necessary safety factors. A Campbell diagram of the machine is computed using the aero-elastic model. A design free of resonant conditions is obtained by constraining the placement of natural frequencies away from strong harmonic excitations; here this was obtained by simply prescribing a given minimum gap between the first blade flap frequency and the three-per-rev at the rated rotor speed, enforced as an inequality constraint in the optimization. Additional inequality constraints are defined to enforce conditions on the design variables, such as a maximum thickness rate of change to account for typical values of ply tapering. From the structural configuration of the blade and its sectional description, the total mass can be readily computed, accounting also for the non-structural mass due to surface coating, foam core, resin take-up, junction adhesive, etc. The total mass defines the cost function for the optimization problem. The optimization is run until convergence, using a Sequential Quadratic Programming (SQP) algorithm with gradients computed by finite differences. For each new instantiation of the

design variables, the 2D cross-sectional analysis is repeated, generating a new blade model and hence a new aero-servo-elastic wind turbine model. For each new model, the necessary analyses are repeated to update cost function and constraints. To reduce the computational cost and minimize the number of evaluations of the full set of DLCs, which is the most expensive part of the optimization, an outer iteration is used where the loads are temporarily frozen until the blade mass has converged and all constraints are satisfied; loads are then updated at the next iteration by repeating the DLCs, as explained in detail in Ref. [37].

At convergence of the blade optimization conducted at the coarse level using 2D cross-sectional and aero-servo-elastic beam-based models, a 3D CAD solid model of the blade is generated automatically by lofting the computed blade geometry. The CAD model accounts for all blade parts including webs, web core, spar caps, leading and trailing edge reinforcements, internal skin, skin core and external skin, associated with the corresponding material properties and laminate characteristics.

Finally, a buckling analysis is performed. If buckling is detected, the core thickness is increased using a heuristic approach. The modified core thickness modifies the non-structural mass of the cross-sectional model, this way again closing the loop between fine and coarse level analyses. Based on the updated constraint conditions and updated model computed at the 3D FEM analysis level, new 2D sectional models are generated which in turn define a new beam model, and the complete process is repeated. Typically, two or three iterations between the coarse and fine levels are necessary for convergence.

Short description of structural analysis tool(s) used

The 3D finite element model is developed in MSC Nastran 2012 format. The mesh procedure is obtained by Hypermesh while the properties definition is performed by Matlab functions. Elements are placed in mid thickness position while local lamination sequence is defined by PCOMP card. Orthotropic materials are set by MAT8 card, while isotropic materials are modelled by MAT1. Further data are reported in following table.

Entity	Number
CTRIA3 (triangular plate element)	1196
CQUAD4 (quadrilateral plate element)	138132
RBE3 (interpolation constraint element)	29

Table 6.1-1: FEM constitutive elements

The RBE3 elements are used to applied loads on the blade FEM model. The loads distribution is discretized and applied to 29 nodes along blade span. The RBE3 allows distributing the applied loads to elements defining the spar caps on suction and pressure side.

The first RBE3, in the root section, is also linked to all the elements, as shown in figure below. This allows to correctly redistributing the loads in the root section.

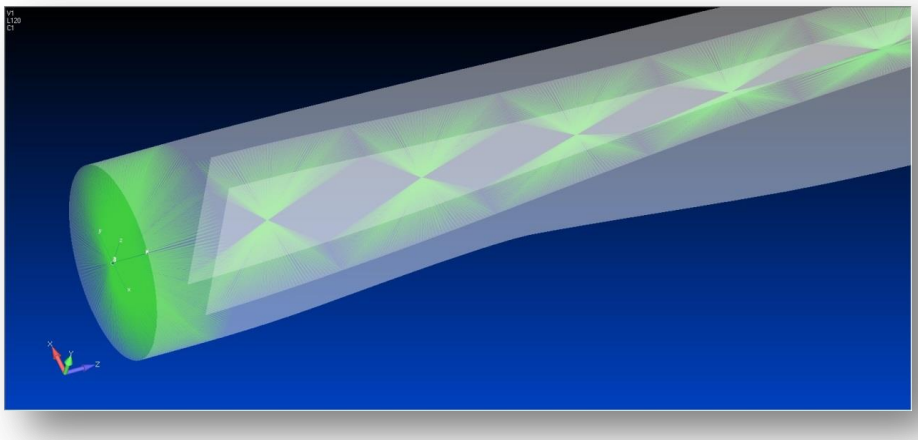

Figure 6.1-1: RBE3 elements

The applied constraint involve the displacements of the nodes at the blade root in direction x, y and z, while the rotations are free. This constrain set is applied for all considered analysis.

For the analysis of the extraction of blade properties

Sectional models are defined using either 2D finite element meshes modelling the stack sequence of plies or using equivalent panels. In this case the latter approach has been used. From the sectional models, fully-populated stiffness matrices are computed using the code ANBA (Anisotropic Beam Analysis), based on the anisotropic beam theory of [39]. From this sectional analysis code a six by six stiffness matrices and the mass matrix are obtained.

Failure criterion used

The failure criteria is based on the definition of a safety margin which compares the loading state in a specific point (for both stress and strain) with the allowable values defined for the material of the ply. A safety margin lower than zero means that the failure criteria are not satisfied.

Fatigue analysis

The RBE3 elements are used to applied static unit loads onto the structure.

The stress time histories necessary for evaluating the damage index are conveniently computed by exploiting the linear superposition of static unit load cases applied to the FE model with load histories obtained from the beam model, [43].

At each verification point, a static force or moment (in the case of shells) of unit magnitude is applied, and the full stress time history follows as:

$$\sigma_i(t) = \sum_j P_j(t) \frac{\sigma_{ij}}{P_{j,FEA}}$$

where $P_j(t)$ denotes a load history obtained by a multibody transient simulation, $P_{j,FEA}$ the applied unit load, and σ_{ij} is the static stress resultant at point i for load case j. Each time step of the loads history $P_j(t)$, for sake of simplicity, is discretized through the direct discretization of the internal force. This choice allows to consider all the dynamic contributions included into internal forces that are provided by the multibody software. Even if the stresses $\sigma_i(t)$ are obtained by static analysis, the effects of inertial loads and time variant aerodynamic effects are considered because they are naturally included into internal forces evaluation.

So this procedure reduces the computational cost necessary for the evaluation of the full stress time history on the comprehensive 3D FE model.

On each verification point the fatigue damage d_{σ_r} due to single stress component is computed according to [44]:

$$d_{\sigma_r} = \sum_{i,j,k} F_{V_k} \frac{n(\sigma_{m_i}, \sigma_{a_i}, V_k)}{N(\sigma_{m_i}, \sigma_{a_i}, \sigma_{adm}, \gamma)}$$

where F_{V_k} is given by the ratio between the time spent by the wind turbine during the entire operative life at wind speed V_k and the simulated time. $n(\sigma_{m_i}, \sigma_{a_i}, V_k)$ is the number of cycles obtained by the rain-flow counting algorithm at mean stress σ_{m_i}, amplitude stress σ_{a_i} and wind speed V_k. The admissible number of cycles is $N(\sigma_{m_i}, \sigma_{a_i}, \sigma_{adm}, \gamma)$, corrected by the safety factor γ.

From the value of σ_r of each stress component, a damage index is defined in agreement with [45], [46] considering only the longitudinal component:

$$D = d_{\sigma_L}^{2/m}$$

Where m is the inverse slope of the Wöhler curve and the longitudinal stress components is identified by indices L.

Failure is predicted if D > 1.0.

Buckling analysis

Linear buckling analysis is performed by MSC Nastran 2012. All the dimensioning load cases used for the optimization process plus the load condition corresponding to max blade tip deflection are considered. Six eigenvalues are computed, which represent the critical load factor. A value > 1 means the critical load associated to buckling is higher than the actual load.
Buckling is prevented by using balsa core in panels of skin and webs, whilst spar cap thickness is adjusted (i.e. increased) to avoid buckling all along the span.
For buckling analysis a safety factor of 2.0419 is applied reducing material capability to withstand maximum loads.

6.1.3 Anticipated PROS and CONS

The literature clearly shows the potential benefits of BTC. Many parametric studies have been performed using models of different levels of complexity and fidelity, yielding a good insight on what can be expected by the adoption of such a technological solution. However a comprehensive approach to the design of such complex structures is still lacking. In fact,

when designing for a specific set of given conditions (e.g., rated power, wind class, rotor diameter, max tip deflection, etc.), one should be able to compare alternative solutions that all satisfy the same design constraints. Only if all alternatives are fully viable, one can then identify the one that is the most desirable according to given criteria or performance metrics. This aspect is of crucial importance in the design of blades for large modern wind turbines, given the complex couplings that exist among the various design requirements. For example, changes in bending stiffness due to fiber rotation must be compensated by increasing the thickness of spars and skin, or by using more performing materials, so as to satisfy max deflections and frequency placement constraints. However, these changes will not only influence weight, but also fatigue and buckling. In turn, the satisfaction of the fatigue and buckling constraints will again influence the sizing of the various structural members of the blade, creating a further coupling. Many other subtle effects are present: for example, different degrees of BTC will induce different mean deflected blade configurations at each mean wind speed, thereby affecting trim and hence power. To restore power to the same level, again so as to perform meaningful comparisons among different candidate solutions with different degrees of BTC, one should then change the trim pitch setting, and this will in turn modify loads, which will again induce a coupling effect in the design and can lower BTC benefits. The twist-to-feather characteristic of a BTC blade, leads to multiple benefits in terms of ultimate and fatigue loads, but at the same time, is accompanied by a higher torsion of the blade, which reflects in a lower power production. Through changing the trim pitch setting is possible to restore power to its initial value, but the potential benefits of BTC are hence mitigated.

All these aspects have been considered in the solutions presented in this project: the blades have been re-designed within an optimization design framework in order to account all these constraints. The final goal is to reduce the CoE which accounts for the mass of the blade as well as for the Annual Energy Production (AEP). All the solutions presented here are able to reduce the CoE and, in the meanwhile, some of these are also able to reduce the loads on the hub and/or on the tower. Since these components have not been re-designed in this deliverable, the real effects on the CoE of these solutions have to be further investigated.

In the following sections PoliMI presents one structural solution (named “POLIMI 10MW BTC SC+05”) which has been computed moving the direction of the unidirectional fiberglass in the spar cap away from the blade axis with an angle of 5deg. This solution has been selected between eight distinct configurations analysed with Cp-Max because it exhibits preliminarily the best CoE reduction. The other optimal blades, satisfying all the design constraints, have been obtained changing the angle in the spar cap (SC) of 3, 4, 5, 6 and 7deg and in the skin (Sk) of 5, 10 and 15deg. The following figure shows the reduction of the CoE computed preliminarily with Cp-Max with respect to the RWT.

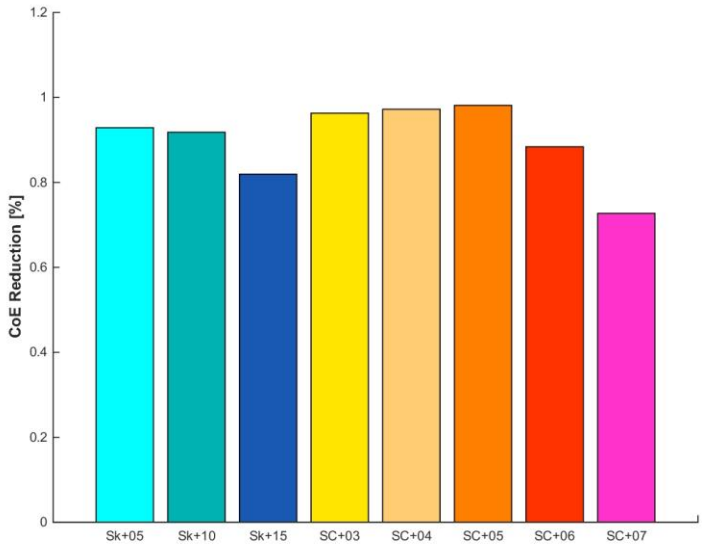

Figure 6.1-2: PoliMI BTC: CoE comparison between optimal blades

6.2 Assessment of the Structural Integrity of the Proposed Design

6.2.1 Design layout and dimensioning

The blade structural layout uses a box-type configuration, with a single cap confined within the two shear webs. The shear webs are parallel and planar, i.e. they do not follow the twist of the airfoils. A third shear web is located at 87% of the local chord, as in the reference wind turbine. Trailing and leading edge reinforcements are introduced to augment in-plane modal frequencies. Root reinforcement made of unidirectional fiberglass is also here used. To prevent buckling in skin and shear webs panels a sandwich with balsa core is used, while to prevent buckling in the spar caps panels the thickness of the spar caps are designed to be buckling-free.

The main blade parameters and material types used are reported in the following table, while the following figures show the adopted blade structure.

The material properties used within this task are the same of the DTU 10MW reference blade.

	Starting section (% span)	Ending section (% span)	Material type
Skin	0	100	Tri-axial fiberglass
Spar caps	0.025	98.12	Unidirectional fiberglass
Shear webs	0.025	98.12	Bi-axial fiberglass
Third shear web	0.22	95	Tri-axial fiberglass
Trailing and leading	0.10	95	Unidirectional

	Starting section (% span)	Ending section (% span)	Material type
edge reinforcement			fiberglass
Root reinforcement	0	30	Unidirectional fiberglass

Table 6.2-1: PoliMI BTC SC+05, main blade parameters and material types

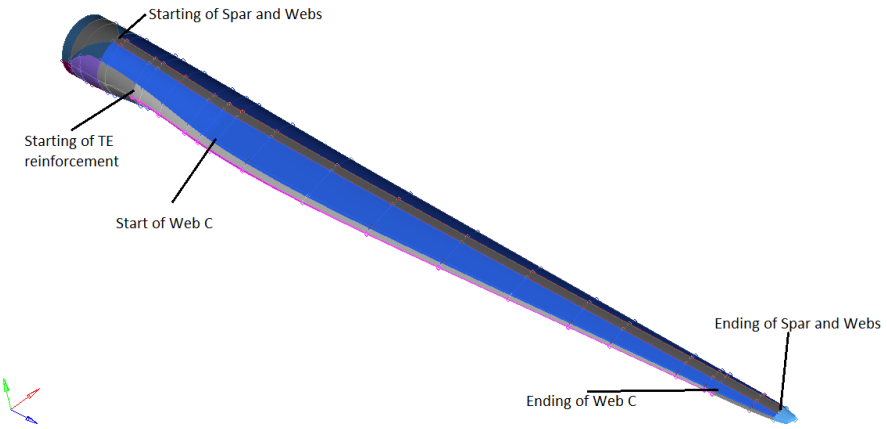

Figure 6.2-1: PoliMI BTC SC+05, blade's structure and position of constitutive elements

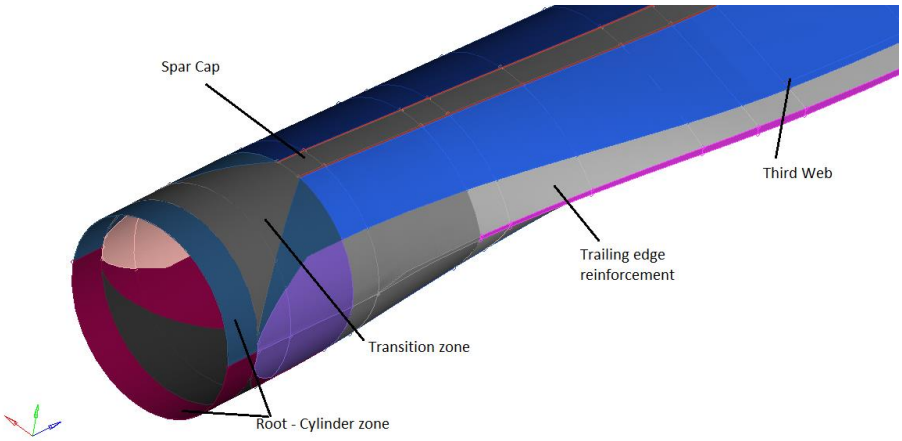

Figure 6.2-2: PoliMI BTC SC+05, root details

The wind turbine design parameters are the same of the DTU 10MW reference blade, and are reported in the following table for completeness.

Wind regime	IEC Class 1A
Rotor Orientation	Clockwise rotation – Upwind
Control	Variable speed, collective pitch
Cut in wind speed	4 m/s
Cut out wind speed	25 m/s
Rated wind speed	11.4 m/s
Rotor Diameter	178.3 m
Hub Diameter	5.6 m
Hub Height	119 m
Maximum Tip Speed	90 m/s
Tilt Angle	5.0 deg
Rotor Precone Angle	4.65 deg
Blade Prebend	0 m
Nacelle Mass	446.036 kg
Tower Mass	628.442 kg

Table 6.2-2: PoliMI BTC SC+05, design parameters

The following table reports the global data of the optimal blade POLIMI BTC SC+05.

	PoliMI BTC SC+05
Spar Caps Angle Rotation	5 deg
1st blade frequency (flap mode)	0.5587 Hz
2nd blade frequency (edge mode)	0.6173 Hz
Max Blade Tip Deflection	12.90 m
Blade Total Mass	40874 kg
AEP	46.160 GWh/y
CoE	74.91 €/MWh

Table 6.2-3: PoliMI BTC SC+05, global data

The following table reports the mass breakdown computed for each structural components including the Non-Structural Masses (NSM). The figures below report the thickness distributions along the blade span of the internal sub-components and the mass, flapwise and edgewise stiffness.

Structural Component	Mass [kg]	% of total blade mass
Skin	8883	21.73
Spar Cap	16884	41.30
Web A + B	2413	5.90
Web C	72	0.17
LE & TE Reinforcement	1284	3.14
Root Reinforcement	2568	6.28
Total Structural Mass	32104	78.54
NSM	8770	21.46
Total blade mass	**40874**	100

Table 6.2-4: PoliMI BTC SC+05, bill of material

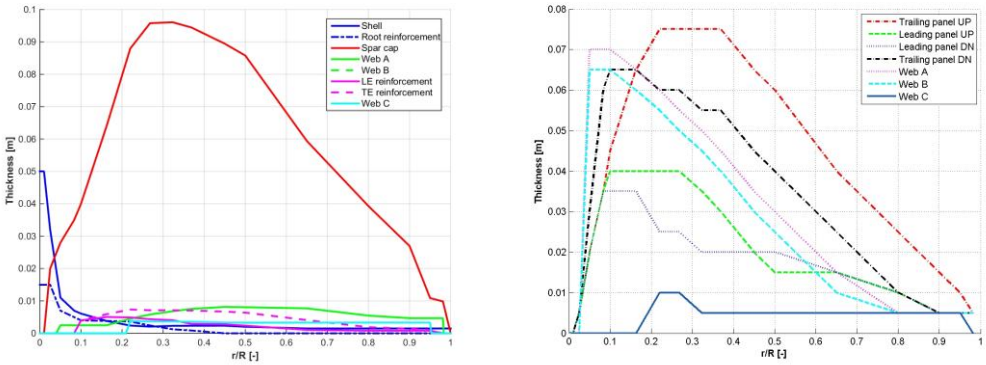

Figure 6.2-3: PoliMI BTC SC+05, structural (left) and core (right) thickness distributions

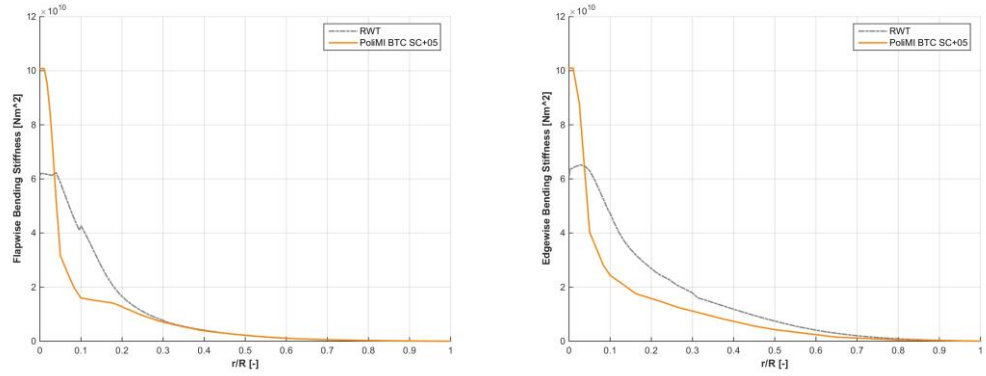

Figure 6.2-4: flapwise (left) and edgewise (right) stiffness distributions comparison

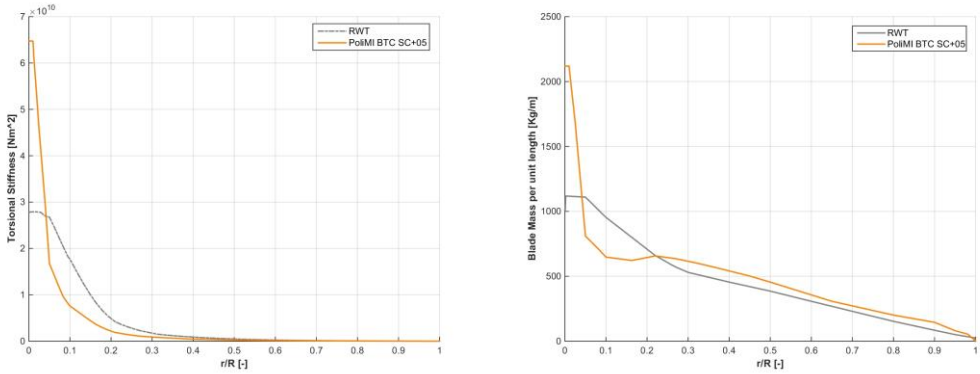

Figure 6.2-5: torsional stiffness (left) and blade mass (right) distributions comparison

The next figures show the deflection of the blade in the out of plane direction in correspondence of the first mode of vibration (at left) and the corresponding torsion associated to the blade (at right). The PoliMI BTC 10MW SC+05 blade has, for the same flapwise deformation, a higher twist due to the BTC.

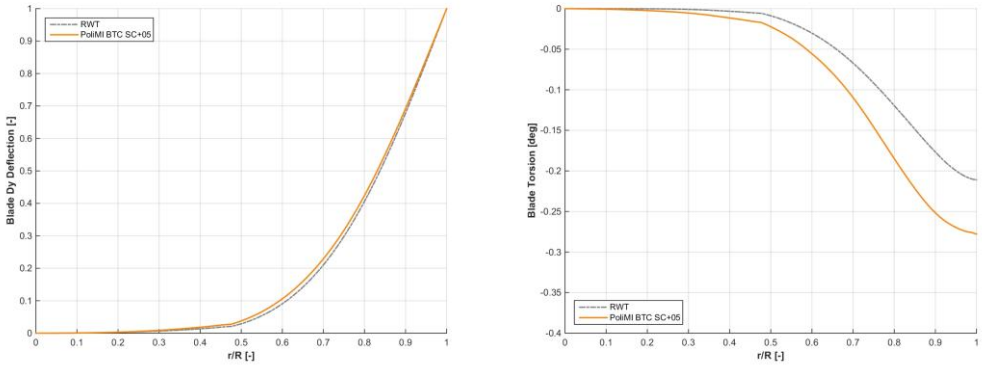

Figure 6.2-6: First flapwise mode: flapwise (left) and torsion (right) deflections comparison

Next is presented a comparison between the DTU 10MW RWT and the actual PoliMI 10MW BTC SC+05. The following table shows a comparison between the RWT blade and the optimal one.

	RWT	PoliMI BTC SC+05	difference
Blade Total Mass	42422 kg	40874 kg	- 3.65 %
Blade 1st modal freq (flap)	0.6123 Hz	0.5587 Hz	-
Blade 2nd modal freq (edge)	0.9124 Hz	0.6173 Hz	-
Blade Max Tip Displ.	13.04 m	12.90 m	-
CG position (spanwise direction)	26.62 m	28.56 m	-
AEP	45.760 GWh/y	46.160 GWh/y	+ 0.87 %
CoE	75.680 €/MWh	74.913 €/MWh	- 1.01 %

Table 6.2-5: PoliMI BTC SC+05 wrt RWT

6.2.2 Load cases considered

The blade is designed according to IEC 61400-1 Ed.3. The load cases selected for the design are reported in the following table.

DLC number	Wind Type	Wind Speed	Yaw Misalignment	Fault	Type of Analysis	Safety factor
1.1	NTM	4 – 5:2:25 m/s	-	-	U	1.35
1.2	NTM	4 – 5:2:25 m/s	-	-	F	1
1.3	ETM	4 – 5:2:25 m/s	-	-	U	1.35
2.1	NTM	4 – 5:2:25 m/s	-	Grid Loss	U	1.35
2.3	EOG	Vr, Vr-2, Vr+2, Vout	-	Grid Loss	U	1.1
6.1	EWM	Vref (50m/s)	-8, 0, +8 deg		U	1.35
6.2	EWM	Vref (50m/s)	-180:30:180 deg	Grid Loss	U	1.1
6.3	EWM	Vref (50m/s)	-20, 0, +20 deg		U	1.1

Table 6.2-6: PoliMI BTC SC+05, DLCs considered

A complete set of load cases, including also DLC 1.4, DLC 1.5, DLC 4.2, was at first considered. For computational reasons, this reduced set was taken as representative of the complete envelope loads along the entire spanwise of the blade.

A complete description of the blade characteristics may be found in the attached file "PoliMI_10MW_BTC_SC05.xlsx".

6.2.3 Structural integrity verification

The proposed blade satisfies all the design constraints, as can be seen from the following figures, which report the constraint margin for stress, strain and fatigue analysis in all the structural components of the blade as described in the previous sections.

A constraint value is considered active when its value reaches 0 (within the optimization tolerance). If the value is positive the constraint is violated, if negative it is satisfied. As one can see, only the fatigue constraint is active in the first 3 figures, which are relatives to skin, spar cap and webs. The other sub-component thicknesses are selected to satisfy the other global constraints (frequency placements above all).

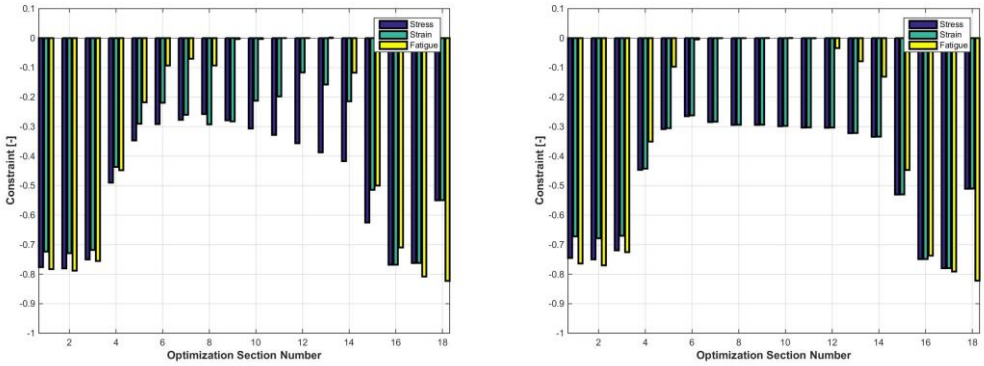

Figure 6.2-7: PoliMI BTC SC+05: skin (left) and spar cap (right) constraints

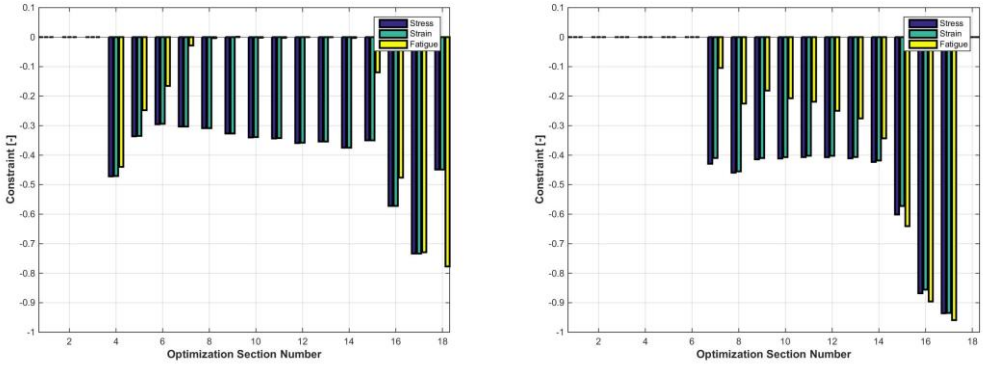

Figure 6.2-8: PoliMI BTC SC+05: web (left) and TE reinforcement (right) constraints

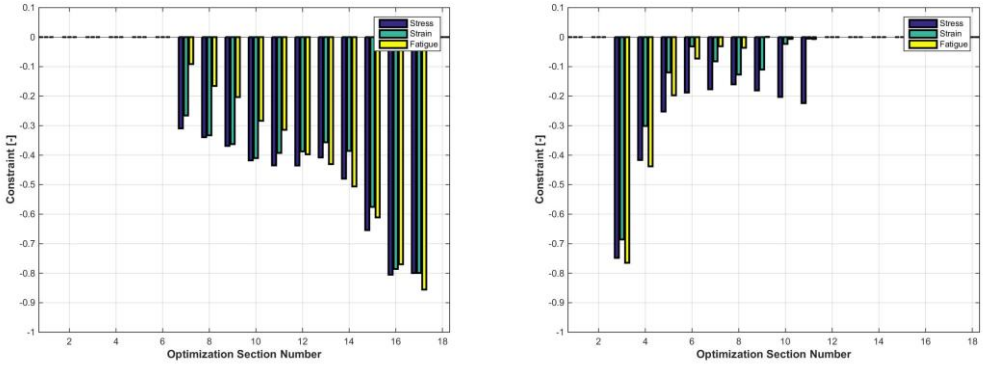

Figure 6.2-9: PoliMI BTC SC+05: LE reinforcement (left) and root reinforcement (right) constraints

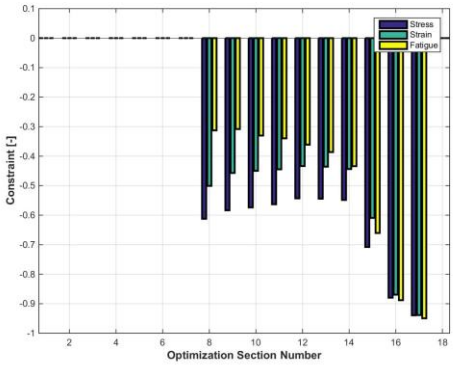

Figure 6.2-10: PoliMI BTC SC+05: third web constraints

The following table shows the ultimate loads on the hub and tower compared with the ones computed (with the same conditions) for the RWT. As one can see the BTC is able to reduce all these loads on these two subcomponents. Since these have not been re-designed in this deliverable, the real effects on the CoE of this optimal blade have to be further investigated.

	RWT	PoliMI BTC SC+05	difference
Hub Nodding Moment	57097 kNm	53908 kNm	- 5.58 %
Hub Yaw Moment	53046 kNm	47078 kNm	- 11.25 %
Hub Combined Moment	58271 kNm	54121 kNm	- 7.13 %
Hub Axial Force	3560 kN	3121 kN	- 12.33 %
Tower Bottom Fore-Aft Moment	491819 kNm	463849 kNm	- 5.68 %
Tower Bottom Combined Moment	495794 kNm	463855 kNm	- 6.44 %
Tower Bottom Torsional Moment	59056 kNm	51513 kNm	- 12.77 %
Tower Top Fore-Aft Bending Moment	59244 kNm	54401 kNm	- 8.17 %
Tower Top Torsional Moment	58688 kNm	51270 kNm	- 12.63 %

Table 6.2-7: PoliMI BTC SC+05, comparison of ultimate loads against RWT

Fatigue loads:

The next table shows the cumulative damage equivalent loads computed considering only DLC12 cases (power production in turbulent wind). A Weibull distribution has been used, with a shape factor of 2 and a mean wind speed of 10m/s. Damage Equivalent Load (DEL) are weighted with Weibull. Following parameters are chosen for the fatigue analysis, for both the blades:

- Number of bin: 100

- Number of years: 25
- Frequency: 0.012684 Hz
- m = 3

It can be seen that the optimal blade with BTC is able to reduce the fatigue loads of about 3% in the hub and 2% in tower bottom. As for the ultimate loads, since tower and hub have not been re-designed in this deliverable, the real effects on the CoE of this optimal blade have to be further investigated.

	RWT	PoliMI BTC SC+05	difference
DEL Hub Nodding Moment	27950 kNm	26884 kNm	- 3.82 %
DEL Hub Yaw Moment	26192 kNm	25270 kNm	- 3.52 %
DEL Tower Bottom Side-Side Moment	59828 kNm	58175 kNm	- 2.76 %
DEL Tower Bottom Fore-Aft Moment	136805 kNm	135267 kNm	- 1.12 %

Table 6.2-8: PoliMI BTC SC+05, comparison of fatigue DEL against RWT

The 3D finite element model was also used to check fatigue satisfaction of the fatigue constraint. Check of fatigue damage index D is done on the three reference section also used in the Deliverable D2.2 *"Information on the Benchmark of blade structural FATIGUE models"* [47] and [48]. Section number and relative position are reported in table:

Section (-)	R (m)
RefSec_1	2.800
RefSec_2	26.694
RefSec_4	54.149

Table 6.2-9: PoliMI BTC SC+05, reference sections used for FE fatigue verification

In the following figure is reported the fatigue damage index D on the skin in *RefSec_2*. As one can see, the suction side leading panel of the skin exhibits higher fatigue loads, but the analysis shows that the index is lower than one, confirming the satisfaction of fatigue analysis. The maximum fatigue damage index computed is 0.958.

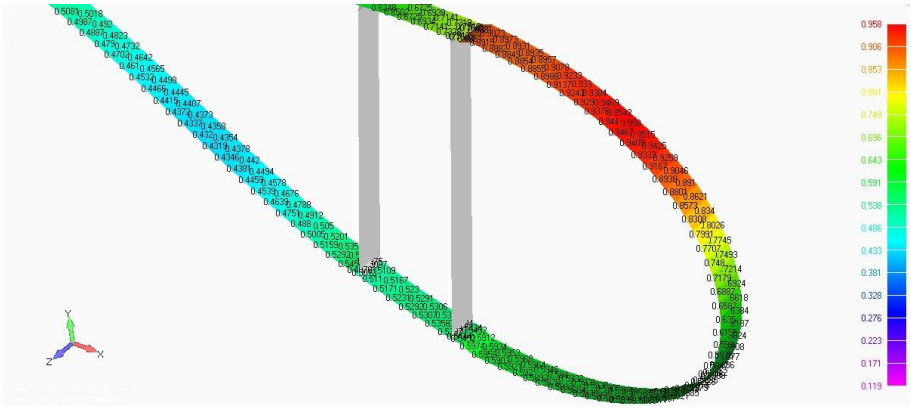

Figure 6.2-11: PoliMI BTC SC+05, fatigue damage index on skin on RefSec_2

In [47] the fatigue damage index was requested in some specified key points (KP1, KP5, KP9, KP12) on the three reference sections selected. Even if the internal structure of the PoliMI 10MW BTC SC+05 is slightly different from the RWT, these fatigue analysis has been repeated in the points which are closer to the original ones. The analysis has showed that all the fatigue constraints are satisfied (fatigue damage less than 1).

Key point No.	Layup	RefSec_1		
		Laminate	Layer 1	Layer 2
1	Tail A	0.1371	0.1371	0.1116
9	Nose P	0.1591	0.1591	0.1433
12	CAP	0.2687	0.2687	0.2273

Table 6.2-10: PoliMI BTC SC+05, fatigue damage index on RefSec_1

Key point No.	Layup	RefSec_2		
		Laminate	Layer 1	Layer 2
1	Tail A	0.7296	0.7296	0.7286
5	Trailing	0.4976	0.4976	0.4475
5	CAP	0.511	0.5110	0.4330
5	Web B	0.7628	0.7628	-
9	Nose P	0.6384	0.6384	0.6244
12	CAP	0.6725	0.6725	0.6384

Table 6.2-11: PoliMI BTC SC+05, fatigue damage index on RefSec_2

Key point No.	Layup	RefSec_4		
		Laminate	Layer 1	Layer 2
1	Tail A	0.6691	0.6687	0.6691
5	Trailing	0.5107	0.5107	0.4556

Key point No.	Layup	RefSec_4		
		Laminate	Layer 1	Layer 2
5	CAP	0.5303	0.5303	0.4728
5	Web B	0.6412	0.6412	-
9	Nose P	0.4074	0.4023	0.4074
12	CAP	0.6991	0.6991	0.6803

Table 6.2-12: PoliMI BTC SC+05, fatigue damage index on RefSec_4

Buckling analysis:

The first buckling eigenvalues appears at suction side between 4.0m and 10.7m from the blade root, but the critical load is higher than actual load on the blade since the minimum buckling load factor computed is 1.0232 in the spar cap and leading edge panels as showed in the next figure. The safety factor on material is already been considered.

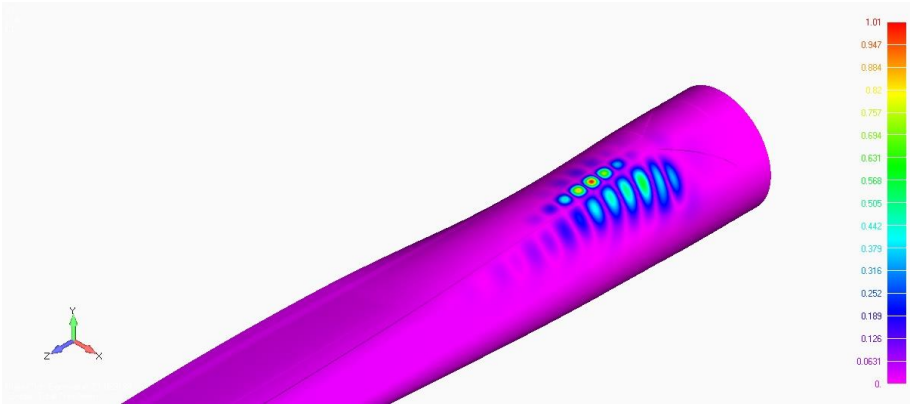

Figure 6.2-12: PoliMI BTC SC+05, FE buckling visualization

6.3 LCOE Impact of the Proposed Design

6.3.1 Effect on Annual Energy Production

The following figures show the power curve computed in turbulent condition for both the *PoliMI BTC SC+05* and the RWT. In region II the power of the new re-designed blade is, as expected, higher. The final AEP is in fact + 0.87 % higher. The figure on the right reports the standard deviation (STD) of the power curve compared against the STD of the RWT. This curve shows that, mainly in region III, the STD of the PoliMI blade is lower.

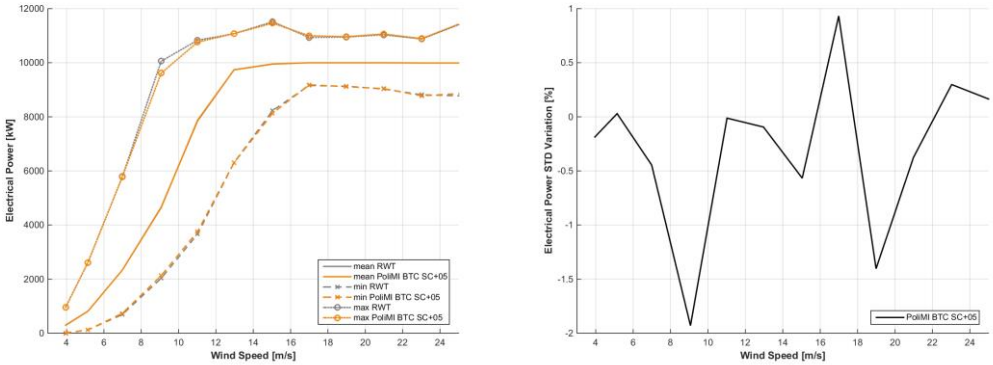

Figure 6.3-1: PoliMI BTC SC+05, turbulent power curve (left) and power STD variation (right), comparison against RWT

6.3.1 Effect on CAPEX

The effect of the reduction of blade mass (-3.65%) is evident in the reduction in Turbine Cost, even if this reduction is small (-0.58%).

	RWT	PoliMI BTC SC+05	difference
Turbine Cost [€/kW]	1376	1368	- 0.58 %
BoP Cost [€/kW]	1695	1695	-
Capital Investment [€/kW]	3071	3063	- 0.26 %
CAPEX (Turbine) [€/MWh]	22.19	21.86	- 1.49 %
CAPEX (BoP) [€/MWh]	27.33	27.09	- 0.88 %

Table 6.3-1: PoliMI BTC SC+05, contribution of CAPEX

BoP (Balance of Plant) does not change, because it is affected only by Nominal Power of the WT, which is the same, since the aerodynamic shape of the blade is not changed.
The higher AEP of the PoliMI BTC SC+05 blade, helps in reducing the CAPEX contribution to the total CoE.

6.3.2 Effect on OPEX

	RWT	PoliMI BTC SC+05	difference
DO&M [M€/y]	1.197	1.198	+ 0.10 %
AEP [GWh/y]	45.760	46.160	+ 0.87 %
OPEX [€/MWh]	26.17	25.96	- 0.80 %

Table 6.3-2: PoliMI BTC SC+05, contribution of OPEX

The higher AEP reflects in higher Operation and Maintenance costs (in the table is reported the DO&M, annual Discounted Operation and Maintenance cost), but the OPEX, which is the ratio between the two is lower (-0.80%).

The details of the CoE may be found in the attached file "*Costs Models v1.02 - PoliMI_BTC_SC05.xls*".

6.4 Conclusions and Recommendations

In this delivery PoliMI has presented a structural solution based on the so called Bend-Twist Coupling (BTC), a passive load mitigation solution obtained by exploiting the anisotropic mechanical properties of composite materials. BTC implies that, when the blade bends because of increased loads, the ensuing change of twist will affect the aerodynamic loading through a change in angle of attack.

The structural solution is computed throughout a blade design procedure based on a novel comprehensive multi-level constrained optimization approach. The design process alternates between a multibody beam model augmented with a 2D FEM cross sectional sub-models and a fine scale 3D FEM detailed model of the blade. The former enables the numerous transient aero-servo-elastic analyses required to compute loads and deflections throughout the lifetime of the machine, while the latter makes it possible to conduct detailed local verifications of the design.

The use of a constrained optimization-based approach to design is crucial and allows comparing different solutions that satisfy the same design requirements, and hence permitting to choose the optimal solution.

For each optimal blade, the control set-points have been changed in order to improve the annual energy production.

The optimal blade presented has several advantages with respect to the RWT: it is lighter (mass - 3%), has a higher AEP (+0.6%) and hence the Cost of Energy is lower, about - 1%. Last but not least, the ultimate as well as the fatigue loads on the hub and tower have been reduced. Since these components have not been re-designed within this task the actual final effect on the CoE of this optimal blade has to be further investigated.

Attached files

[1] PoliMI_10MW_BTC_SC05.xlsx
[2] Costs Models v1.02 - PoliMI_BTC_SC05.xls

CHAPTER 7 INTEGRATED BLADE DESIGN WITH BEND-TWIST COUPLING FOR INDIVIDUAL PITCH CONTROLLED ROTORS

7.1 Introduction to the Innovative Concept

7.1.1 State of the art and motivation

The re-design of the RWT blade inner structure, with the adoption of bend-twist coupling as presented in the previous Chapter shows the potential advantages of this passive load reduction technique in terms of both ultimate and fatigue loads. The blade mass therefore reduces, but, since the AEP is almost the same, the CoE drops slightly.

As observed in [49], the cost of energy model has a very high influence on the wind turbine rotor design: on dependence of the cost model adopted one can obtain a significant different optimal rotor design. The solution here proposed is based on the INNWIND cost model [5]. This model is mainly dependent on the annual energy production, while the blade total mass has a very small influence and the loads on the fixed frame (hub and/or tower) are not taken into account at all.

In order to influence more and more the CoE, (i.e. to increase the AEP) one solution could be stretching the blade while keeping constant the hub and tower loads (i.e. maintaining the same structure of the turbine).

To further limit the increase of ultimate loads on the hub, due to the extension of blade length, within a certain value, PoliMI considers in this integrated solution also the combined adoption of an individual pitch controller (IPC).

Active load control systems exploit a power source to move the whole blade, or a part of it, so as to reduce loads due to turbulence, gusts and asymmetry in the inflow. Generally these systems require sensors to measure the wind turbine response and drive, through a feedback loop, a suitable motion strategy. Recently, several IPC formulations have been proposed, demonstrating a significant potential for fatigue load reduction [50], [51], [52], [53], [54], [55], [56] and [57]. In fact, changing the pitch of each blade independently allows for the reduction of the lowest load harmonics, including their mean value.

Since BTC blades were shown to allow for a reduction in ultimate and fatigue loads as in solution proposed in Chapter. ("PoliMI 10MW BTC SC+05"), it is interesting to combine the two load control technologies, passive via BTC and active via IPC. In fact, on the one hand, since both BTC and IPC can reduce loads, by combining them one may obtain a synergistic effect. On the other hand, since BTC tends to reduce ADC and IPC to increase it, by combining the two one can hope to obtain significant load reductions with reduced ADC increases.

7.1.2 Brief description of the concept

A series of parametric studies is done increasing the rotor diameter of the structural solution proposed in Chapter 6 ("PoliMI 10MW BTC SC+05"). For each solution the blade design is performed with a constrained optimization-based procedure that sizes the structural blade elements by minimizing a cost function [37], [38] and [39] through the procedure indicated in section 6.1.2.

Since the combined adoption of BTC and IPC, as shown in Deliverable D2.22 [58], is able to reduce the loads on the hub (and on the tower), the diameter is increased as long as the maximum combined bending moment on the hub does not exceed the one computed for the RWT.

The increase in blade length is done by stretching all the properties to a major extension. No other elements of the wind turbine are touched, i.e. non changes to hub height or rotor cone, etc. The distribution of chord, twist, airfoil thickness is unchanged, but it is now stretched to adapt to a longer blade.

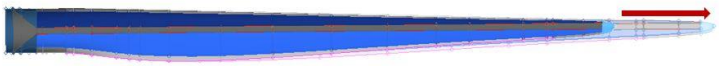

Figure 7.1-1: PoliMI 188m BTC SC+05 IPC, blade length increased

The individual pitch controller is based on the architecture proposed in Ref. [50]. The controller is driven by blade root moments, which are Coleman transformed in a nacelle-fixed frame of reference to yield the rotor tilt and yaw moments. Two independent proportional integral derivative (PID) controllers compute two fixed frame control inputs by trying to drive the tilt and yaw moments to zero. In turn, the fixed frame inputs are back-transformed into the rotating frame using the inverse Coleman transformation, an operation that generates the individual pitch control inputs. Such inputs are superimposed to the ones computed by a collective pitch and torque controller, whose roles are the regulation of the machine around a given set point and the reaction to gusts.

By adjusting the gains of the IPC-PID controllers, one can tune within a certain range the level of individual blade pitch activity, consequently affecting the level of load reduction and of ADC increase.

7.1.3 Anticipated PROS and CONS

The main goal of this solution is to increase the AEP increasing the rotor diameter and, at the same time, keeping frozen the load on the hub and tower, i.e. keeping frozen the other components of the WT. The constraint used in this integrated solution is not to exceed the maximum combined bending moment on the hub based on the assumption that this is a design load. The fatigue loads are computed but not constrained so that in some case may exceed the reference values. The impact of this loads on the structure (and hence on the final real CoE) should further be investigated in the other WPs.

The blade total mass, and its cost, increases, but this seems to have a little impact on the final cost of energy. On the other hand, the longer blade affects heavily the AEP and hence the final cost of energy.

Aerodynamic distribution of twist, chord and thickness remains the same of the RWT, but the longer blade probably changes the local Reynolds number so that this impact on the aerodynamic performance needs to be further investigated.

Possible drawbacks of active load control are the reduction of AEP and its effect on the actuators and their design: constantly pitching the blade increases the actuator duty cycle, and hence requires more expensive and larger actuators, inducing a trade-off with the advantages brought by IPC. The combined adoption of BTC and IPC should mitigate the increment of actuator duty cycle [59].

Nevertheless it is expected a sensible increase of annual energy production and hence a better cost of energy.

7.2 Assessment of the Structural Integrity of the Proposed Design

7.2.1 Design layout and dimensioning

The blade structural layout uses a box-type configuration, with a single cap confined within the two shear webs. The shear webs are parallel and planar, i.e. they do not follow the twist of the airfoils. A third shear web is located at 87% of the local chord, as in the Reference wind turbine. Trailing and leading edge reinforcements are introduced to augment in-plane modal frequencies. Root reinforcement made of unidirectional fiberglass is also here used. To prevent buckling in skin and shear webs panels a sandwich with balsa core is used, while to prevent buckling in the spar caps panels the thickness of the spar caps are designed to be buckling-free.

The main blade parameters and material types used are reported in the following table, while the following figures show the adopted blade structure.

	Starting section (% span)	Ending section (% span)	Material type
Skin	0	100	Tri-axial fiberglass
Spar caps	0.025	98.12	Unidirectional fiberglass
Shear webs	0.025	98.12	Bi-axial fiberglass
Third shear web	0.22	95	Tri-axial fiberglass
Trailing and leading edge reinforcement	0.10	95	Unidirectional fiberglass
Root reinforcement	0	30	Unidirectional fiberglass

Table 7.2-1: PoliMI 188m BTC SC+05 IPC, main blade parameters and material types

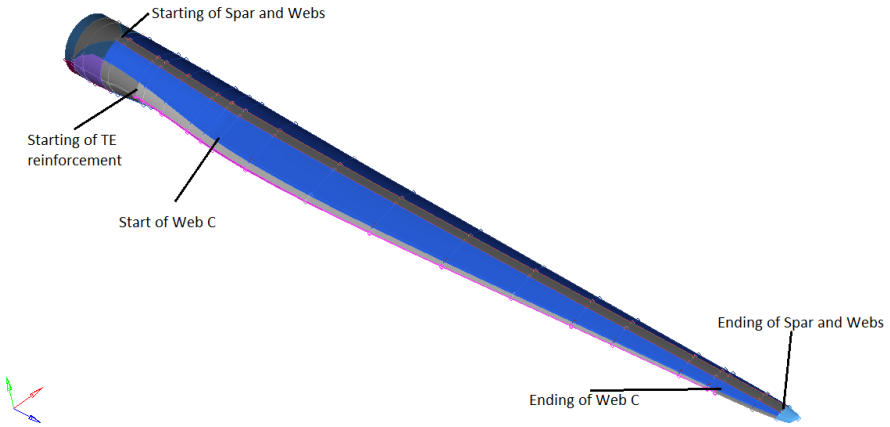

Figure 7.2-1: PoliMI 188m BTC SC+05 IPC, structure of the blade and position of constitutive elements

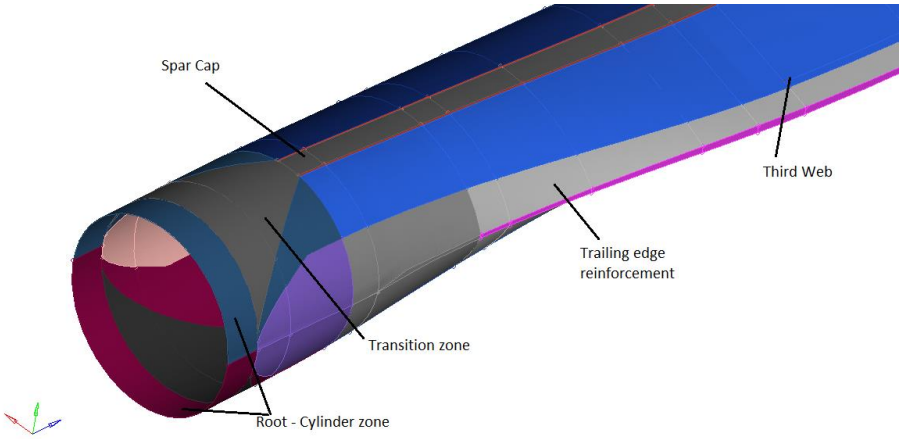

Figure 7.2-2: PoliMI 188m BTC SC+05 IPC, root details

The following table reports the global data of the optimal blade PoliMI 188m BTC SC+05 IPC compared with the reference one.

	RWT	PoliMI 188 m BTC SC+05 + IPC	difference
Rotor Diameter	178.3 m	188 m	+ 5.44 %
Blade Total Mass	42422 kg	49390 kg	+ 16.40 %
Blade 1st modal freq (flap)	0.6123 Hz	0.5494 Hz	-
Blade 2nd modal freq (edge)	0.9124 Hz	0.6062 Hz	-
AEP	45.760 GWh/y	47.701 GWh/y	+ 4.24 %
CoE	75.680 $/kWh	73.623 $/kWh	- 2.72 %

Table 7.2-2: PoliMI 188m BTC SC+05 IPC, Comparison against RWT

The figure below reports the thickness distributions for the core.

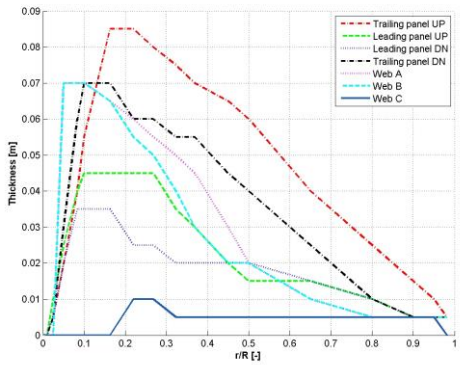

Figure 7.2-3: PoliMI 188m BTC SC+05 IPC, core thickness distributions

The following table reports the mass breakdown computed for each structural components including the Non-Structural Masses (NSM).

Structural Component	Mass [kg]	% of total blade mass
Skin	9553	19.34
Spar Cap	22671	45.9
Web A + B	2352	4.76
Web C	97	0.19
LE & TE Reinforcement	2034	4.12
Root Reinforcement	3315	6.72
Total Structural Mass	40022	81.03
NSM	9368	18.97
Total blade mass	**49390**	100

Table 7.2-3: PoliMI 188m BTC SC+05 IPC, bill of material

The figures below report the thickness distributions along the blade span of the internal sub-components and the mass, flapwise and edgewise stiffness.

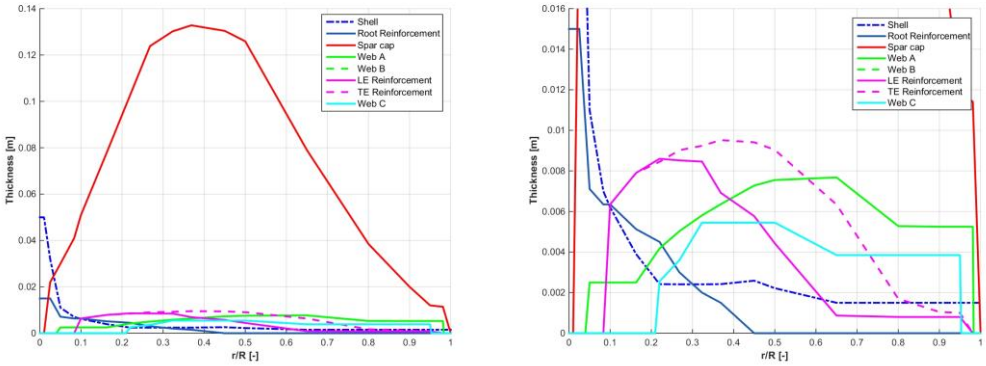

Figure 7.2-4: PoliMI 188m BTC SC+05 IPC, structural thickness distributions

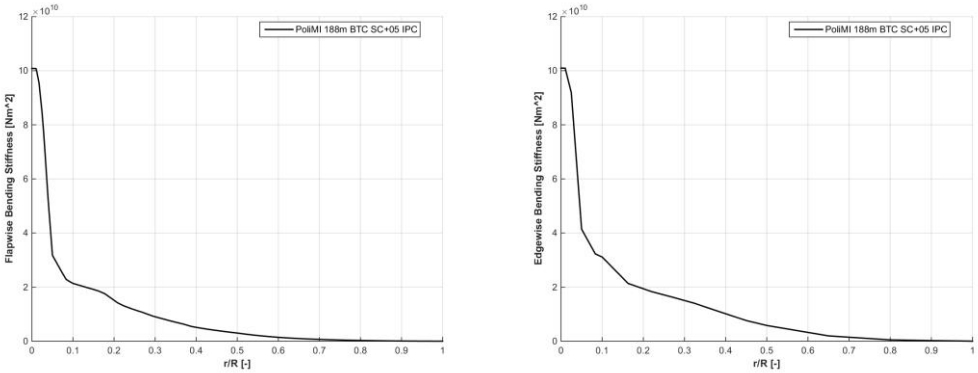

Figure 7.2-5: PoliMI 188m BTC SC+05 IPC, flapwise (left) and edgewise (right) stiffness distributions

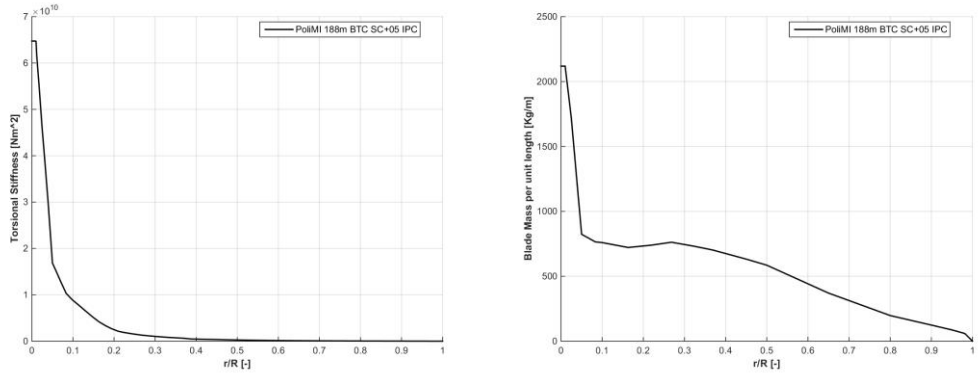

Figure 7.2-6: PoliMI 188m BTC SC+05 IPC, torsional stiffness (left) and blade mass (right) distributions

The next figures show the deflection of the blade in the out of plane direction in correspondence of the first mode of vibration (at left) and the corresponding torsion associated to the blade (at right) mainly due to the bend-twist coupling.

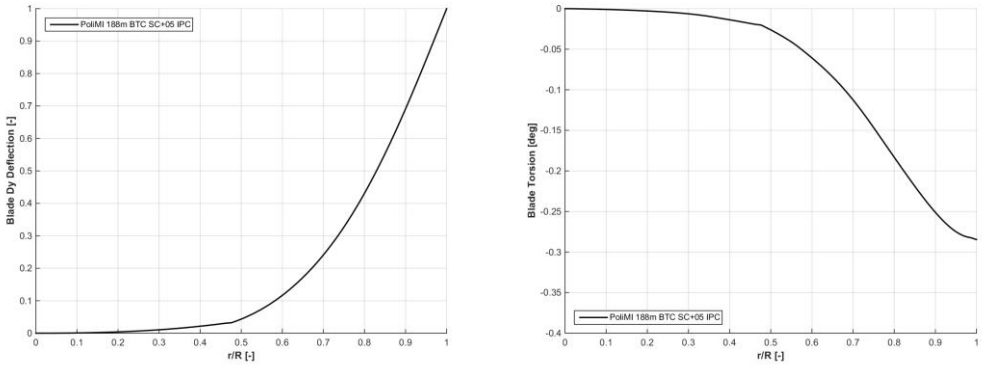

Figure 7.2-7: PoliMI 188m BTC SC+05 IPC, first flapwise mode: flapwise (left) and torsion (right) deflections

7.2.2 Load cases considered

The blade is designed according to IEC 61400-1 Ed.3. The load cases selected for the design are the same defined in section 6.2.2.

A complete description of the blade characteristics may be found in the attached file "PoliMI_10MW_BTC_SC05_188.0m_IPC.xlsx".

7.2.3 Structural integrity verification

The proposed blade satisfies all the design constraints, as can be seen from the following figures, which report the constraint margin for stress, strain and fatigue analysis in all the structural components of the blade as described in the previous sections.
A constraint value is considered active when its value reaches 0 (within the optimization tolerance). If the value is positive the constraint is violated, if negative it is satisfied. As one can see, only the fatigue constraint is active in the first 3 figures, which are relatives to skin, spar cap and webs.

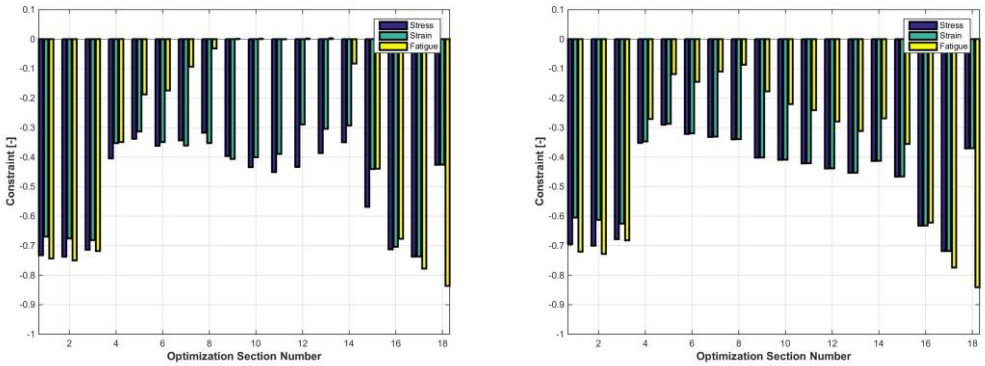

Figure 7.2-8: PoliMI 188m BTC SC+05 IPC, skin (left) and spar cap (right) constraints

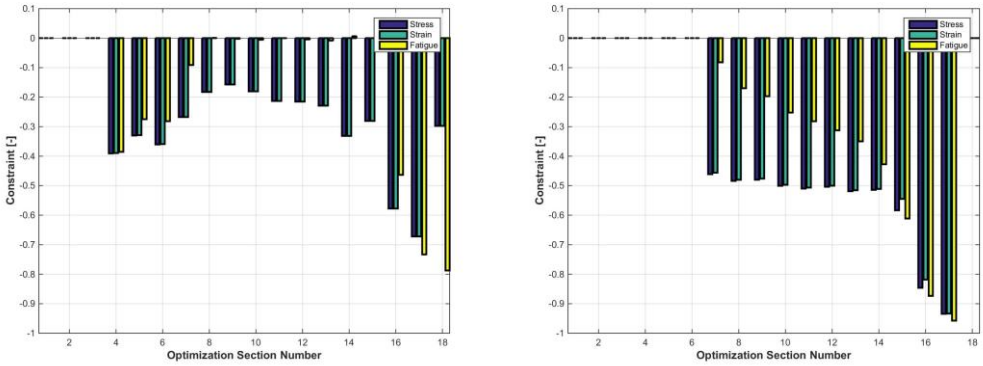

Figure 7.2-9: PoliMI 188m BTC SC+05 IPC, web (left) and TE reinforcement (right) constraints

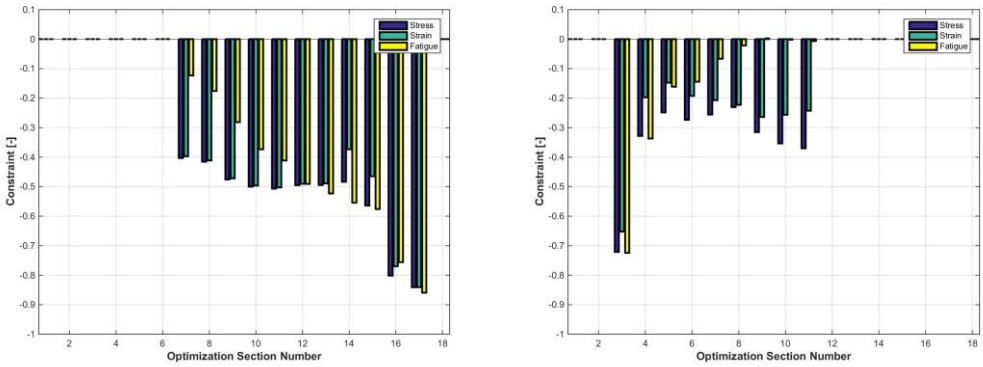

Figure 7.2-10: PoliMI 188m BTC SC+05 IPC, LE reinforcement (left) and root reinforcement (right) constraints

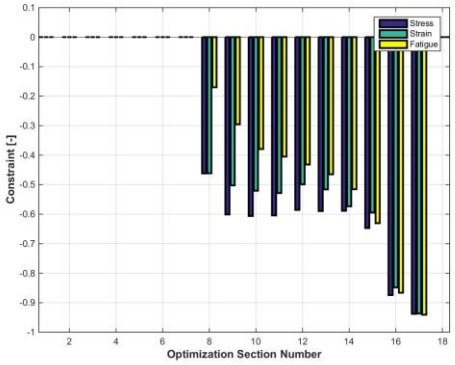

Figure 7.2-11: PoliMI 188m BTC SC+05 IPC, third web constraints

The following table shows the ultimate loads on the hub and tower compared with the ones computed (with the same conditions) for the RWT. In this analysis the hub combined bending moment is constrained to be equal to the reference one (- 0.55%), but, as one can see, the loads on the tower are slightly higher (+ 1.62% for the tower bottom combined bending moment) than the reference values.

	RWT	PoliMI 188 m BTC SC+05 + IPC	difference
Hub Nodding Moment	57097 kNm	56957 kNm	- 0.25 %
Hub Yaw Moment	53046 kNm	52421 kNm	- 1.18 %
Hub Combined Moment	58271 kNm	57960 kNm	- 0.55 %
Hub Axial Force	3560 kN	3324 kN	- 6.63 %
Tower Bottom Fore-Aft Moment	491819 kNm	503813 kNm	+ 2.44 %
Tower Bottom Combined Moment	495794 kNm	503829 kNm	+ 1.62 %
Tower Top Fore-Aft Bending Moment	59244 kNm	54534 kNm	- 7.95 %
Tower Top Torsional Moment	58688 kNm	58993 kNm	+ 0.52 %

Table 7.2-4: PoliMI 188m BTC SC+05 IPC, comparison of ultimate loads against RWT

Fatigue loads:

The next table shows the cumulative damage equivalent loads computed considering only DLC12 cases (power production in turbulent wind). A Weibull distribution has been used, with a shape factor of 2 and a mean wind speed of 10m/s. Damage Equivalent Load (DEL) are weighted with Weibull. Following parameters are chosen for the fatigue analysis, for both the blades:

- Number of bin: 100
- Number of years: 25
- Frequency: 0.012684 Hz
- m = 3

It can be seen that the optimal blade with combined BTC and IPC with this longer blade increases the fatigue loads of about 15% on the hub. Since tower and hub have not been re-designed in this deliverable, the real effects on the CoE of this optimal blade needs to be further investigated.

	RWT	PoliMI 188 m BTC SC+05 + IPC	difference
DEL Hub Nodding Moment	27950 kNm	32149 kNm	+ 15 %
DEL Hub Yaw Moment	26192 kNm	29906 kNm	+ 14.1 %
DEL Tower Bottom Side-Side Moment	59828 kNm	57948 kNm	- 3.14 %
DEL Tower Bottom Fore-Aft Moment	136805 kNm	149026 kNm	+ 8.93 %

Table 7.2-5: PoliMI 188m BTC SC+05 IPC, Comparison of fatigue DEL against RWT

Buckling analysis:

The first buckling eigenvalues appears at suction side between 3.0m and 5.0m from the blade root, but the critical load is higher than actual load on the blade since the minimum buckling load factor computed is 1.0698 in leading edge panels as showed in the next figure. The safety factor on material is already been considered.

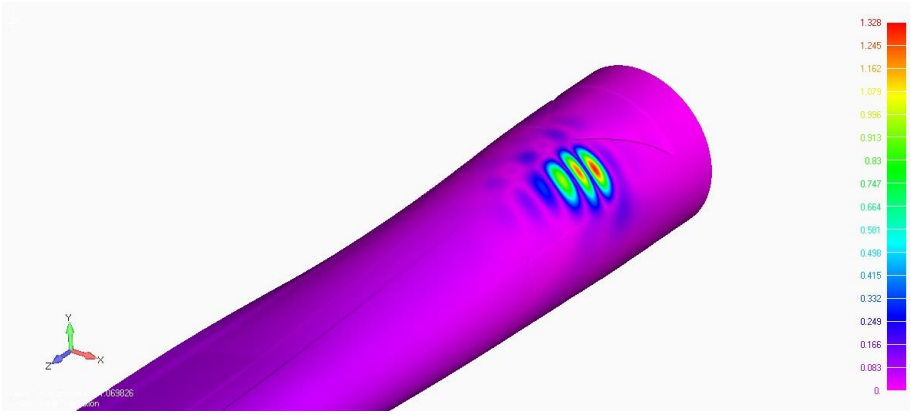

Figure 7.2-12: PoliMI 188m BTC SC+05 IPC, FE buckling visualization

7.3 LCOE Impact of the Proposed Design

7.3.1 Effect on Annual Energy Production

The following figures show the power curve computed in turbulent condition for both the *PoliMI 188m BTC SC+05 IPC* and the RWT. In region II the power of the new re-designed blade is, as expected, significantly higher. The final AEP is in fact + 4.24 % higher. The figure on the right reports the standard deviation (STD) of the power curve compared against the STD of the RWT. This curve shows that, mainly in region III, the STD of the PoliMI blade is much lower.

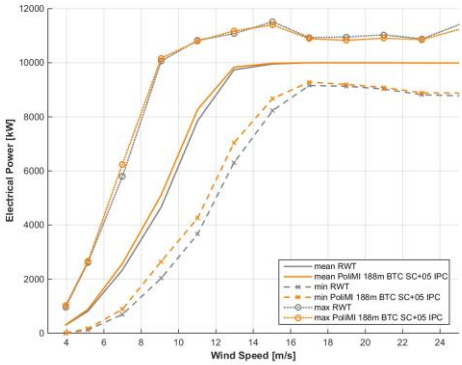

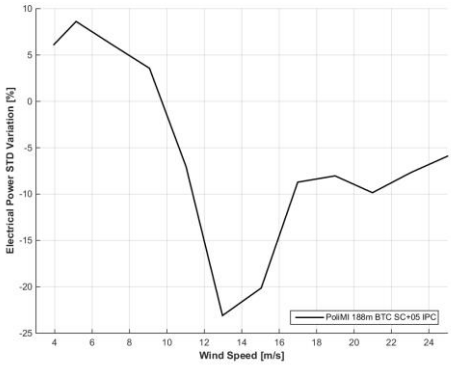

Figure 7.3-1: PoliMI 188m BTC SC+05 IPC, turbulent power curve (left) and power STD variation (right), comparison against RWT

7.3.2 Effect on CAPEX

The effect of the increase in mass and in blade length is clear in the increase in Turbine Cost.

	RWT	PoliMI 188 m BTC SC+05 + IPC	difference
Turbine Cost [€/kW]	1376	1435	+ 4.28 %
BoP Cost [€/kW]	1695	1695	-
Capital Investment [€/kW]	3071	3130	+ 1.92 %
CAPEX (Turbine) [€/MWh]	22.19	22.19	-
CAPEX (BoP) [€/MWh]	27.33	26.21	- 4.09 %

Table 7.3-1: PoliMI 188m BTC SC+05 IPC, contribution of CAPEX

BoP (Balance of Plant) does not change, because it is affected only by Nominal Power of the WT, which is the same.
The increase in in turbine cost is due to the increase in blade cost, but this is absorbed by the increase in AEP, resulting in the same CAPEX contribution as per regards the turbine costs

7.3.3 Effect on OPEX

	RWT	PoliMI 188 m BTC SC+05 + IPC	difference
DO&M [M€/y]	1.197	1.203	+ 0.48 %
AEP [GWh/y]	45.760	47.701	+ 4.24 %
OPEX [€/MWh]	26.17	25.22	- 3.63 %

Table 7.3-2: PoliMI 188m BTC SC+05 IPC, contribution of OPEX

The higher AEP reflects in higher Operation and Maintenance costs (in the table is reported the DO&M, annual Discounted Operation and Maintenance cost), but the OPEX, which is the ratio between the two is significantly lower.

The details of the CoE may be found in the attached file "*Costs Models v1.02 - PoliMI_BTC_SC05_188.0m_IPC.xls*".

7.4 Conclusions and Recommendations

In this section PoliMI has presented an integrated structural solution based on the so called Bend-Twist Coupling (BTC), Individual Pitch Controller (IPC) plus a blade stretch. The BTC is a passive load mitigation solution obtained by exploiting the anisotropic mechanical properties of composite materials. BTC implies that, when the blade bends because of increased loads, the ensuing change of twist will affect the aerodynamic loading through a change in angle of attack. IPC is an active load mitigation solution which exploits a power source to move the whole blade, or a part of it, so as to reduce loads due to turbulence, gusts and asymmetry in the inflow. It is here explored the possibility offered by the combination of these two technologies. The load reduction obtained by this solution has been used here to increase the rotor diameter without exceeding the hub loads with respect to the reference ones.

The structural solution is computed throughout a blade design procedure based on a novel comprehensive multi-level constrained optimization approach. The design process alternates between a multibody beam model augmented with a 2D FEM cross sectional sub-models and a fine scale 3D FEM detailed model of the blade. The former enables the numerous transient aero-servo-elastic analyses required to compute loads and deflections throughout the lifetime of the machine, while the latter makes it possible to conduct detailed local verifications of the design.

The use of a constrained optimization-based approach to design is crucial and allows comparing different solutions that satisfy the same design requirements, and hence permitting to choose the optimal solution. The control set-points have been changed in order to improve the annual energy production.

The possibility offered by the synergetic adoption of BTC and IPC of lowering the loads allowed to increase as much as possible the rotor diameter, operation that concerns a worsening of loads, but that has the main goal of increase the energy production.
The optimal blade presented here is significantly longer, +5.44%, and heavier, +16.40%, with respect to the RWT, but produces more energy, +4.24%, and, at the end, has a lower cost of energy, -2.72%. The larger rotor diameter permits also to reduce the oscillations in power production, permitting to improve the quality of power production.
Ultimate loads on hub are quite close to that of the RWT, tower top moment is 8 % lower. For tower bottom loads the situation is opposite, the RWT is subjected to lower loads, even if the difference is small, at about 2%.
On the other side, fatigue loads increase, both on the hub and on the tower. The solution proposed here is constrained to keep the maximum loads on the hub constant, not the fatigue loads, based on the assumption that these ultimate loads are design-driven. Since these components have not been re-designed within this task, the actual final effect on the CoE of this optimal blade has to be further investigated. In order to try to mitigate also these fatigue loads one could use a different IPC setting (changing the IPC-PID gains).
Alternatively a lower rotor diameter can be selected. This parametric analysis (changing the rotor diameter with BTC+IPC) has been investigated and summarize in the following table and figures.

	RWT	PoliMI BTC SC+05 + IPC	PoliMI 182m BTC SC+05 + IPC	PoliMI 185m BTC SC+05 + IPC	PoliMI 188m BTC SC+05 + IPC
Rotor Diameter	178.3 m	178.3 m	182 m	185 m	188 m
Blade Total	42422 kg	- 4.80 %	+ 2.80 %	+ 9.40 %	+ 16.40 %

	RWT	PoliMI BTC SC+05 + IPC	PoliMI 182m BTC SC+05 + IPC	PoliMI 185m BTC SC+05 + IPC	PoliMI 188m BTC SC+05 + IPC
Mass					
AEP	45.760 GWh/y	+ 0.69 %	+ 2.12 %	+ 3.01 %	+ 4.24 %
CoE	75.680 €/MWh	- 0.92 %	- 1.71 %	- 2.11 %	- 2.72 %
Hub Combined Moment	58271 kNm	- 12.53 %	- 9.80 %	- 4.74 %	- 0.55 %
Tower Bottom Combined Moment	495794 kNm	- 6.35 %	- 3.21 %	- 0.03 %	+ 1.62 %
DEL Hub Nodding Moment	27950 kNm	- 5.55 %	+ 2.05 %	+ 8.34 %	+ 15 %
DEL Hub Yaw Moment	26192 kNm	- 4.93 %	+ 2.33 %	+ 7.35 %	+ 14.1 %

Table 7.4-1: comparison of increasing rotor diameter solution against RWT

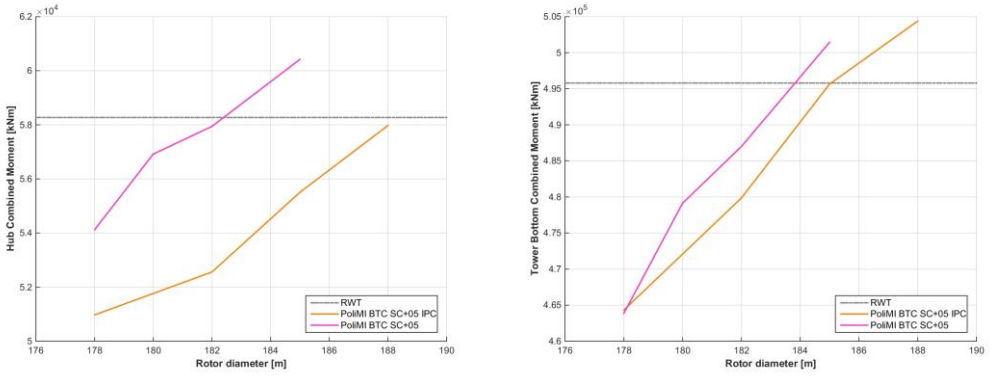

Figure 7.4-1: Comparison of hub (left) and tower bottom (right) combined moments wrt rotor diameter

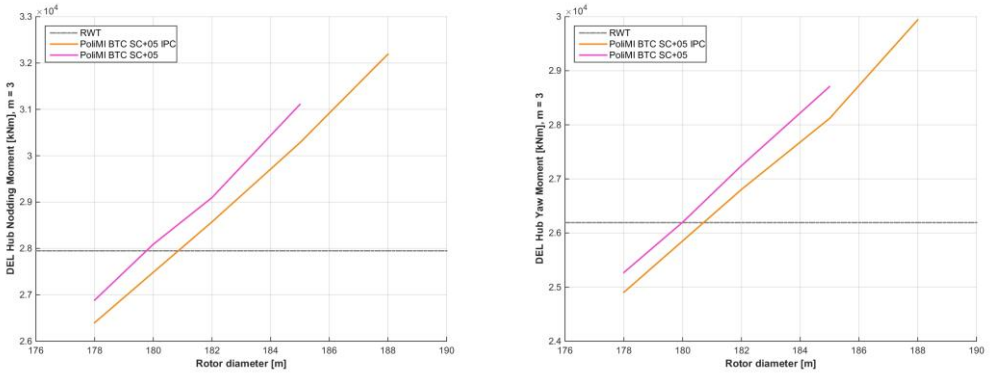

Figure 7.4-2: Comparison of hub nodding (left) and yawing (right) DEL moments wrt rotor diameter

Finally, the next table summarizes PoliMI's (integrated) solutions compared with the RWT.

	RWT	PoliMI BTC SC+05	PoliMI 182m BTC SC+05	PoliMI BTC SC+05 + IPC	PoliMI 188m BTC SC+05 + IPC
Rotor Diameter	178.3 m	178.3 m	182 m	178.3 m	188 m
Blade Total Mass	42422 kg	- 3.65 %	+ 5.02 %	- 4.80 %	+ 16.40 %
AEP	45.760 GWh/y	+ 0.87 %	+ 2.19 %	+ 0.69 %	+ 4.24 %
CoE	75.680 €/MWh	- 1.01 %	- 1.68 %	- 0.92 %	- 2.72 %
Hub Combined Moment	58271 kNm	- 7.13 %	- 0.49 %	- 12.53 %	- 0.55 %
Tower Bottom Combined Moment	495794 kNm	- 6.44 %	- 1.77 %	- 6.35 %	+ 1.62 %
DEL Hub Nodding Moment	27950 kNm	- 3.82 %	+ 4.10 %	- 5.55 %	+ 15 %
DEL Hub Yaw Moment	26192 kNm	- 3.52 %	+ 4.01 %	- 4.93 %	+ 14.1 %

Table 7.4-2: comparison of different solutions against RWT

Attached files

[1] PoliMI_10MW_BTC_SC05_188.0m_IPC.xlsx
[2] Costs Models v1.02 - PoliMI_BTC_SC05_188.0m_IPC.xls

CHAPTER 8 SUPERCONDUCTING GENERATOR

8.1 Selection of superconducting wire technology

The SuperConducting Direct Drive (SCDD) generators investigated in the INNWIND.EU project are based on commercially available superconducting wires containing

1) **NbTi** Niobium-Titanium is the work horse of the Magneto Magnetic Resonant (MRI) industry and has also used for accelerator magnets for decades. It is made by putting NbTi powder in copper tubes that are extruded to 10 km length (Powder-In-Tube method).
The critical temperature is T_C = 9.8 K (-263 ^oC) and the price is about 0.4 €/m [60]

2) **MgB_2** Magnesium-di-Boride wires are still being developed as MgB_2 was discovered to be superconducting in 2001. It is with the Powder-In-Tube method as NbTi. The T_C = 39 (- 234 ^oC) K and the price is about 1-4 €/m [60]

3) **RBCO** High temperature superconducting Rare Earth–Barium–Copper-Oxide ($RBa_2Cu_3O_{6+x}$) in the form of coated conductors. This compound was discovered in 1986 and is still being developed, because coated conductors are made by depositing a micro meter thick thin-film onto a metal substrate being several kilometers long. The T_C = 93 K (-180 ^oC) and the price is about 20-30 €/m due to the advanced processing method [60].

The first option NbTi is well established and it is used as a reference scenario as described by GE-global Research [61]. The MgB_2 option is investigated by performing generator designs in Task 3.11 and also by demonstrating a coil in Task 3.13. The last option is being investigated by the industrial partner Siemens Wind Power by making an industrial demonstration in Task 3.12.

Both the MgB_2 demonstration coil and the industrial demonstrations are delayed in the INNWIND.EU project due to technical challenges and the final findings can therefore not be included the current comparison between MgB_2 and RBCO. In general terms it can be said that the low operation temperature of NbTi is considered to be a serious challenge for the wind turbine generator application. This is improving for MgB_2 and especially for RBCO, but the high price for the RBCO tape is indicating that MgB_2 is most likely the fastest technology to be implemented. It should however be said that RBCO is considered to become the cheapest technology in the long run, because the tapes are produced of little and in-expensive materials, but using a very expensive production methods [60]. These methods are expected to be improved and to become cheaper as production volumes of the tapes are ramped up.

8.2 Nacelle layout

Based on these assumptions we will here present the optimization of a 10 MW MgB2 SCDD generator tailored to the INNWIND.EU 10 MW reference turbine [62]. Figure 8.1 is illustrating the INNWIND.EU nacelle based on the King-pin concept done by DNV-GL [63]. It is based in having two main bearings sitting on each side of hub holding the blades. Is has been decided to place the SCDD in front of the rotor plane, because that allows more freedom for designing the cryogenic cooling system in the middle of the ring generator and

because superconducting generators have the potential to become more compact other direct drive options.

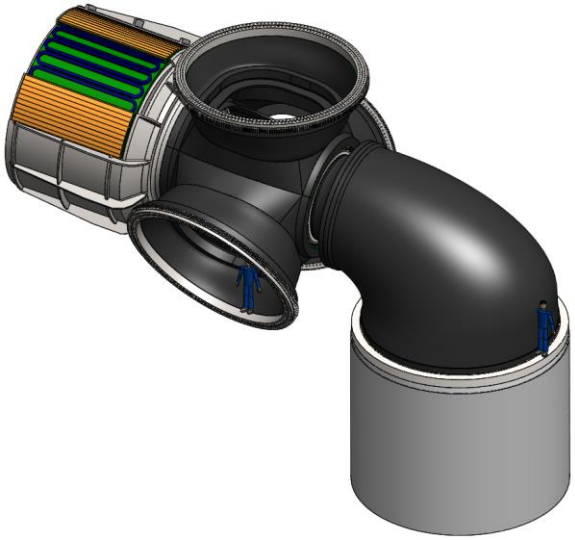

Figure 8-1. Illustration of the INNWIND.EU 10 MW nacelle concept. It is based on the king-pin configuration with a main bearing on each side of the hub holding the rotor blades. The direct drive generator is placed in front of the rotor in order to allow space of the cryogenic cooling system [4]. The MgB_2 coils are shown as blue and are shown as an outer rotor configuration.

8.3 MgB_2 Generator optimization

A central question of task 3.11 has been to find out the best way to use the MgB_2 wire in a wind turbine generator in terms of which active materials to use for creating and shaping the magnetic flux distribution inside the generator. The main parameter of a radial flux generator is the shear force density F_d given by the product of peak magnetic flux density of the rotor B_r and the current loading of the armature A_S

$$F_d = \frac{1}{2} B_r A_S \cos\gamma \qquad (8\text{-}1)$$

where γ is the angle between the two distributions [64].

The initial assumption of task 3.11 was that one can increasing the peak magnetic flux density in eq (8-1) utilizing superconducting MgB_2 coil, whereby more compact generators can be obtained [65]. This concept is following the same design philosophy that was used for the NbTi design performed by GE Global Research. Figure 8-2 is showing the resulting coil design and the magnetic flux distribution inside the generator. These coils are included in the illustration of the nacelle in figure 8-1 and they were used to specify the dimensions of the MgB_2 coil demonstration of Task 3.13, which has the same cross section but the length of the straight section is only 0.5 m [65]. From the initial analysis it was clear that a wire amount in the order of 474 km would be needed and that with a wire cost of the order 4 €/m that would amount to 1876 k€. This was compared to a total drive train cost threshold value determined as 20% of the CAPEX of an offshore turbine at 1.5 M€/MW ~ 0.3 M€/MW. Thus the wire cost was about 63 % of the total available CAPEX for the drive train and thereby considered very high [65]. The main reason why the NbTi

philosophy is not applicable to MgB_2 is that the critical current density of the superconducting wire is about 10 times smaller. An initial estimate of the demand for MgB2 wires were done by assuming the construction of a 10 GW SCDD offshore capacity by 2030, which would amount to 474000 km of wire. With a worldwide annual wire production in the order of 5000 km/year then a considerable production upscaling will be needed and a price reduction is therefore also expected. Discussions with the manufactory Columbus Superconductors revealed that a target price in the order of 1 €/m could be expected for the large scale production. Using this wires price then cost of the 474 km of MgB2 wire would correspond to 16 % of the CAPEX threshold for the drive train [65]. This is still high and a more conventional design philosophy was implemented to find a cheaper machine.

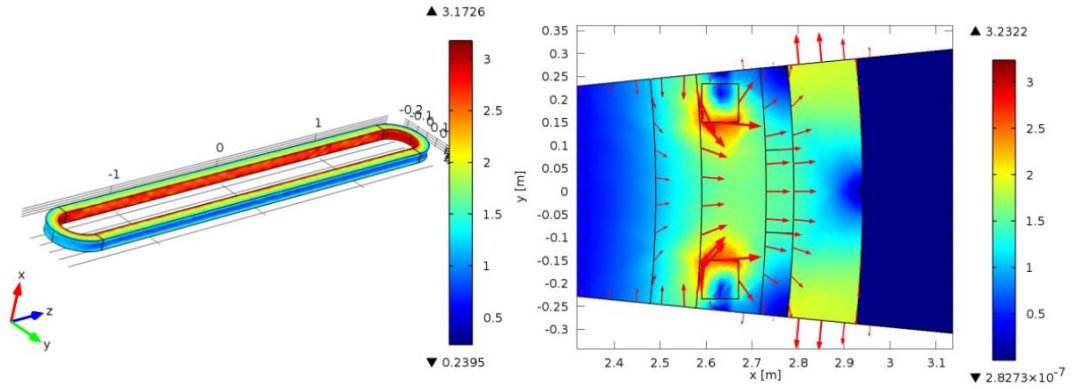

Figure 8-2. Left) Initial design of MgB2 coil for a 10 MW SCDD. Right) Magnetic flux distribution inside the generator where an airgap flux density of 1.5 Tesla is obtained [65].

In order to find the best utilization of the MgB2 wire in a wind turbine generator an optimization algorithm was implemented with the finite element software COMSOL [66]. The optimization strategy is two-fold. Primarily to change the dimensions of the generator parts as well as the number of pole-pairs in order to find the cheapest layout by assuming some general costs of the active materials as outlines in table 8-1. Secondly to replace different parts of the generator by different active materials in order to determine the cheapest generator topology for a wind turbine. The main question is how much iron that should be included in the generator in order to decrease the magnetic flux path and thereby bring down the usage of the expensive superconducting wire, but on the other hand increase the weight of the generator.

Material	Price [€/kg]
Cu	15
FeSi laminates	3
Glass fibre (G10)	15
MgB_2 tape	4 (→ 1) €/m

Table 8-1. Price of active material of superconducting direct drive generators [66].

Figure 8-3 is showing the 2D cross section of the generator pole layout and figure 8-4 is showing a series of generator topologies with an increasing amount of iron being included as back of the rotor, the rotor pole piece, the back of the armature and in the teeth of the armature. Figure 8-5 is illustrating the consequence on the cost of the active materials as more is introduced from topology 1 towards 9 by assuming a MgB_2 wires price of 4 €/m as

well as 1 €/m reflection large scale production volumes. A line indicating the cost of active materials of a 10 MW Permanent Magnet Direct Drive (PMDD) generator is included and it is seen that the MgB_2 generator will match the PMDD for a wire cost of 1 €/m [66].

The cheapest generator has the T9 topology and the usage of MgB_2 at 1 €/m is about 100 km resulting in a cost of 100 k€ for the 10 MW machine. This is corresponding to 3 % of the drive train CAPEX threshold and seems reasonable.

Taking the concept of putting as much iron into the generator as possible to the limit then one will obtain a quite conventional design, where the high current density of the superconducting wire is only used to magnetize the iron circuit. Figure 8-6 is showing two such generators with either non-magnetic-teeth (NMT) or iron teeth (IT) in the armature winding. The physical airgap between the rotor pole piece and the armature is narrowed down to 6 mm resulting in a huge reduction of superconducting usage to 15.3 km, which would constitute 61 k€ (assuming 4 €/m of MgB_2 wire price) or 2.0 % of the drive train CAPEX threshold. If a wire cost of 1 €/m is assumed then a CAPEX fraction below 1% might be obtained [67].

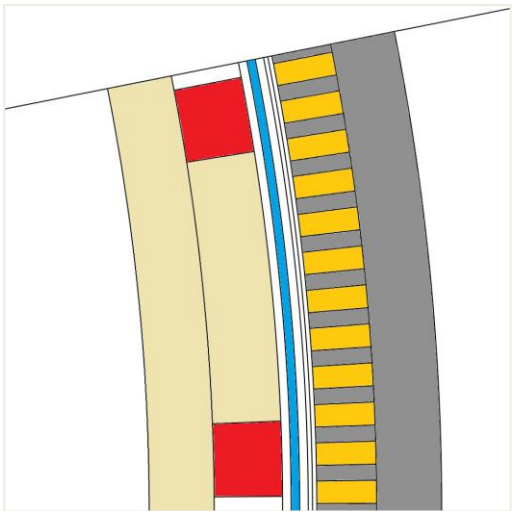

Figure 8-3. Generator pole topology for optimization of the cost. Components from left to right: Rotor back and pole piece (beige), Superconducting coils (red), cryostat wall (blue), Copper armature windings (yellow) and armature iron teeth and back iron (Gray).

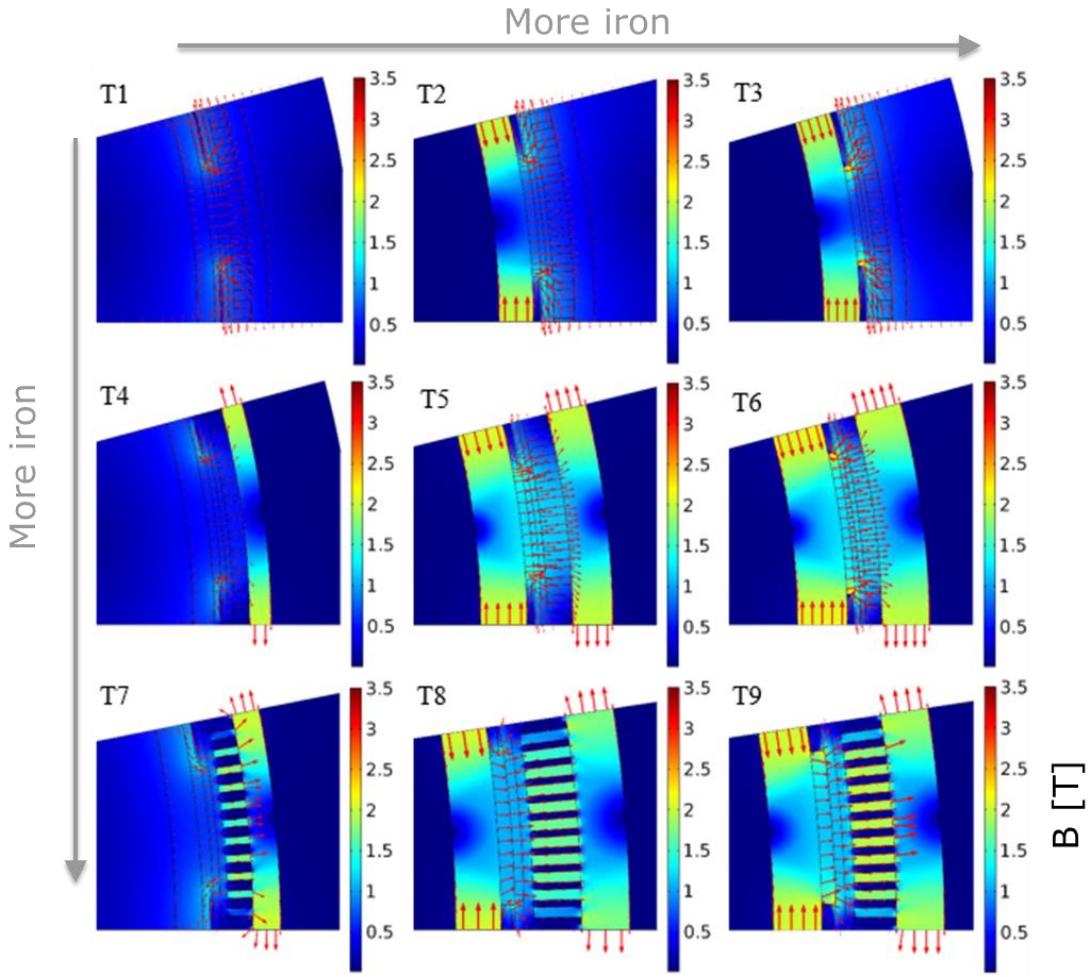

Figure 8-4. Generator topologies with an increasing amount of iron in the machine to reduce the magnetic flux path and thereby bring down the amount of superconducting wire used [7].

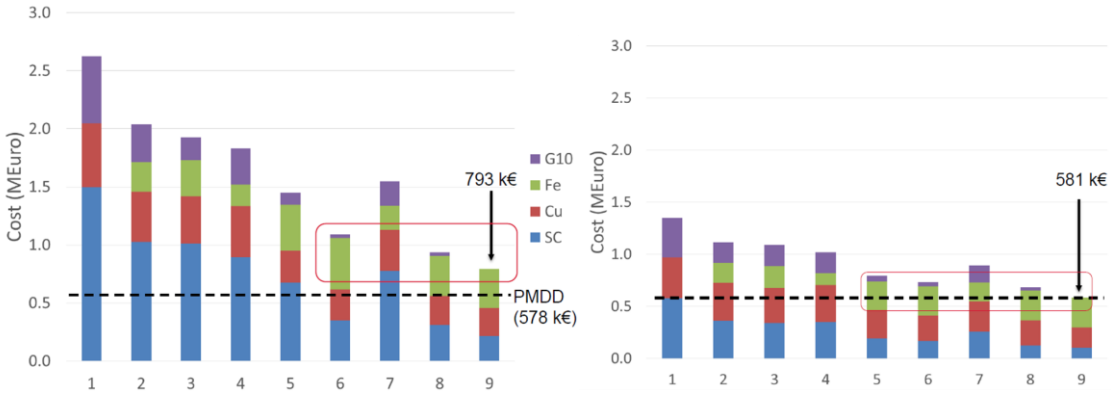

Figure 8-5. Cost of active materials for the generator topologies of figure 8-4 by assuming an MgB_2 wire price of 4 €/m (left) and 1 €/m (right) reflecting large scale production volume. The dashed line is indicating the expected cost of the active materials of a permanent magnet direct drive (PMDD) generator. The initial design of figure 8-2 is equivalent to the T4 topology [66].

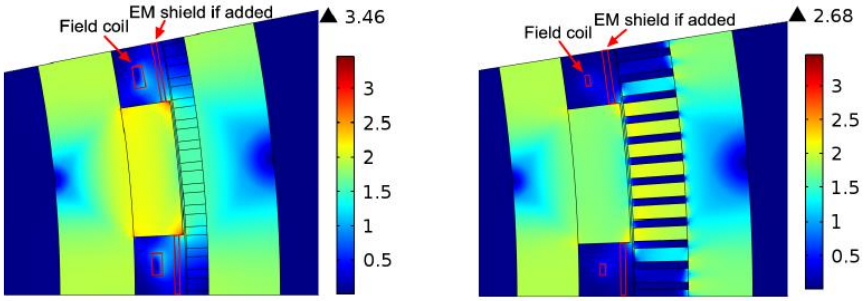

(a) NMT design (b) IT design

Figure 8-6. Generator topologies with as much iron as possible by reducing the physical airgap between the rotor and armature if based on Non Magnetic Teeth (NMT) [Left] and with Iron Teeth (IT) in the armature [right].

	IT design	NMT design
Nominal power	10 MW	
Nominal speed	9.65 rpm	
Rated voltage	3300 V	
Specific electrical loading	75 kA	
Air gap diameter	6 m	
Mechanical air gap	6 mm	
Distance from field coil to air gap	50 mm	
Cryogenic temperature	20 K	
Price of MgB_2 wire	4 €/m	
Generator axial length	2.56 m	2.63 m
Total MgB_2 wire length	15.23 km	77.54 km
Active material cost	687.24 k€	982.13 k€
Active material mass	148.95 ton	164.24 ton
Annual energy production	44.7379 GWh	43.4399 GWh
Capacity factor	0.511	0.496
Pole pair number	20	16
Field current density in a MgB_2 wire	179 A/mm^2	118 A/mm^2
Field coil side height	10 mm	24 mm
Field coil side width	20 mm	52 mm
Number of turns per coil	60	371
Armature slot height	102 mm	50 mm
Armature yoke height	122 mm	164 mm
Field pole core height	100 mm	114 mm
Field pole width	260 mm	306 mm
Field core back height	118 mm	172 mm
Ratio of armature tooth to slot pitch	0.65	0.41

Table 8-2. MgB_2 generator properties after increasing the iron fraction as illustrated on figure 8-6. It should be noted that the needed amount of MgB_2 is reduced to only 15 km when using Iron Teeth (IT) compared to the Non-Magnetic-Teeth (NMT) [67].

The cost and mass of the active materials of the IT and NMT generators of table 8-2 are shown in figure 8-7 and figure 8-8. The efficiency of the generators are discussed when they are combined with the efficiency of the power electronics.

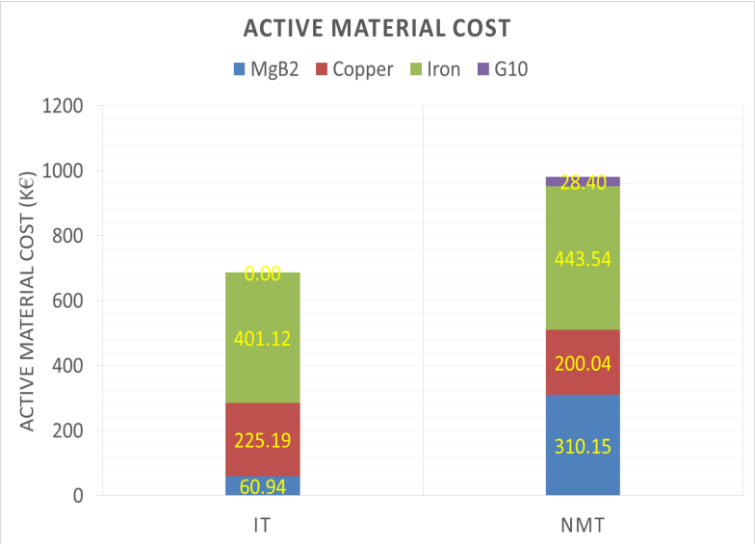

Figure 8-7. Cost of the active mass of generator with Iron Teeth (IT) in the armature [right] and Non Magnetic Teeth (NMT) [Left].

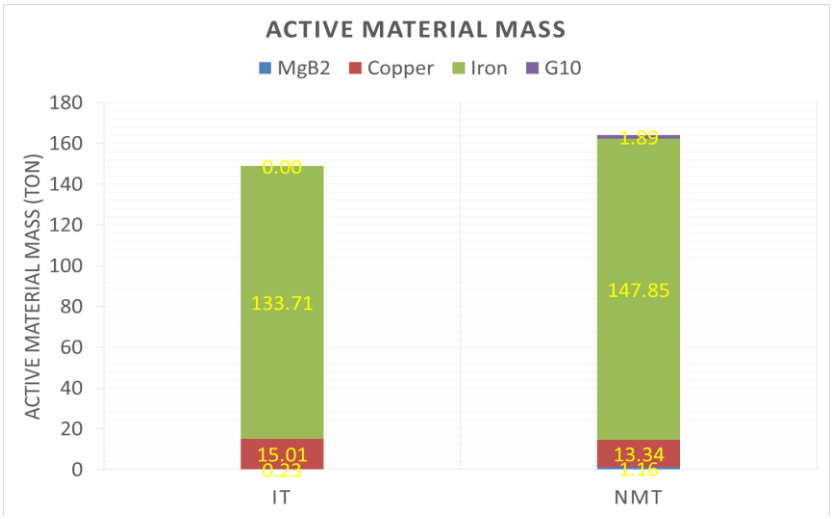

Figure 8-8. Active mass of generator with Iron Teeth (IT) in the armature [right] and Non Magnetic Teeth (NMT) [Left].

8.4 Power electronics tailored to Superconducting direct drive generators

The superconducting direct drive generators have a relative low pole pair number compared to permanent magnet direct drive wind generator and thereby also a lower operation frequency in the order of a few Hz. This is pushing the normal frequency specification of power electronics for full wind turbine converter and it has therefore been

investigated if state of the art as well as a novel power electronics configuration will be able to handle the low frequency in the INNWIND.EU deliverable D3.31 [68]. Figure 8-7 is illustrating the topology tailored for the superconducting generators and figure 8-8 is showing the efficiency at partial load.

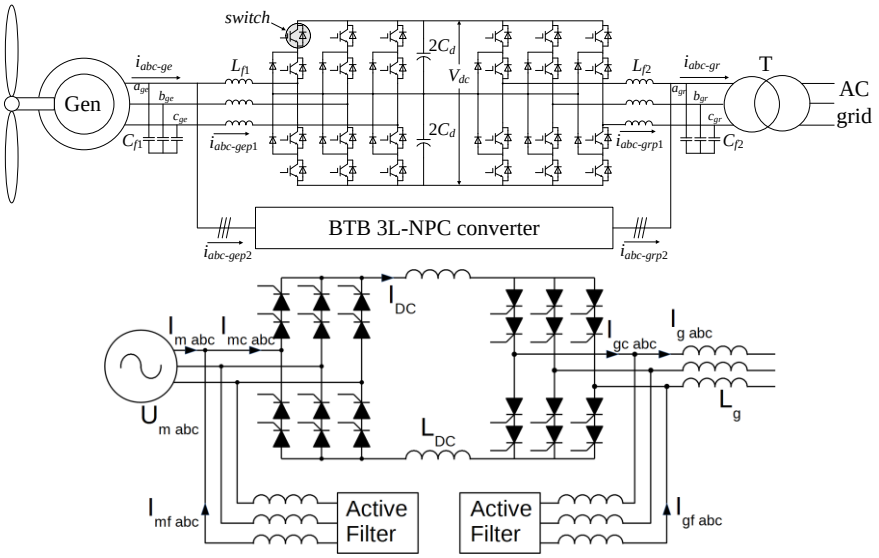

Figure 8-7. Power electronics tailored to superconducting generators. Voltage Source Inverter (VSI): 2 parallel back to back 3 level neutral point clamped converters is the most widely used configuration of the wind industry (top) whereas the Current Source Inverter (CSI) as more simple rectifier combined with active filters have also been investigated (bottom).

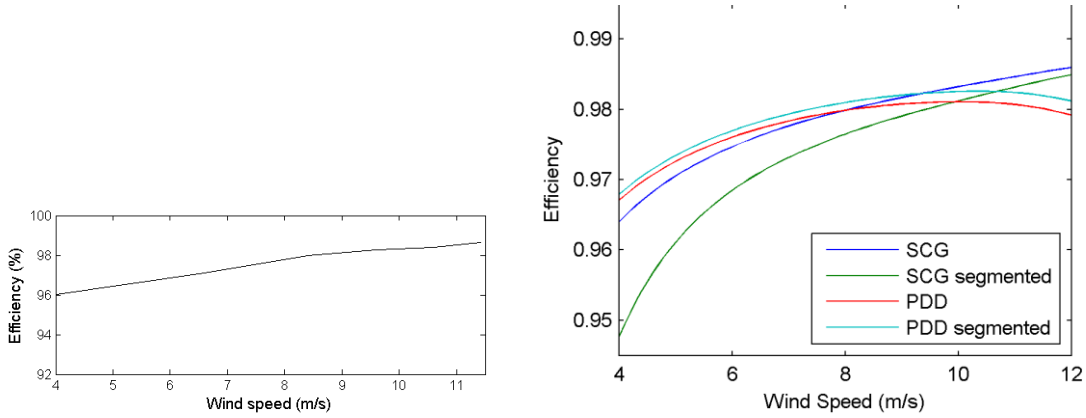

Figure 8-8. Efficiency of Voltage Source Inverter (VSI) and Current Source Inverter (CSI) for 10 MW SCDD [68].

Power Converter	Gen.	Power (MW)	Seg.	Gen. type	Total cost (k€)	Size (m^3)	Weight (kg)	AEP (MWh)	CoE (€/MWh)
VSC	SCG	10	non-seg.	T8	704	30.4	10710	47588	0.71
			Seg.	T8	796	22.9	14752	47423	0.73
		20	non-seg.	T10	1298	34.3	12822	95171	0.63
			Seg.	T10	1408	60.8	21420	95018	0.67
	PDDG	10	non-seg.		859	26,69	8550	47020	0.731
		20	Seg.		1809	59.37	17100	93799	0.771

CSI	SCG	10	non-seg.	T5,6	499	23.8	7040	47,668	0.419
				T8,9	452	20.3	6040	47,635	0.380
			Seg.	T5,6	376	20.7	5820	47,611	0.316
				T8,9	384	20.7	5590	47,464	0.323
		20	non-seg.	T10	760	30.7	9880	95,580	0.318
				T11	824	34.7	11100	95,607	0.345
			Seg.	T10	711	30.0	9680	95,335	0.298
				T11	777	33.0	10800	95,370	0.326
	PDDG	10	non-seg.		402	17.8	7590	47,436	0.339
			Seg.		376	19.9	7780	47,524	0.317
		20	non-seg.		619	26.7	11100	95,388	0.259
			Seg.		601	26.7	11100	95,458	0.252

Table 8-3. Summary of the properties of the power electronics tailored to the SCDD and PDD generators [68]

8.5 Cost of Energy of MgB_2 SCDD combined with power electronics

After the pure cost optimization as shown in figure 8-5 a more advanced optimization taking the cost of energy into account was performed. This was done by assuming a Weibull wind distribution corresponding to a class Ia and by using the mechanical power curve of the 10 MW INNWIND.EU reference turbine as described in deliverable D1.21. The Annual Energy Production (AEP) is calculated by integrating the Weibull distribution over the mechanical power curve subtracted the losses of the generator and power electronics as shown on figure 8-8. The Cost of energy is then determined as

$$CoE = \frac{CAPEX+OPEX}{AEP} \quad (8\text{-}2)$$

Where CAPEX are the capital expenditures and OPEX is the operation and maintenance expenditures. In this study the CAPAX is describes as the sum of the turbine cost minus the generator but added the cost of the foundation (balance of plant). The OPEX is excluded from the study, because no information for 10 MW turbines is available.

Equation (8-2) was used for the generator optimization of the IT and NMT configuration shown in table 8-2. The CAPEX assumptions used for the optimization are shown in table 8-4. It should be noted that the cost of the cryogenic cooling system is assumed similar to a study of a low temperature superconducting generator by Wang [69]. It is assumed that the power needed to operate the cryogenic cooling system is 50 kW being 0.5 % of the full rated power of the turbine, but for a simple cooling system based on cryo-coolers then this power consumption is also needed then the turbine is not producing at low wind speeds.

Component	Cost (k€)	Source
Mechanical structure for the generator	456	10 MW PMDD scaling function [70]
Cryostat	590	12 MW LTS generator design [69]
Refrigeration system for cryostat	570	
Power electronics	800	Based on estimation of 80 k€/MW
Other wind turbine components	7500	INNWIND.EU cost model
Balance of plant	17000	
Total	26916	-

Table 8-4. CAPEX assumptions for the optimization of the 10 MW IT SCDD generator.

Figure 8-9 shows the mechanical input power curve as well as the resulting curves after subtracting the losses of the generator and power electronics. Figure 8-10 is showing the different loss components resulting in the efficiency curve of figure 8-11. The energy loss is found in figure 8-12 by integrating over the Weibull distribution.

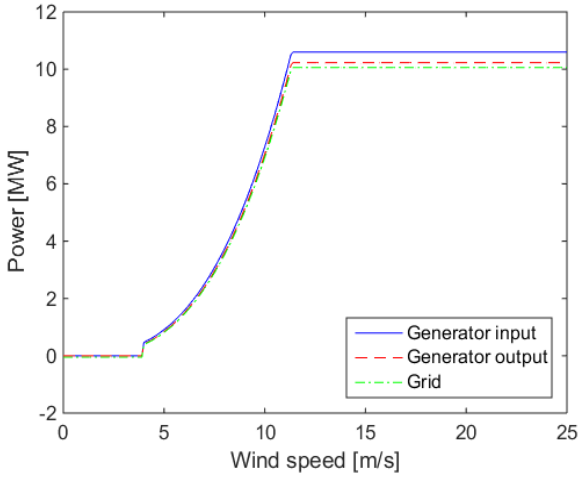

Figure 8-9. Resulting power curve of 10 MW SCDD IT generator after subtracting the generator losses and power electronic losses.

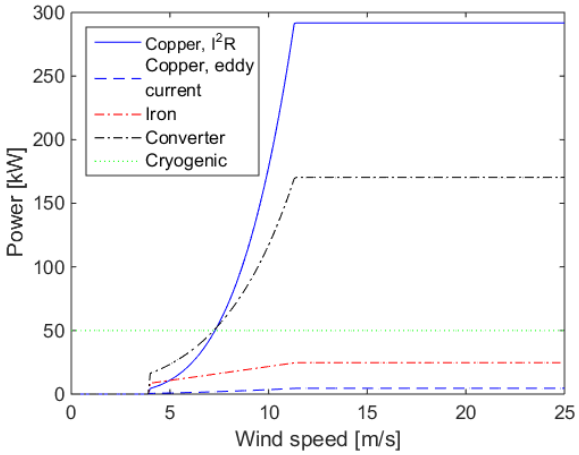

Figure 8-10. Loss components of the IT generator and power electronics system for a 10 MW SCDD turbine.

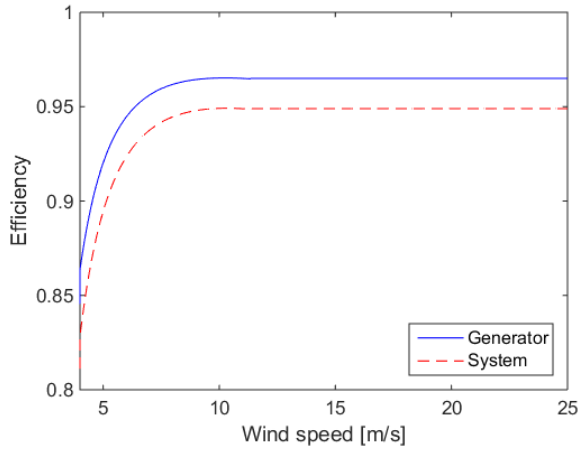

Figure 8-11. Partial load efficiency of 10 MW SCDD IT generator and also including estimates of the power electronics losses.

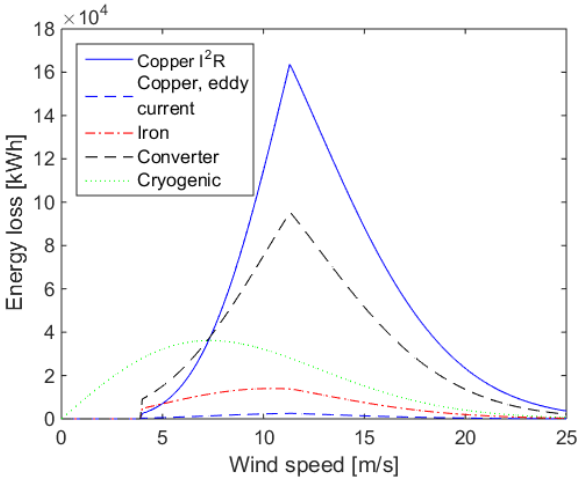

Figure 8-12. Energy losses of 10 MW SCDD IT generator as determined from the Class Ia wind distribution.

It should be noticed that the power curve for the SCDD generator as shown in figure 8-9 is negative in the wind speed interval from zero and up to the cut in wind speed V = 0-4 m/s due to the power consumption of the cryogenic system, which is assumed to be running all the time in order to keep the turbine ready for power production. The efficiency curve of figure 8-11 is only showing the efficiency of the operation wind speeds of the turbine, since the definition of efficiency as power loss divided by power production is ill defined below the cut-in wind speed. One will however have to take the losses below rated wind speed into account and that is done by integrating the cryogenic power loss below cut-in wind speed as shown on figure 8-12 and subtracting that from the Annual Energy Production (AEP). The 50 kW power consumption is based on having a number of cryocoolers running constantly and represent a simple cooling system, where the cooling power cannot be regulated. The loss correspond to 0.5 % of the rated power of the turbine, but when integrated over a year it corresponds to 0.44 GWh per year, which is about 1 % of the AEP of the turbine as reported in table 8-2. The main concern of the cryogenic system is however the amount of hour with wind speeds below cut-in wind speed of 4 m/s, which amounts to 1550 hours or 17.7 % of the year where the turbine is not producing.

The energy consumption for running the cryocoolers in that period is E = 50 kW x 1550 hours = 77.5 MWh or 0.2 % of AEP. With an approximate Cost of Energy CoE ~ 100 €/MWh for offshore wind power then the cryogenic power loss corresponds to 77.5 k€/year or 1.94 M€ over the 25 year life time of the turbine. Thus it will be relevant to investigate if the stand-still power loss can be decreased by a more advanced cryogenic cooling system, but the added cost should not be more than about 1-2 M€. An alternative strategy could be to turn off the cryocoolers in case of no production and start them sometime before restarting production depending on the final heating / cooling time constants of the system. This must be investigated as then cryostat design is more mature.

8.6 Nacelle cost estimates

The integration of the superconducting direct drive and the Pseudo magnetic direct drive (PDD) generator into the INNWIND.EU reference nacelle have been investigated by several engineering tools at DNV-GL [71]. An estimation of the mass of the nacelle components are found in table 8-5 and the associated costs are listed in table 8-6. It should be noticed that these estimates are based on some simple assumption about the turbine loads and that further work is needed to confirm the accuracy of these estimates.

Type:	INNWIND 10-178	INNWIND 10-198	INNWIND 20-252	INNWIND 20-280
Rating [MW]	10	10	20	20
Rotor Diameter [m]	178	198	252	280
Blade Mass [kg]	40,000	50,000	80,000	100,000
Hub Mass [kg]	115,000	150,000	360,000	425,000
Rotor Mass [kg]	235,000	300,000	600,000	725,000
PDD/SCDD [kg]	120,000	120,000	200,000	200,000
Other Nacelle Mass [kg]	220,000	260,000	275,000	350,000
Nacelle Mass [kg]	340,000	380,000	475,000	550,000
RNA Mass [kg]	575,000	680,000	1,075,000	1,275,000
Blade Mxy [kNm]	60,000	76,000	172,000	216,000
Pitch Bearing PCD 8-point [m]	5.5	6.2	9.3	10.4
Hub Stationary My [kNm]	51,000	64,000	143,000	181,000
Hub Stationary Fz [kN]	3,200	4,100	8,100	9,800
Main Bearing Spacing [m]	4.2	4.8	7.2	8.0
LSS Torque [kNm]	9,899	9,000	28,000	25,455
LSS Torque + incr.	12,000	11,000	35,000	32,000

[kNm]				
Yaw Bearing Mxy [kNm]	71,000	89,000	200,000	252,000
Pitch Bearing PCD 8-point [m]	5.1	5.7	8.5	9.6

Table 8-5. Dimensions and loads used to dimension the INNWIND.EU nacelle holder a superconducting Direct Drive (SCDD) or magnetic Pseudo Direct Drive (PDD) generator [71]

Type	Innwind 10-178	Innwind 10-198	Innwind 20-252	Innwind 20-280
Mass Hub [kg]	60,000	66,000	125,000	128,000
Mass Blade Extenders	50,000	56,000	113,000	144,000
Mass Pitch Bearings	27,000	33,000	75,000	99,000
Mass other Rotor parts	15,000	18,000	24,000	30,000
Total Rotor Mass	152,000	173,000	337,000	401,000
Mass Main Bearings	10,000	10,000	25,000	27,000
Mass Kingpin	51,000	61,000	129,000	161,000
Mass Mainframe	58,000	72,000	107,000	142,000
Mass Yaw bearing	17,000	19,000	28,000	32,000
Mass other Nacelle parts	30,000	35,000	50,000	55,000
Total Nacelle Mass excl gen	166,000	197,000	339,000	417,000
Total Structural Mass excl gen	318,000	370,000	676,000	818,000

Table 8-6. Mass of the main components of the INNWIND.EU nacelles [71]

Type	Innwind 10-178	Innwind 10-198	Innwind 20-252	Innwind 20-280
Cost Hub [€]	€180,000	€198,000	€375,000	€384,000
Cost Blade Extenders	€150,000	€168,000	€339,000	€432,000
Cost Pitch Bearings	€378,000	€462,000	€1050,000	€1386,000
Cost other Rotor parts	€150,000	€180,000	€240,000	€300,000
Total Rotor cost	€858,000	€1008,000	€2004,000	€2502,000

Cost Main Bearings	€300,000	€300,000	€750,000	€810,000
Cost Kingpin	€153,000	€183,000	€387,000	€483,000
Cost Mainframe	€174,000	€216,000	€321,000	€426,000
Cost Yaw bearing	€255,000	€285,000	€420,000	€480,000
Cost other Nacelle parts	€300,000	€350,000	€500,000	€550,000
Total Nacelle Cost excl gen	€1182,000	€1334,000	€2378,000	€2749,000
Total Structural cost excl gen	€2040,000	€2342,000	€4382,000	€5251,000

Table 8-7. Cost of the main components of the INNWIND.EU nacelles [71]

8.7 Conclusion

The Key performance indicators of the superconducting direct drive generators have been presented for the 10 MW MgB_2 topology after cost of energy optimization have been applied (see evolution from figure 8-5 to figure 8-7). It is concluded that the economical most optimal generator topology contains as much iron as possible in form of a salient pole configuration, which is magnetized by a superconducting rotor winding. This philosophy was followed after the recommendation from WP1 that weight does not matter to much, but it remains to be investigated if the current generator proposal has actually become "too heavy" in term of structural loads in the nacelle and the turbine. From Table 8-5 it is seen that the initial assumption about the generator mass is 120 tons, whereas the current design is about double of that.

Finally a cost of the nacelle components can be compiled

Component	Cost (k€)	Source
Generator active materials	687	Table 8-2. Optimizing for low Cost of Energy
Mechanical structure for the generator	456	Table 8-4. Must be confirmed by structural design
Cryostat	590	Table 8-4. Specific design for IT generator must be done to confirm this. Cooling loss = 50 kW.
Refrigeration system for cryostat	570	
Power electronics	400-800	Table 8-3 from INNNWIND Deliverable D3.31
Cost of nacelle structure	2040	Table 8-7. Structural integrity must be confirmed.
Total	5143	-

Table 8-8. Cost breakdown of 10 MW MgB2 IT superconducting generator.

These parameters have been provided the INNWIND.EU Cost of Energy calculator of WP1 together with the expected efficiencies of the superconducting generator proposals outlines above.

CHAPTER 9 MAGNETIC PSEUDO DIRECT DRIVE GENERATOR (PDD)

9.1 Introduction to the Innovative Concept

9.1.1 State of the art and motivation

A magnetic gear is combined with an electrical machine to realize a magnetically geared drive of high torque density in various ways. The magnetic pseudo direct-drive (PDD) generator is realizing the possibility of applying magnetic gears in wind turbines. In a PDD generator, the magnetic gear and the electrical generator are mechanically as well as magnetically integrated.

When compared to the basic arrangement of magnetic-gear machines, the PDD

- facilitates access and cooling of the stator winding and
- simplifies manufacturing significantly, especially for large machines since it only has two air gaps.

Prototypes of PDD machines have been designed and tested for various applications. PDD machines with a continuous torque output of 4 kNm to ~20 kNm have been tested. Developments in INNWIND.EU are in progress to increase torque to magnitudes required for wind turbines.

9.1.2 Brief description of the concept

The PDD employs a magnetic gear stage, and the purpose of this is twofold. Firstly the size of the generator is minimised by virtue of the torque converter which is analogous to a mechanical gear in this respect and secondly the (mechanical) gearbox system with the very high “consequence of failure” is removed from the system.

A PDD is a full magnetic and mechanical integration of an electrical generator and magnetic gear. The resulting electrical machine, which is shown in the figure below, has been called the Pseudo-Direct Drive (because it has the characteristics of a direct-drive machine, although it uses a magnetic gear to achieve its very high torque-densities).

The PDD consists of three components:

- Outer stator, comprising a conventional lamination stack with copper windings, and stationary outer magnets
- Inner permanent-magnet array rotating at high-speed with no external mechanical connection
- Intermediate annular component, the modulating rotor, with ferro-magnetic pole-pieces, rotating at low-speed and connected to the input shaft of the generator.

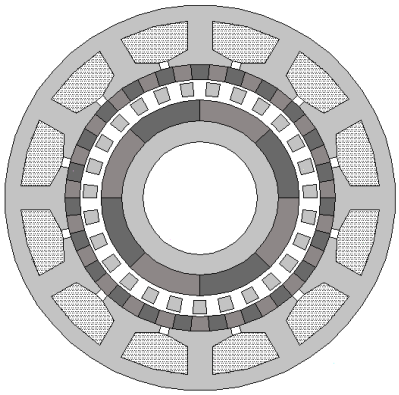

Pseudo-Direct Drive (PDD)

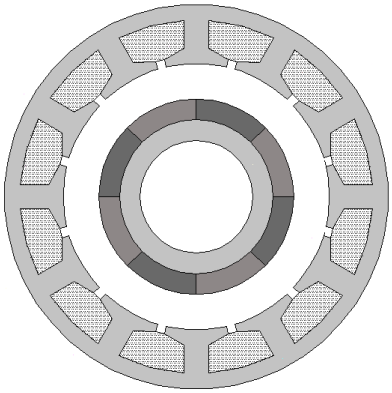

Components forming the PM generator

The principal of operation of the PDD can be understood by considering the operation of the different sub-components within it; i.e. the magnetic gear and the electrical machine. The components it shares with the magnetic gear are evident from the above figures, which also shows the elements of the device which contribute to its operation as an electrical machine; i.e. the outer lamination stack with the copper windings and the inner permanent magnet rotor. Thus the inner rotor contributes to the operation of both the electrical machine and the magnet gear, and, as a result, the PDD uses less magnet material than would be used by a combination of a magnetic gear and separate electrical machine. Further, the PDD is controlled in an identical manner to a conventional direct-drive PM machine, through the use of existing full-rated power converter technology.

9.1.3 Anticipated PROS and CONS

The PDD designs have the following advantages:

- Because of the inherently low electric loading, the rated efficiency can be more than 98%.
- The total mass of generator, including the structural components, is relatively low. It is anticipated that the size/mass of PDD generators would be less than 50% of that of permanent-magnet direct-drive generators.
- Although the quantity of permanent magnets in a PDD machine may be higher, this can be significantly reduced by appropriate optimization. Another idea to reduce the use of permanent magnets is to use electrical excitation to replace some of the permanent magnets.

Summarizing, the most important advantages of the PDD are

- the anticipated reduction of weight compared to direct-drive generators and
- the significant reduction of maintenance compared to mechanical gearboxes.

The most important disadvantage is the large amount of permanent magnet material.

9.2 Assessment of the Structural Integrity of the Proposed Design

9.2.1 Design layout and dimensioning

The magnetic pseudo direct drive train has been investigated both from an experimental point of view by performing a demonstration in task 3.2.2 and by theoretical investigations as done in task 3.2.1.

Magnomatics has designed manufactures and tested a down-scaled PDD model generator as described in deliverable D3.22 [72], whereas University of Sheffield has validated theoretical optimization models of the PDD against finite element calculations in deliverable D3.21 [73].

Table 9-1 is summarizing the key performance indicators of the machine properties expected at P = 10 MW and 20 MW for the INNWIND.EU turbines.

Figure 9-2 is showing the resulting efficiency curves for the PDD at P = 10 MW and 20 MW.

Symbol	Quantity	Value for 10MW	Value for 20MW
	Rated power	10 MW	20MW
$\Omega_{PP,R}$	Rated speed of PP rotor	9.65 rpm	6.82 rpm
	Rated torque on the PP rotor	9.9 MNm	28.0 MNm
	Analytical pullout torque of the MG	11.9 MNm	33.7 MNm
$f_{out,R}$	Rated electrical output frequency	48.25 Hz	34.1 Hz
G	Gear ratio	7.5	7.5
p_{HS}^*	Pole-pairs on HS rotor per section	2	2
p_S^*	Pole-pairs on stator per section	13	13
m_S	Halbach segments per pole-pair on the stator	4	4
Q^*	Pole-pieces per section	15	15
S	Number of identical sections	20	20
	PP slot opening angle	$\pi/300$ rad	$\pi/300$ rad
D	Airgap diameter	6.0 m	8.5 m
w_{PP}	Radial thickness of PPs	31.4 mm	44.4 mm
	Radial thickness of HS rotor PMs	39.8 mm	56.3 mm
	Radial thickness of stator PMs	25.2 mm	35.6 mm
	Length of inner airgap	6.0 mm	8.5 mm
	Length of outer airgap	6.0 mm	8.5 mm
l_a	Active axial length	1.66 m	2.35 m
	HS rotor pole arc to pole pitch ratio	0.8	0.8
B_r	Remanence of N48SH PMs at 100°C	1.25 T	1.25 T
μ_r	Relative recoil permeability of PMs	1.05	1.05
	Copper packing factor	0.5	0.5
	Current density at rated power	2.0 A_{rms}/mm^2	2.0 A_{rms}/mm^2
	PM mass	13.5 tons	38.2 tons
	HS rotor and PP rotor laminated steel mass	14 tons	39.6 tons
	Stator laminated steel mass	15.5 tons	45 tons
	Copper mass	7 tons	14 tons
	Estimated structural mass **	100 tons	383 tons
	Estimated total mass	150 tons	520 tons

** The structural mass for the 10MW design is assumed to be 2 times the active mass,

a similar factor as for the 10MW design given by Magnomatics in [74]. Furthermore, the ratio of structural mass to active mass is assumed to scale with the diameter, hence a factor of 2.8 is assumed for the 20MW design.

Table 9-1. Properties of the Magnetic Pseudo Direct Drive generators for the INNWIND.EU turbines [73]

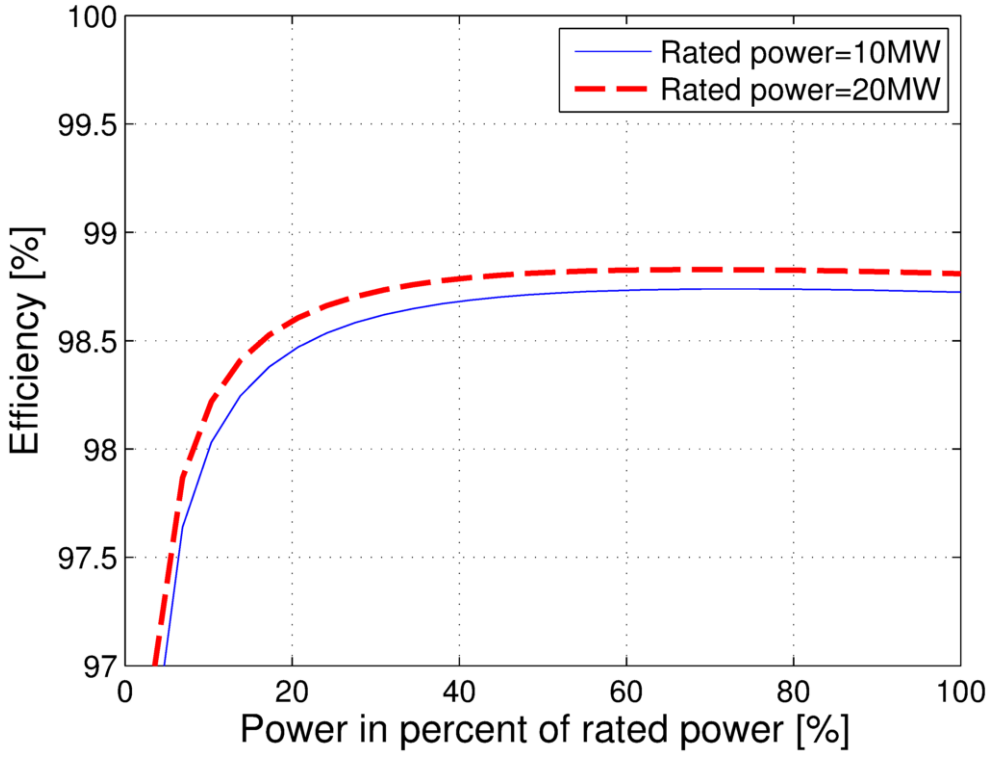

Figure 9-1. Variations of the electromagnetic efficiency with the power in percent of the rated power as reproduced from [73]

The properties of the down scaled demonstrator are shown in table 9-2 and figure 9-2 is showing the machine being tested in the lab at Magnomatics.

Symbol	Quantity	Value
	Rated speed of PPR output rotor	300 rpm
	Peak torque (slip torque of magnetic gear)	6.3 kNm
	Rated torque (fan cooled/water cooled)	3/5 kNm
	Torque per unit current	16.2 Nm/Arms
	Rated electrical output frequency	165 Hz
	Gear ratio	5.5:1
	Pole-pairs on HS rotor	6
	Pole-pairs on outer magnet array	27
	Number of pole-pieces	33
	Number of slots	18
	Outer diameter stator lamination	480mm
	Outer airgap diameter	363mm
	Radial thickness of PPs	18 mm
	Radial thickness of HS rotor PMs	21 mm
	Radial thickness of stator PMs	10 mm
	Length of inner airgap	1.5 mm
	Length of outer airgap	1.5 mm
	Active axial length	302 m
	NdFeB magnet grade	N40SH
	Copper packing factor	0.34
	PM mass	65 kg
	HS rotor and PP rotor laminated steel mass	64 kg
	Stator laminated steel mass	120 kg
	Copper mass	26 kg
	Total active mass	275 kg

Table 9-2. Properties of the down-scaled demonstrator of the Magnetic Pseudo Direct Drive generators for the INNWIND.EU turbines [72]

Figure 9-2. Picture of Magnomatics PDD demonstration machine (left) being tested in a drive train test bench at Magnomatics [72]

9.3 Conclusions

A down scaled Magnetic pseudo direct drive (PDD) generator has been designed, build and tested by magnomatics. Secondly theoretical optimizations have been used to determine the best PDD configuration for P = 10 and 20 MW. These parameters have been supplied to WP1 for evaluation of the resulting Cost of Energy.

CHAPTER 10 BOTTOM MOUNTED OFFSHORE SUPPORT STRUCTURE

10.1 Introduction to the Bottom-Mounted Jacket

10.1.1 State of the Art and Motivation

Jacket type support structures are the preferred solution for medium water depths where monopile solutions are reaching manufacturing limits, installation limits or cost effective limits. Wind farms using jacket support structures are typically located in water depths between 25m-60m, which is the range of wind farms under operation or planned by today. The development of competitive monopiles increases its applicability for deeper waters. Hence the lower limit of the water depth for jackets will increase.
The jacket concept has huge optimization potential with respect to manufacturing and assembly. Especially in large wind farms with the need for optimal clustering of structures. However it can be seen that the assembly and manufacturing strategies are insufficiently integrated in the design and the cost estimation by using reduced lumped prizes per unit weight only. This leads to mass optimized structures as the governing cost indicator and neglects important shares of other costs. It is aimed for a more detailed refinement of the cost contributors, namely material, volume/length and type of welding, assembly and mass production benefits.

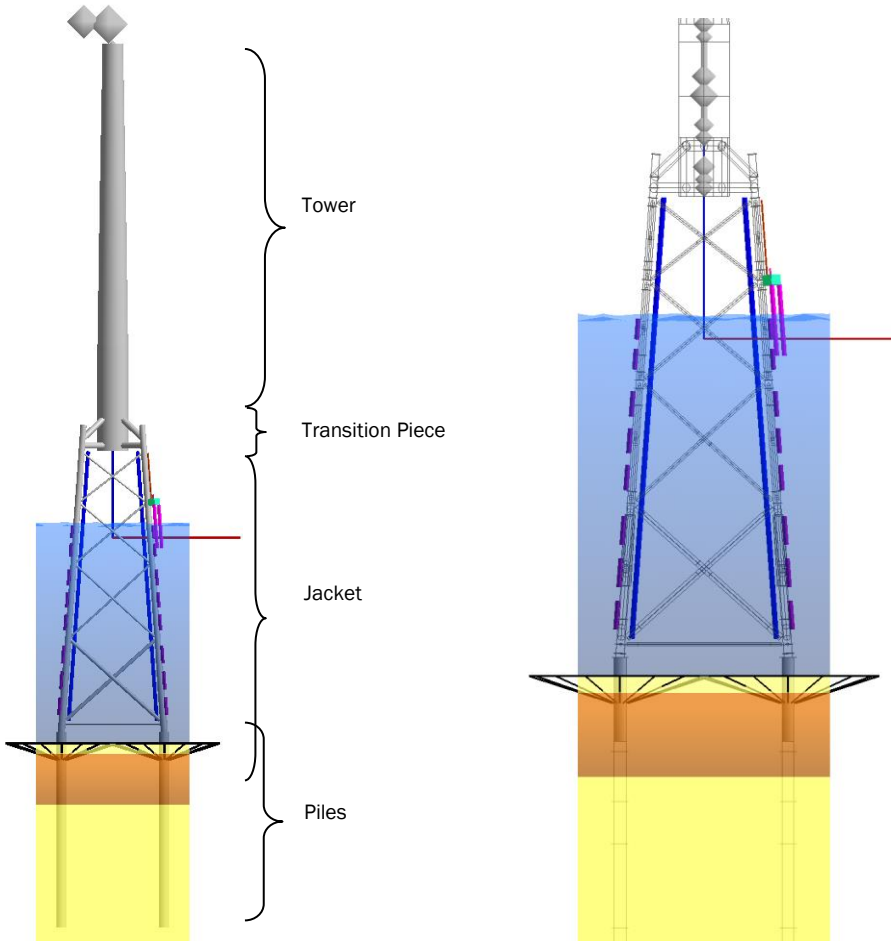

Figure 10.1-1: Overall view of the ROSA jacket model showing mass and area appurtenances.

10.1.2 Brief Description

The general jacket foundation concept is characterized by a number of legs, which are stiffened by braces. The legs are supported by piles. The connection to the cylindrical tower is achieved through a transition piece, which is made of steel. For the present design, a four legged jacket with a generic strutted beam transition piece, four levels of X-bracings and four piles is used.

The jacket foundation as well as the tower is modelled with the Ramboll in-house FE-program ROSAP using tubular beam elements for the legs, braces and piles. Timoshenko beam theory is applied. The pile-soil interaction is modelled by means of soil springs (p-y, t-z, Q-w curves) in accordance with the API standard.

The elements connecting the jacket and the tower are modelled in ROSA as a strut model. This method leads to a simplification of the transition pieces mass and stiffness properties and could be evaluated in more detail. Ideally, a detailed FE-analysis of the transition piece should be conducted in order to optimize the structure. This will be part of the jacket design updates in a later stage of INNWIND.EU.

Figure 10.1-1 shows a 3-D model of the jacket foundation including sea, soil, scour and appurtenances, ref. [75]. The appurtenances are modeled as discrete or distributed masses and areas, such as the boat landing, ladders, external J-tubes and anodes. Wave loads on appurtenances are calculated by ROSAP and are applied to the structure. Dynamic wave loads, turbulent wind loads, gravity and buoyancy loads are also taken into account for all time domain structural load simulations. Design procedures consider the further effects of the marine environment, e.g. marine growth, corrosion, etc. Design checks for ULS, FLS and NFA are performed.

10.2 Assessment of Structural Integrity

10.2.1 Final Design Layout and Dimensions

An overview of the main jacket geometrical parameters is shown in Table 10.2-1. Please refer to the design report D4.31 for all details and design results, ref. [75].

Table 10.2-1: Overview of jacket geometry and masses

Structural member	Dimensions	Value
Jacket		
Base Width	[m]	34
Top Width	[m]	14
Interface elevation	[m] wrt MSL	26
Transition Piece height	[m]	9
Batter angle of the legs	[°]	12.2
Number of legs	[-]	4
Jacket legs diameter (outer)	[mm]	1400
Jacket legs maximum wall thickness	[mm]	120
Jacket legs minimum wall thickness	[mm]	42
Number of x-braces levels	[-]	4

Max. Upper x-braces diameters (outer)	[mm]	900
Max. Upper x-braces wall thicknesses	[mm]	50
Max. Middle upper x-braces diameters (outer)	[mm]	876
Max. Middle upper x-braces wall thicknesses	[mm]	38
Max. Middle lower x-braces diameters (outer)	[mm]	968
Max. Middle lower x-braces wall thicknesses	[mm]	34
Max. Lower x-braces diameters (outer)	[mm]	1088
Max. Lower x-braces wall thicknesses	[mm]	44
Number of horizontal braces levels	[-]	1
Max. Horizontal braces diameter	[mm]	1044
Max. Horizontal braces wall thickness	[mm]	22
Number of Piles	[-]	4
Pile penetration	[m]	40
Pile diameter	[mm]	2438
Pile wall thicknesses	[mm]	32-52
Pile top elevation above mudline (Stick-up length)	[m]	1.50
Overlap length (grout length)	[m]	10.0
Mass		
Jacket structure	[t]	1210
Transition Piece (estimation)	[t]	330
Steel Appurtenances (estimation)	[t]	80
Piles (all)	[t]	380
Grout (estimation)	[t]	120
Total	[t]	2120
Natural frequency overall structure		
1st eigenfrequency (1st bending mode)	[Hz]	0.287

10.2.2 Design Load Cases

The load calculations are based on IEC 61400-3 design load cases (DLC) with appropriate partial safety factors. It is assumed that the turbine has 100% availability. Wind and waves are aligned and 12 directions (30° increment) are considered. Turbulent seeds are combined with yaw error scenarios. The following DLCs have been applied:

- DLC 1.2 FLS
- DLC 6.4 FLS
- DLC 2.1 ULS
- DLC 2.3 ULS
- DLC 6.1 ULS
- DLC 6.2 ULS

The simulations are based on a sequential integrated calculation approach for every time series. Aero-elastic simulations of wind loads are performed with the help of LACflex using a model of the offshore wind turbine consisting of the rotor-nacelle-assembly, the tower and the foundation superelement from ROSAP. The resulting dynamic responses at interface in terms of load time series of all six components (Fx, Fy, Fz, Mx, My and Mz) are extracted from LACflex and subsequently applied at the support structure interface and combined with the hydrodynamic loads of the sea state in order to obtain the full dynamic responses of the foundation structure for each load case.

10.2.3 Structural Integrity Check

Design assessment for NFA, ULS and FLS is based on the DNV guideline, ref. [76] and [77]. Appropriate safety factors for loads and material are taken into account. Refer to the design report for detailed descriptions, ref. [75].

The purpose of the NFA analysis is to demonstrate that the natural frequency of the entire structure falls inside the allowable frequency band between 1P and 3P. 1P is the lower limit corresponding to rotor frequency, 1P = (rotor speed in rpm) / 60. 3P is the upper limit being the blade passing frequency, 3P = 3 x (rotor speed in rpm) / 60. A structure with the first natural frequency placed between the given limits refers to a soft-stiff configuration.
The obtained natural frequency of the system will be utilized in other analyses, such as the fatigue analysis, where the damping of the system is calculated by applying Rayleigh-damping.

The purpose of the extreme event analysis is to ensure that the jacket structure is capable of supporting the WTG for the least favourable combination of environmental load conditions. The jacket element stresses and tubular joints punching shear stresses are analyses for all members and load cases. The maximum allowed utilization has to be smaller than one.

The purpose of the time domain fatigue analysis is to ensure that the jacket structure is capable of supporting the WTG for the required design life of 25 years. In addition, site specific conditions in terms of water depth, marine growth, corrosion allowance and soil characteristics are applied for the turbine location. Hot spot stresses are evaluated using the approach of stress concentration factors (SCF). S-N curves for different types of tubular joint welds, butt welds, cut-outs, conical sections and attachment welds are considered.

10.3 LCOE Impact

10.3.1 Effect on Annual Energy Production

The influence of the jacket, i.e. the motion of the structure, on the annual energy production of the wind turbine is negligible. The gained power is mainly driven by the mean wind speed and wind distribution, the rotor performance and the availability of the turbine.

10.3.2 Effect on CAPEX

Costs drivers for the support structure are the material costs (weight of the structure), the welding costs (number of welds and volume/length) and the assembly costs. Due to its complexity only lumped prices per tonnage of the structure are usually applied, based on manufacture's experiences from realized projects. A more detailed approach should distinguish the different cost contributions to determine a cost effective support structure designs instead of misleading pure mass optimization. Mass optimized structures result in individual optimized cross sections of braces and legs and consequently in higher costs for welding and assembly, which can compensate the material costs savings. In a cost study [78] it has been shown that the assembly strategy can lead to variations of up to 20%.

10.3.3 Effect on OPEX

There are no OPEX related cost savings. The support structure is designed to survive the entire lifetime without maintenance of the primary steel components. Inspections of corrosion and scour monitoring might be of relevance to assess the design assumptions.

10.4 LCOE Sensitivity Analyses

A LCOE variation study using the INNWIND.EU cost model (v1.01) of reference wind turbine is performed. The influence of the CAPEX costs of the support structure on the LCOE is addressed. The results are shown in Table 10.4-1:

Table 10.4-1: LCOE variation study for bottom fixed support structure costs

	Support structure cost	LCOE	Change of LCOE
Base case ref. design (TP, Jacket, Piles	9.5 mio €	91,93 €/MWh	-
Jacket -5%	9.15 mio €	91,25 €/MWh	-0.74%
Jacket -10%	8,80 mio €	90.57 €/MWh	-1.48%
Jacket -15%	8.45 mio €	89.88 €/MWh	-2.23%
Jacket -20%	8.10 mio €	89.20 €/MWh	-2.97%

10.5 Conclusions and Recommendations

The design of a jacket support structure with pre-installed piles has been performed based on NFA, ULS and FLS assessment [76]. The design driving load cases DLC 1.2, 2.1, 2.3, 6.1, 6.2, 6.4 are applied.

The foundation costs influence only the CAPEX of the wind turbine system there is no benefit for the energy yield. There is also no influence on operational costs in the scope of the primary steal design. The assessment of the material, welding and assembly costs has been performed [78], which results in a cost saving potential of up to 20%. The change of CAPEX influences to LCOE up to 3%.

CHAPTER 11 SEMI-SUB FLOATER DESIGN

11.1 Introduction

In this chapter, a floating platform concept developed by CENER for the INNWIND 10MW wind turbine [62] within the project task 4.3 "Design of Offshore Support Structures" is presented. The chapter summarizes the technical characteristics of the support solution, including the stability curve, the hydrodynamic behaviour, the natural periods, an estimation of the mass of steel required for the construction that is based in the structural calculation and, finally, an estimation of the platform cost. More details on the methodology, assumptions, and calculations can be found in the project deliverable 4.33 [79].

11.2 Design concept

The concept is an asymmetric semi-submersible floater designed for a sea depth of 200m. The design conditions for the platform are described in detail in [80]. The great stability of the semi-submersible concept allows assembling the platform in the dock. Afterwards, the assembled wind turbine can be towed to the desired location, decreasing the costs in transport. In addition, the area of the water plane section is not high, improving the behaviour of the platform under the wave loading. This type of concept is also very versatile and can be installed in a very wide range of different depth locations.

A disadvantage of the semisubmersible concept is that the construction can be complex, because the vertical cylinders have to be connected by pontoons or by tubular structures requiring welding. To minimize these disadvantages, the proposed concept is composed by three cylinders connected by pontoons, forming a geometrically simple shape. The material and construction cost is reduced avoiding bracings and other connecting structural elements. The function of the pontoons is not only structural, but also hydrodynamic: the pontoons behave as heave plates to damp the motion of the offshore wind turbine. In addition, to simplify the structure, the wind turbine is mounted on one of the cylinders, instead of building a central structure to hold it in the platform center. The center of gravity is lowered to increase stability through the use of sea water as ballast. Part of the platform ballast is active to counteract the variations in the overturning moment direction introduced in the platform by the rotor due to changes in the wind direction. Figure 11.1 presents a tri-dimensional model of the concept design:

Figure 11.1 – Isometric view of the floating platform

To have an overlook of the platform dimensions, the main geometric characteristics of the platform are presented in Table 11.1 :

Table 11.1 – Platform main characteristics

Main characteristics	
Distance between columns	**66 m**
Draft	**25.5 m**
Platform depth	**37.5 m**
Freeboard	**12 m**
Column diameter	**14.5 m**
Pontoon breadth	**10.875 m**
Pontoon depth	**7 m**
Buoyancy volume	**24907 m^3**
Center of buoyancy	**0, 0, -17.32 m**

Figure 11.2 illustrates the dimensions of the platform. The origin of the reference system is located in the geometric centre of platform and at the sea water level (SWL). All the physical properties and results presented in this chapter are referred to this reference system.

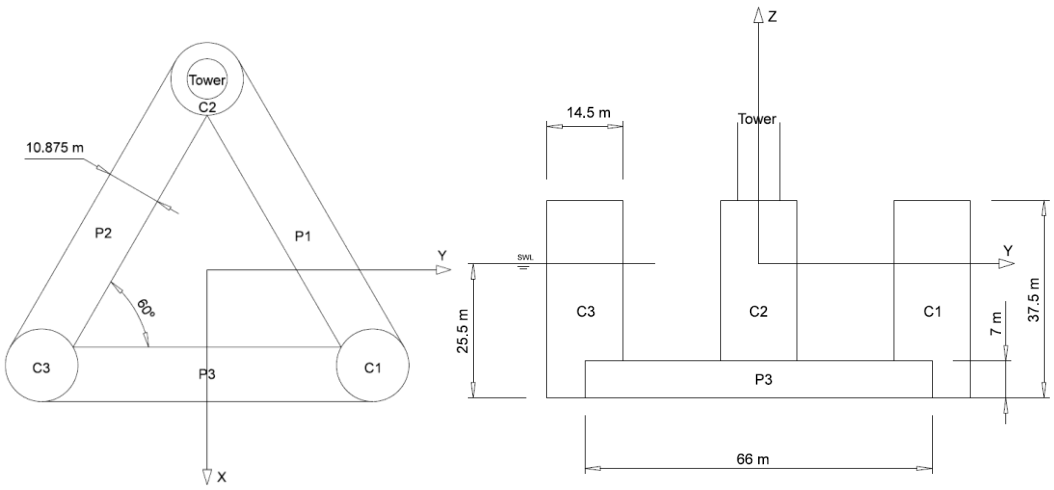

Figure 11.2 – Top view (left) and side view (right) of the platform and reference system

11.3 Estimation of the platform required steel mass

The platform structural design has been performed according to the DNV guidelines ([81], [82] and [83]) and using a configuration composed by frames. These guidelines provide indications and requirements for the local structural design of the platform. Nevertheless, a final verification of the global structural behaviour of the design is required and a reinforcement of certain parts of the platform could be necessary. This global verification of the platform is out of the scope of this preliminary platform design and will be done in future steps of the project. A detailed description of the structural design is skipped here, but can be found in the project deliverable 4.33 [79]. Figure 11.3 and Figure 11.4 show the internal structure elements of the pontoons and columns: as web frames, bulkheads, decks and longitudinal bulb and T stiffeners.

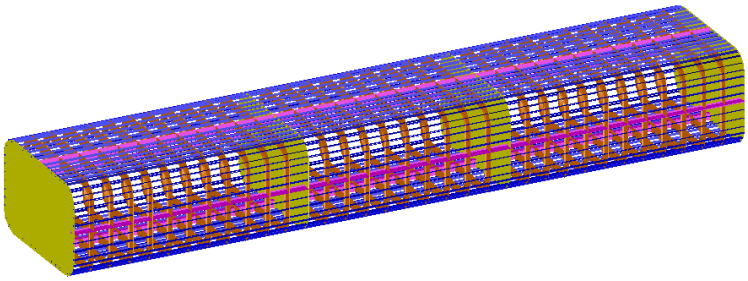

Figure 11.3 – Pontoon internal structure CAD model

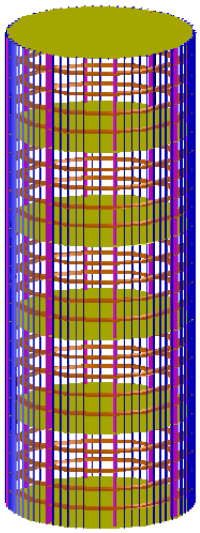

Figure 11.4 – Column internal structure CAD model

The mentioned structural design has provided the thickness for the different components of the platform, including the web frames, bulb and T stiffeners, column rings, bulkheads and decks to guarantee the structural integrity of the system. Based on this structural design the total weight of the platform can be estimated. The total weight is calculated from the density and volume of steel of the different structural elements that we have dimensioned, according to the next expression:

$$m_{steel} = \rho_{steel} \cdot V = \rho_{steel} \cdot A_{steel} \cdot t_{steel} \quad (1)$$

The thickness. $T_{steel,}$ of the different components of the platform was obtained from the structural design and the areas (A_{steel}) of these components from the main frame sections, using Autocad3D. An additional 30% of the internal tanks bulkheads weight was added, accounting for the associated reinforcements. Another extra 2% of the total web frames weight was added to take into account the weight of the brackets. Furthermore, an extra 3% of the total weight was included to take into account the weight of welding.

Table 11.2 presents a summary of the calculation of the total weight of the structure element by element. The total weight of steel obtained is 3745,1 t. In addition, the total weight of the mooring system has been estimated in 94.7 t and will be included in the cost evaluation of the system.

Table 11.2 – Calculation of the structural weight of the platform

Pontoons				
Central tank	Area (cm^2)	Length cm)	Number	Weight (kg)
Longitudinal stiffeners	23,6	1550	52	14932,0
Web frames	94,6	2376	9	15879,6
Shell	1650	2376	1	30774,4

Stringers	94,6	1550	4	4604,2
Side tank	Area (cm^2)	Length (cm)	Number	Weight (kg)
Longitudinal stiffeners	23,6	1800	52	17340,3
Web frames	94,6	2376	11	19408,9
Shell	1650	2376	1	30775,1
Stringers	94,6	1800	4	5346,8
Bulkheads	741935,8	1,1	4	25626,5
Reinforcement bulkheads			30%	7687,9
Sum				278561,2
Total			3	835683,5
	Columns			
Section 1	Area (cm^2)	Length (cm)	Number	Weight (kg)
Longitudinal stiffeners	22,6	7500	64	85156,8
Rings	125,4	4555	4	17935,6
Shell	825	4555	1	29499,3
Stringers	125,4	7500	8	59063,4
Deck	1651299,6	1,1	1	14259,0
Reinforcements deck			30%	4277,7
Sum				210191,8
Total			3	630575,3
Section 2	Area (cm^2)	Length (cm)	Number	Weight (kg)
Longitudinal stiffeners	22,6	7500	64	85156,8
Rings	97,8	4555	4	13988,0
Shell	675	4555	1	24135,8
Stringers	97,8	7500	8	46063,8
Deck	1651299,6	0,9	1	11666,4
Reinforcements deck			30%	3499,9
Sum				184510,8
Total			3	553532,4
Section 3	Area (cm^2)	Length (cm)	Number	Weight (kg)
Longitudinal stiffeners	22,6	7500	64	85156,8
Rings	63	4555	4	9010,7
Shell	525	4555	1	18772,3
Stringers	63	7500	8	29673,0
Deck	1651299,6	0,7	1	9073,9
Reinforcements deck			30%	2722,2
Sum				154408,9
Total			3	463226,6
Section 4	Area (cm^2)	Length (cm)	Number	Weight (kg)

Longitudinal stiffeners	22,6	7500	64	85156,8
Rings	63	4555	4	9010,7
Shell	525	4555	1	18772,3
Stringers	63	7500	8	29673,0
Deck	1651299,6	0,7	1	9073,9
Reinforcements deck			30%	2722,2
Sum				154408,9
Total			3	463226,6
Section 5	Area (cm^2)	Length (cm)	Number	Weight (kg)
Longitudinal stiffeners	22,6	7500	64	85156,8
Rings	63	4555	4	9010,7
Shell	525	4555	1	18772,3
Stringers	63	7500	8	29673,0
Deck	1651299,6	0,7	1	9073,9
Reinforcements deck				2722,2
Sum				154408,9
Total			2	308817,7
Section 5 (Column support)	Area (cm^2)	Length (cm)	Number	Weight (kg)
Longitudinal stiffeners	22,6	7500	64	85156,8
Rings	125,4	4555	4	17935,6
Shell	825	4555	1	29499,3
Stringers	125,4	7500	8	59063,4
Deck	1651299,6	1,1	1	14259,0
Reinforcements deck			30%	4277,7
Brackets	121712,5	1,1	16	16815,8
Ring structure	99	13801	1	10725,4
Sum				237733,0
Total			1	237733,0
Pontoon-column joint	Area (cm^2)	Length (cm)	Number	Weight (kg)
Shells	2195394	1,1	3	56871,7
Reinforce			30%	17061,5
Total				73933,2
Total structure				3566728,3
Secondary reinforcements and welds			5%	178336,4
Final weight (kg)				3745064,7
Final weight (t)				**3745,1**

Figure 11.5 shows the internal distribution of the tanks for the ballast at the pontoons and columns. Table 11.3 presents the mass and the position of the center of gravity for the whole floating wind turbine, including the ballasts at the pontoons and the columns, for the design

operating condition with a wind speed of 11m/s. The platform ballast is exclusively composed by sea water. This ballast is required to equilibrate the weight of the platform with the buoyancy and also to bring down the center of gravity and achieve the specified platform pitch stiffness. The vertical position of the center of gravity in the global system is -13.46m in the reference system of Figure 11.2.

Figure 11.5 – Internal distribution of the tanks at the pontoons and columns

Table 11.3 – Mass and center of gravity position for the global system including ballasts

Item name	Quantity	Unit Mass (Ton)	Total Mass (Ton)	Unit Volume (m^3)	Total Volume (m^3)	Longitudinal Arm (m)	Transversal arm (m)	Vertical Arm (m)
Unballasted weight	1	4889.0	4889.0			20.99	23.24	13.93
Tank 1	100%	1150.258	1150.258	1122.203	1122.203	23.5	-2.564	-22
Tank 2	100%	990.50	990.50	966.342	966.342	40.25	-2.564	-22
Tank 3	100%	1150.258	1150.258	1122.203	1122.203	57.0	-2.564	-22
Tank 4	100%	1328.215	1328.215	1295.820	1295.820	13.67	16.247	-22
Tank 5	100%	1143.724	1143.724	1115.829	1115.829	23.34	33.0	-22
Tank 6	100%	1010.46	1010.46	985.815	985.815	31.61	47.64	-22
Tank 7	100%	1328.215	1328.215	1295.820	1295.820	66.83	16.25	-22

Tank 8	100%	1143.724	1143.724	1115.829	1115.829	57.16	33.0	-22
Tank 9	100%	1050.629	1050.629	1025.004	1025.004	48.57	47.81	-22
Tank C1.1	100%	1383.647	1383.647	1349.899	1349.899	7.65	-0.04	-21.77
Tank C1.2	0%	1249.532	0.0	1219.056	0.0	14.27	0.0	-18
Tank C1.3	0%	1249.532	0.0	1219.056	0.0	14.27	0.0	-10.5
Tank C1.4	0%	1249.532	0.0	1219.056	0.0	14.27	0.0	-3
Tank C1.5	0%	1249.532	0.0	1219.056	0.0	14.27	0.0	4.5
Tank C2.1	100%	1328.646	1328.646	1349.899	1349.899	72.85	-0.04	-21.77
Tank C2.2	100%	1249.532	1249.532	1219.056	1219.056	73.26	0.0	-14.25
Tank C2.3	100%	1249.532	1249.532	1219.056	1219.056	73.26	0.0	-6.75
Tank C2.4	50%	1249.532	1249.532	1219.056	1219.056	73.44	0.0	-1.1
Tank C2.5	0%	1249.532	0.0	1219.056	0.0	80.47	0.0	4.5
Tank C3.1	100%	851.118	851.118	830.359	830.359	40.25	59.14	-21.75
Tank C3.2	100%	1253.117	1253.117	1222.554	1222.554	40.25	57.16	-14.25
Tank C3.3	0%	1253.117	0.0	1222.554	0.0	47.39	57.16	-10.5
Tank C3.4	0%	1253.117	0.0	1222.554	0.0	47.39	57.16	-3
Tank C3.5	0%	1253.117	0.0	1222.554	0.0	47.39	57.16	4.5
Total			**23180.34**	**28217.68**	**17845.21**	**40.64**	**19.16**	**-13.46**

A summary of the total system masses distribution described above is showed in Table 11.4.

Table 11.4 – Summary of the system masses

System mass	
Wind turbine	**$1.144 \cdot 10^6$ Kg**
Unballasted platform	**$3.745 \cdot 10^6$ Kg**
Ballast	**$1.829 \cdot 10^7$ Kg**
Mooring system	**$2.841 \cdot 10^5$ Kg**
Total mass (m_{FOWT})	**$2.346 \cdot 10^7$ Kg**

The system inertias are presented in Table 11.5 in the reference system defined in Figure 11.2:

Table 11.5 – System inertias

System inertias	
Ixx	**$3.105 \cdot 10^{10}$ kgm^2**
Iyy	**$3.103 \cdot 10^{10}$ kgm^2**
Izz	**$2.373 \cdot 10^{10}$ kgm^2**

11.4 Hydrostatic and hydrodynamic performance of the platform

11.4.1 Hydrostatic pitch and heave stiffness

Table 11.6 shows the total hydrostatic pitch stiffness and also the contributions from buoyancy, gravity and the waterplane. The pitch stiffness fulfils the design requirements defined in [79].

Table 11.6 – Pitch hydrostatic stiffness

Pitch hydrostatic stiffness	
Contribution from buoyancy	$-4.334 \cdot 10^9$ Nm/rad
Contribution from gravity	$3.585 \cdot 10^9$ Nm/rad
Contribution from waterplane area	$3.674 \cdot 10^9$ Nm/rad
C_{55}	$2.925 \cdot 10^9$ Nm/rad

In addition, the platform heave stiffness, based in the area of the water plane section, results in a value of $4.967 \cdot 10^6$ N/m.

11.4.2 Stability

Figure 11.6 shows the computation of the righting moment curve against the inclination angle of the platform:

Figure 11.6 – Platform righting moment

The righting moment increases with the inclination angle until it reaches a maximum close to $2.0 \cdot 10^8$ Nm around 34deg. For higher values of inclination, the righting moment decreases until 92 deg, where the platform would capsize. For an inclination angle of 3.5 deg the righting moment equals the maximum heeling moment ($1.785 \cdot 10^8$ Nm) produced by the rotor thrust at the rated wind speed, which is consistent with the design conditions defined in [80].

11.4.3 Still-water eigenperiods

The heave and pitch eigenperiods have been computed with equation (5) and the results are presented in Table 11.7:

Table 11.7 – Still-water eigenperiod

Still-water eigenperiod	
$T_{eig,33}$	20.66 s
$T_{eig,55}$	24.41 s

The resulting natural periods are higher than 20 s to avoid the periods with more energy of typical wave spectra. If it were necessary, the periods could be increased with a slight redesign of the platform.

11.4.4 Heave and Pitch RAO's

Figure 11.7 shows the heave RAO in the nominal wave direction.

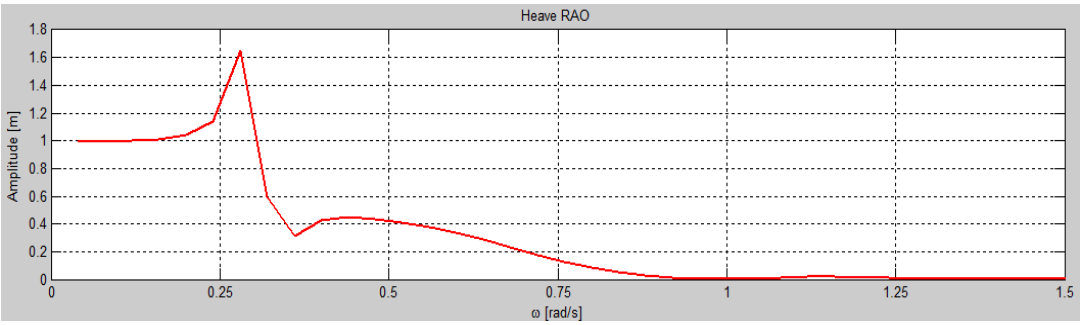

Figure 11.7 – Heave RAO for nominal direction

The plot shows that for very low values of angular frequencies (until 0.13 rad/s) the heave response is 1 meter because the wave length is higher than the platform dimensions. The maximum response appears at a wave frequency close to the heave natural frequency. Finally, for high wave frequencies (higher than 1 rad/s) the platform response in heave is low.
Figure 11.8 represents the platform pitch motion RAO in the wave nominal direction.

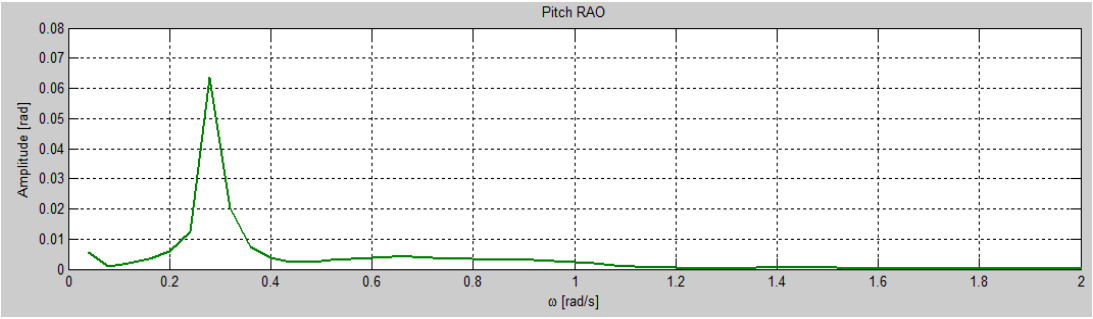

Figure 11.8 – Pitch RAO for nominal direction

The maximum pitch response appears at a wave frequency of approximately 0.28 rad/s, which is close to the pitch natural frequency.

11.4.5 Wave excitation force

Figure 11.9 shows the excitation force in the surge degree of freedom divided by the total floating offshore wind turbine mass, m_{FOWT}, that was presented in Table 11.5:

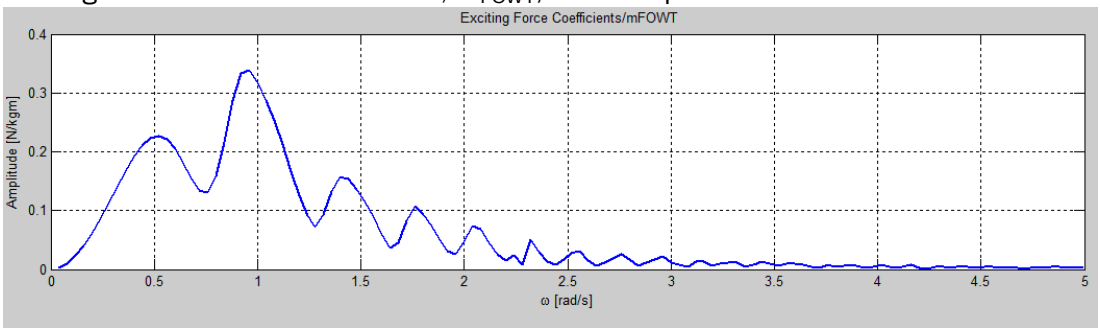

Figure 11.9 – Surge excitation force divided by total floating offshore wind turbine mass

The maximum surge excitation force is located at wave frequency of approximately 0.9 rad/s (7 s of wave period).

Similarly, Figure 11.10 shows the excitation moment in the platform pitch degree of freedom divided by the total inertia in pitch that was presented in Table 11.5.

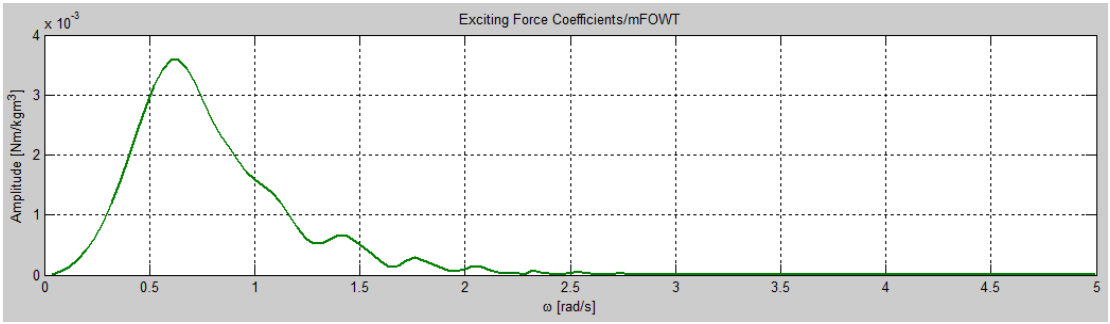

Figure 11.10 – Pitch excitation force divided by floating offshore wind turbine inertia

11.5 Material cost

Table 11.8 summarizes the cost estimation of the platform design. The weight of the platform was presented in Table 11.4.

Table 11.8 – Material cost

Material cost	
Material	**Steel**
Material cost per ton (including welding & manufacturing)	**3,000 €/t**

Platform steel weight	**3,745 t**
Mooring lines total weight	**284.1 t**
Cost of platform	**11,235,000**
Cost of mooring lines	**852,300€**
Cost of anchors	**450,000€**
Total cost	**12,537,300 €**

For the estimation of the cost of the mooring system, it is assumed a cost of 150.000€ per anchor. This assumption gives a total cost of the mooring system of 1.3MM€.
The total cost of the platform (including the mooring system) is 12.54M€.

11.6 Conclusions and outlook

A new conceptual design of a floating platform for a 10MW wind turbine has been proposed. A preliminary evaluation of the concept has been presented. The design presents natural frequencies out of the higher energy frequencies of a typical wave spectrum. The motion and force RAO's show a good performance of the platform with moderate excitation in all the range of wave frequencies considered. The platform also presents good stability behaviour.

A structural design and calculation of the platform has been performed based in DNV's guidelines. A global verification of the structural design, under loads calculated according to guidelines is still pending, but we consider that the current structural design provides a good approximation on the weight of steel required for the construction of the concept.
The total mass of the platform is 23460t, including the water ballast and the wind turbine.

The calculated mass of steel is for the platform is 3745t. Based on this mass, we have estimated an approximate manufacturing cost of the platform of 12.5 MM€. Although it is a rough estimation, the value is reasonable for a 10MW steel platform.

The simulations and results presented in this document are preliminary. Although the performance of the design proposed seems very promising, further testing and analysis is required. Therefore, we estimate a Technology Readiness Level (TRL) of 2.

CHAPTER 12 SYNTHESIS AND CONCLUSIONS

The comparison of the studied concepts in terms of the Performance Indicators (PIs) set for the INNWIND.EU project is presented in Table 12.1 and Table 12.2. The first Table presents dimensional values of the PIs while the second presents percentage changes in comparison to the PI values of the 10MW Reference Wind Turbine. Some promising combinations of the rotor/drive train/support structure concepts are also included in the Tables.

The PI values used in the Tables may be slightly different than those presented in the earlier chapters of the report. This is the result of a harmonization procedure including the recalculation of all the PIs, whenever needed, with dedicated spreadsheets employing the cost model version of Ref [5].

Table 12.1 – Performance Indicators of the innovative concepts studied

ROTOR	Component Mass (tn)	Component Cost (k€)	Overall CAPEX (k€)	Turbine CF	Wind Farm CF	LCOE (€/MWh)
RWT - 10MW	42	448	31000	0.507	0.430	91.93
Low Induction Rotor	45	517	32190	0.545	0.469	86.37
Two-Bladed Rotor R1.08	33	361	30510	0.531	0.450	87.03
Two-Bladed Rotor R1.12	40	430	30910	0.549	0.465	84.97
Smart Rotor (Flaps)	37	419	30860	0.508	0.431	91.43
Carbon Truss Blade Structure	31	389	30720	0.507	0.430	91.38
Bend-Twist Coupled Rotor	41	439	30630	0.507	0.430	91.22
Integrated BTC with IPC	49	531	31300	0.545	0.461	86.36
DRIVE TRAIN & NACELLE	Component Mass (tn)	Component Cost (k€)	Overall CAPEX (k€)	Turbine CF	Wind Farm CF	LCOE (€/MWh)
RWT - 10MW	338	4515	31000	0.507	0.430	91.93
SC MgB2-CSI Generator	497	4643	31210	0.511	0.433	91.60
PDD Generator	346	3922	30080	0.514	0.435	89.01
OFFSHORE SUPPORT STRUCT	Component Mass (tn)	Component Cost (k€)	Overall CAPEX (k€)	Turbine CF	Wind Farm CF	LCOE (€/MWh)
RWT - 10MW	1920	9497	31000	0.507	0.430	91.93
Advanced Jacket		8100	29600			89.20
Semi-Sub Floater Design	3745	12540	34040			97.89
COMBINATIONS			Overall CAPEX (k€)	Turbine CF	Wind Farm CF	LCOE (€/MWh)
RWT - 10MW			31000	0.507	0.430	91.93
LIR + PMDD + Adv. Jacket			29650	0.549	0.473	81.37
2B R1.12+PMDD+Adv.Jacket			28070	0.553	0.469	79.94
BTC/ITC+ PMDD + Adv. Jacket			28980	0.545	0.461	81.98

Table 12.2 – Percentage improvement of PIs in comparison to the 10MW RWT

ROTOR	Component Mass (Δ%)	Component Cost (Δ%)	Overall CAPEX (Δ%)	Turbine CF (Δ%)	Wind Farm CF (Δ%)	LCOE (Δ%)
Low Induction Rotor	7.9%	15.4%	3.8%	7.5%	9.1%	-6.0%
Two-Bladed Rotor R1.08	-20.9%	-19.4%	-1.6%	4.7%	4.7%	-5.3%
Two-Bladed Rotor R1.12	-4.1%	-4.0%	-0.3%	8.3%	8.1%	-7.6%
Smart Rotor (Flaps)	-10.7%	-6.5%	-0.5%	0.2%	0.2%	-0.5%
Carbon Truss Blade Structure	-25.7%	-13.2%	-0.9%	0.0%	0.0%	-0.6%
Bend-Twist Coupled Rotor	-2.0%	-2.0%	-1.2%	0.0%	0.0%	-0.8%
Integrated BTC with IPC	18.4%	18.5%	1.0%	7.5%	7.2%	-6.1%
DRIVE TRAIN & NACELLE	Component Mass (Δ%)	Component Cost (Δ%)	Overall CAPEX (Δ%)	Turbine CF (Δ%)	Wind Farm CF (Δ%)	LCOE (Δ%)
SC MgB2-CSI Generator	47.2%	2.8%	0.7%	0.8%	0.7%	-0.4%
PDD Generator	2.5%	-13.1%	-3.0%	1.4%	1.2%	-3.2%
OFFSHORE SUPPORT STRUCT	Component Mass (Δ%)	Component Cost (Δ%)	Overall CAPEX (Δ%)	Turbine CF (Δ%)	Wind Farm CF (Δ%)	LCOE (Δ%)
Bottom-Mounted OSS		-14.7%	-4.5%			-3.0%
Semi-Sub Floater Design	95.1%	32.0%	9.8%			6.5%
COMBINATIONS			Overall CAPEX (Δ%)	Turbine CF (Δ%)	Wind Farm CF (Δ%)	LCOE (Δ%)
LIR + PMDD + Adv. Jacket			-4.4%	8.3%	10.0%	-11.5%
2B R1.12+PMDD+Adv.Jacket			-9.5%	9.1%	9.1%	-13.0%
BTC/ITC+ PMDD + Adv. Jacket			-6.5%	8.9%	8.4%	-10.8%

12.1 Blade Concepts

LIR concept (Chapter 2)

The new hybrid (glass-carbon) blade is heavier (7%) and more expensive (15%) than the RWT blade. This is due to its longer span and the use of expensive carbon. Nevertheless, the overall increase in turbine CAPEX is less than 4% because in offshore wind the blades represent a small fraction of the turbine and support structure cost. Despite the higher CAPEX the larger, less loaded rotor, increases the turbine yield (capacity factor CF) by 7.5%. As stated earlier, a 4.5% comes from the LIR planform and another 3% from the dedicated low lift profiles. Even more important is the increase of the wind farm capacity factor by 9.1% due to the lower wake losses of LIR rotors. This is the highest value achieved among the different rotor concepts. Overall, LIR promises a 6% reduction of LCOE. This number could be further improved if a cheaper, all-glass LIR blade, could be designed using the integrated techniques developed in the project.

2-Bladed Designs (Chapter 3)

Here both 2-Bladed designs of different blade length R1.08 and R1.12 are discussed. They are all-glass blades derived from an integrated design exercise using aero-structural optimization. Contrary to the LIR they are both high Cp_max designs. The smaller blade (R1.08) is significantly lighter (21%) and cheaper (19%) from the RWT blade. This is however translated to only 1.6% CAPEX reduction. Its lower span yields a 4.7% improvement of wind turbine and wind farm capacity factor and a 5.3% reduction of LCOE. The larger blade (R1.12) is still 4% lighter and cheaper than the reference blade but also has 8.3% and 8.1% higher turbine and farm capacity factors, leading to an overall LCOE

reduction of 7.6%. This is the highest reduction value achieved among the different blade designs studied. It is noted however that this improvement does not take account of the extra wake losses due to the larger diameter of the rotor. If wake losses were proportionally increased by 12% then the R1.12 LCOE reduction would drop to 6.5% from 7.6% but this would still be the larger improvement attained.

Smart Rotor with Flaps (Chapter 4)

The all-glass smart blade with active flaps over 30% of its outer span, designed with advanced integrated design techniques, is satisfying the RWT load envelopes having an 11% less mass than the reference blade. Assuming a cost burden of 5% for the integration of the flap the blade structure the smart blade is 6.5% cheaper than the reference. As long as the rotor radius is maintained and the energy yield gains are marginal (0.2% for both turbine and wind farm capacity factor) the impact in LCOE reduction is rather small, 0.5%. These figures do not take account of possible penalization of the turbine reliability, which besides the increasing direct maintenance costs would compromise its availability and energy yield. On the other hand, the smart blade could have a large benefit in reducing costs of downstream fatigue -driven components, like the jacket, if a reduction of fatigue loading of such components can be demonstrated.

Truss inner-blade Structure (Chapter 5)

The expected benefits in terms of PIs are rather small for the Glass/Epoxy design, so we shall limit our discussion to the Carbon/Epoxy alternative. It is clear in this design but also in other blade designs that maintain the rotor radius of the RWT that no significant improvement is expected in regard to capacity factors and LCOE and the benefits are related to the reduction of the blade mass and cost. Indeed, a 26% reduction in blade mass is achieved which is the largest among the different blade concepts studied. On the other hand, the blade cost seems to decrease by 13% but this is a highly uncertain result since the manufacturing cost for the build-up of internal truss structures, including the joints of the truss members, is pretty unknown.

Bend-Twist Coupled Rotor (Chapter 6)

The conclusions here regarding the impact of the BTC concept on LCOE are similar to those extracted for Chapter 5. No real improvement in the cost of energy is expected maintaining the reference rotor diameter. Such designs may reduce the fatigue loading of the blade itself but, also, of the support structure having an indirect effect on CAPEX reduction which is not studied in the present context. The BTC blade is highly loaded (high Cp_max design) and 2% lighter and cheaper than the RWT blade. The overall CAPEX and LCOE improvement is small.

Integrated Design of a BTC Blade with IPC (Chapter 7)

Here a longer than the RWT all-glass blade is designed with an integrated design method using aero-structural optimization. The blade has BTC capabilities and further load reduction is succeeded by employing Individual Pitch Control. Contrary to the LIR this is also a high Cp_max design. The resulting blade is 18.5% heavier and most expensive than the RWT blade. This is however translated to only 1% CAPEX increase. It promises a 7.5% and 7.2% improvement of wind turbine and wind farm capacity factor respectively and a 6.1% reduction of LCOE. It is noted that the LCOE improvement does not take account of the extra wake losses due to the larger diameter of the rotor.

12.2 Drive Train Concepts

Superconducting Generator (Chapter 8)
The 10MW MgB2 superconductor generator combined with a high efficiency Current Source Inverter (CSI) power electronics option is considered in the tables above. To reduce the SC cost the heavy design alternative IT (iron teeth) has been considered in the present context. This design leads to a small only increase of the drive train cost (0.8%) but due to the large SC weight (300tn, almost double from the reference) the overall nacelle-drive train mass increases by 47%. Alternative lightweight designs with less iron and more SC material have been shown to be very expensive with current SC prices. The highly efficient power electronics seem to compensate the power losses due to machine cooling and combined with the generator efficiency lead to a slight increase (0.8%) of the turbine capacity factor. The overall effect promises a small reduction (0.4%) of LCOE compared to the 10MW RWT.

Magnetic Pseudo Direct Drive (PDD) (Chapter 9)
The PDD generator with highly efficient power electronics promises a good LCOE performance (3.2% lower than the reference) combined with a significant nacelle/drive train cost reduction of 13%. The nacelle mass is slightly increased by 2.5% while the turbine capacity factor increases by 1.4% which, along with the reduced CAPEX, is the reason of LCOE improvement. The improved capacity factor comes as a combination of the highly efficient PDD generator (98.7% at full load) and the highly efficient power electronics.

12.3 Support Structure Concepts

Bottom Mounted Offshore Support Structure (Chapter 10)
An advanced design/manufacturing of the 10MW RWT jacket is expected to reduce the original cost of 9.5 M€ by at least 15%. Such a reduction would decrease the overall CAPEX by 4.5% translated to 3% reduction of the LCOE.

Semi-Sub Floater Design (Chapter 11)
An asymmetric semi-submersible floater platform from steel, designed for a sea depth of 200m, has been presented. This design seems to be more mature and detailed compared to other competing concepts and it is therefore adopted as the Reference 10MW Floater of the project. Moving the RWT from its jacket to the reference floater would result in a 32% increase of the support structure cost that burdens the overall CAPEX by 9.8%. This would lead to a 6.5% increase of LCOE compared to its reference value.

12.4 Combination of Innovative Concepts and Overall Expectations

A simplified methodology for estimating the combined performance of the researched concepts would sum-up the percentage gains of the individual components. Some examples of such combinations are given in the lower parts of the PI Tables.

For bottom mounted designs at INNWIND.EU 10MW RWT conditions the following expectations regarding LCOE reduction look reasonable:

- Rotors with conventional inner structure 7%
- Advanced inner structure (BTC, carbon truss) 1%
- Drive train (reduced CAPEX, increased efficiency) 3%
- Advanced Jacket 3%

Expected Overall LCOE reduction 14%

Starting from the EWII LCOE value of 106.93 €/MWh corresponding to 5MW turbine sizes this number dropped at 91.93 €/MWh (16% reduction) for the 10MW RWT. This reduction was due to the larger turbine size along with the use of a lightweight rotor with thick profiles and the shift from traditional three-stage geared drive trains to medium speed single-stage drive. The additional 14% reduction of LCOE, due to the advanced concepts researched in INNWIND.EU is getting LCOE close to 80 €/MWh. This corresponds to an overall reduction of more than 30% compared to the EWII value.

For floating designs the picture is less clear for the moment. The reference floater itself increases LCOE by 6.5%. Employing the rotor and drive train innovations would result to an overall 7.5% LCOE reduction. Further improvement should come from the reduction of the floater cost. For doing that we shall first need to investigate the floater mass/cost sensitivity to the RNA (rotor-nacelle-assembly) mass and the wind turbine size. The RNA sensitivity should be studied taking account of the system natural frequencies and stability constraints that drive the design of floaters. If the cost – RNA mass sensitivity is high, design options (such as 2Bladed concepts, advanced inner blade structures, active flaps and more expensive, lightweight, superconducting generators) that have the potential of large RNA mass reductions are becoming more promising.

REFERENCES

[1] *Chaviaropoulos, T; H.J.M. Beurskens and S. Voutsinas, Moving towards large(r) high speed rotors – is that a good idea? Proc. Scientific Track, EWEA 2013 Conference, Vienna..*

[2] *P.K. Chaviaropoulos and G. Sieros, "Design of Low Induction Rotors for use in large offshore wind farms", Proc. Scientific Track, EWEA 2014, Barcelona..*

[3] *INNWIND.EU Deliverable 2.12.*

[4] *INNWIND.EU Del 1.22.*

[5] *Chaviaropoulos P, Costs Models v1.01 Oct 2014.xlsx D1.23.*

[6] D. J. Lekou, "Scaling Limits and Costs regarding WT blades," , UPWIND (SES6) 019945, WP3 Deliverable Report D3.4.3, http://www.upwind.eu/publications/3-rotor-structure-and-materials.aspx, 2010.

[7] T. C. Inc., "Cost study for large wind turbine blades: WindPact Blade system design studies," SANDIA report, SAND2003-1428, 2003.

[8] *New aerodynamics rotor concepts specifically for very large offshore wind turbines, Edited by H.A. Madsen, L. Bergami and F. Rasmussen. INNWIND.EU D2.11 Deliverable, Sept 2013.*

[9] *http://hawcstab2.vindenergi.dtu.dk.*

[10] *http://openmdao.org.*

[11] *http://fusedwind.org.*

[12] *Hansen, M. H., Aeroelastic stability analysis of wind turbines using an eigenvalue approach, Wind Energy, 7:133-143, 2004.*

[13] *[Tibaldi C., Henriksen L., Hansen M.H., Bak C., Wind turbine fatigue damage evaluation based on a linear model and a spectral method. Accepted for publication on Wind Energy 2015..*

[14] *Barlas, T. K. and van Kuik, G. A. M., Review of state of the art in smart rotor control research for wind turbines, Progress in Aerospace Sciences — 2010, Volume 46, Issue 1, pp. 1-27, 2010.*

[15] *Bergami, L., Adaptive Trailing Edge Flaps for Active Load Alleviation in a Smart Rotor Configuration, PhD thesis, DTU Wind Energy, 2013.*

[16] *Madsen, H. A. et al., Towards an industrial manufactured morphing trailing edge flap system for wind turbines, Proceedings of EWEC 2014, Barcelona, Spain, 2014.*

[17] *Bak, C. et al Description of the DTU 10 MW Reference Wind Turbine, Technical report, DTU Vindenergi-I-0092, 2013.*

[18] *Zahle, F., Tibaldi, C., Verelst, D. R., Bak, C., Bitche, R., and Blasques, J. P. A. A., Aero-Elastic Optimization of a 10MW Wind Turbine, Proceedings of the 33rd Wind Energy Symposium , Kissimmee, Florida, U.S.A., 2015.*

[19] *http://openmdao.org.*

[20] *Gill PE, Murray W, Saunders MA. SNOPT: An SQP algorithm for large-scale constrained optimization (reprinted from SIAM journal optimization, vol 12, pg 979-1006, 2002). Siam Review 2005; 47(1):99{131.*

[21] *Gill PE, Murray W, Saunders MA. SNOPT 7 user's guide. Technical Report Numerical Analysis Report NA 04-1, Department of Mathematics, University of California, 2008..*

[22] *http://fusedwind.org.*

[23] *Blasques, P., User s Manual for BECAS A cross section analysis tool for anisotropic and inhomogeneous beam sections of arbitrary geometry, 2012.*

[24] *Blasques, J. P. and Stolpe, M., Multi-material topology optimization of laminated composite beam cross sections, Composite Structures,94(11), 3278-3289, 2012.*

[25] *http://becas.dtu.dk.*

[26] *Hansen, M. H., Aeroelastic stability analysis of wind turbines using an eigenvalue approach, Wind Energy, 7:133-143, 2004.*

[27] *http://hawcstab2.vindenergi.dtu.dk.*

[28] *Tibaldi, C., Concurrent Aeroservoelastic Design and Optimization of Wind Turbines, PhD Thesis, DTU Wind Energy,2015.*

[29] *Tibaldi C., Henriksen L., Hansen M.H., Bak C., Wind turbine fatigue damage evaluation based on a linear model and a spectral method. Accepted for pubblication on Wind Energy 2015.*

[30] *Bergami, L. and Hansen M. H., A Linear Time Invariant Model of a Smart Rotor with Adaptive Trailing Edge Flaps, Wind Energy, to appear.*

[31] *IEC. IEC 61400-1. Wind turbines – Part 1: Design Requirements, 2005.*

[32] *Veers PS, Bir G, Lobitz DW. Aeroelastic tailoring in wind-turbine blade application. Windpower '98, AWEA Annual Conference and Exhibition, Bakersfield, CA, April 27 – May 1, 1998..*

[33] *Lobitz DW, Veers PS, Eisler GR, Laino DJ, Migliore PG, Bir G. The Use of Twist-Coupled Blades to Enhance the Performance of Horizontal Axis Wind Turbines. Sandia Report SAND 2001-1303, Sandia National Laboratories, Albuquerque, NM, May 2001..*

[34] *Lobitz DW, Laino DJ. Load mitigation with twist-coupled HAWAT blades. '99 ASME Wind Energy Symposium, Reno, January 11–14, 1999..*

[35] *Lobitz D, Veers PS, Laino D. Performance of twist-coupled blades on variable speed rotors. AIAA 2000-0062, 2000 ASME Wind Energy Symposium, Reno, January 10–13, 2000..*

[36] *Bottasso C.L., Campagnolo F., Croce A., Tibaldi C., "Optimization-based study of bend–twist coupled rotor blades for passive and integrated passive/active load alleviation", Wind Energy, Vol. 16, N.8, p1149-1166, 2013. DOI: 10.1002/we.1543 (2013)..*

[37] *Bottasso C.L., Campagnolo F., Croce A., "Multi-Disciplinary Constrained Optimization of Wind Turbines", Multibody System Dynamics, Vol. 27, N. 1, p. 21-53, 2012, ISSN: 1384-5640, doi: 10.1007/s11044-011-9271-x (2012)..*

[38] *Bottasso C.L., Campagnolo F., Croce A., Dilli S., Gualdoni F., Nielsen M.B., "Structural optimization of wind turbine rotor blades by multi-level sectional/multibody/3DFEM analysis", Multibody System Dynamics, Vol. 32, N. 1, 2014, p. 87-116, doi:10.1007/s.*

[39] *Giavotto V, Borri M, Mantegazza P, Ghiringhelli GL. Anisotropic beam theory and applications. Computers & Structures 1983; 16:403–413..*

[40] *Bauchau OA. Flexible Multibody Dynamics. Springer, Solid Mechanics and its Applications, Vol. 176, 2011..*

[41] *Bauchau OA, Bottasso CL, Trainelli L. Robust integration schemes for flexible multibody systems. Computer Methods in Applied Mechanics and Engineering 2003; 192:395–420..*

[42] *Bottasso CL, Croce A. Cp-Lambda: User's Manual. Dipartimento di Ingegneria Aerospaziale, Politecnico di Milano, 2006–2011..*

[43] *Bishop N.W.M, Sherratt F., "Finite Element Based Fatigue Calculations". NAFEMS, (2000)..*

[44] *Germanischer Lloyd, Guideline for the certification of wind turbines, 2010.*

[45] *Philippidis, T. P. and Vassilopoulos, A. P., "Complex stress state effect on fatigue life of GRP laminates. Part I, experimental," International Journal of Fatigue, 24 813-823, (2002)..*

[46] *Philippidis, T. P. and Vassilopoulos, A. P., "Complex stress state effect on fatigue life of GRP laminates. Part II, theoretical formulation," International Journal of Fatigue, 24 825-830 , (2002)..*

[47] *Lekou DJ, "Information on the Benchmark of blade structural FATIGUE models", InnWind.EU Report, July 2014.*

[48] *Lekou DJ, Chortis D, Belen Fariñas A, Amézqueta C, Nuin I, Pavese C, Berring P, Branner K, Bottasso CL, Croce A, Gualdoni F, Philippidis TP, Masmanidis IT, Roukis GA, de Winkel GD, Dekker H, Benchmarked aerodynamic-structural design methods: Part A "Resul.*

[49] *Duràn Lucas Oscar. Influence of cost of energy models on wind turbine rotor design. 2015.*

[50] *Bossanyi E. Individual blade pitch control for load reduction. Wind Energy 2003; 6:119–128..*

[51] *Bossanyi E. Wind turbine control for load reduction. Wind Energy 2003; 6:229–244..*

[52] *Bossanyi E. Developments in individual blade pitch control. The Science of Making Torque from Wind, Delft, The Netherlands, April 19–21, 2004..*

[53] *Bossanyi E. Further load reductions with individual pitch control. Wind Energy 2005; 8:481–485..*

[54] *van Engelen T. Design model and load reduction assessment for multi-rotational model individual pitch control. European Wind Energy Conference (EWEC 2006), Athens, Greece, February 27 – March 1, 2006.*

[55] *Geyler M, Caselitz P. Individual blade pitch control design for load reduction on large wind turbines. European Wind Energy Conference (EWEC 2007), Milano, Italy, May 7–10, 2007..*

[56] *Kanev S, van Engelen T. Exploring the limits in individual pitch control. European Wind Energy Conference (EWEC 2009), Marseille, France, March 16–19, 2009..*

[57] *Leithead W, Neilson V, Dominguez S. Alleviation of unbalanced rotor loads by single blade controllers. European Wind Energy Conference (EWEC 2009), Marseille, France, March 16–19, 2009..*

[58] *A.Croce, Deliverable D2_22_PoliMI_16July2015.txt.*

[59] *Bottasso C.L., Campagnolo F., Croce A., Tibaldi C., "Optimization-based study of bend–twist coupled rotor blades for passive and integrated passive/active load alleviation", Wind Energy, Vol. 16, N.8, p1149-1166, 2013. DOI: 10.1002/we.1543 (2013)..*

[60] *B.B. Jensen, N. Mijatovic and A.B. Abrahamsen, "Development of superconducting wind turbine generators", J. Renewable Sustainable Energy 5, 023137 (2013).*

[61] *R. Fair et. al., "Superconductivity for Large Scale Wind Turbines", General Electric – Global Research, DOE report DE-EE0005143, 2012.*

[62] C. Bak, F. Zahle, R. Bitsche, T. Kim, A. Yde, L. Henriksen, P. Andersen, A. Natarajan and M. Hansen, "Description of the DTU 10 MW Reference Wind Turbine," D1.21 INNWIND.EU, 2013.

[63] *A.B. Abrahamsen et. al., "Design study of a 10 MW MgB2 superconductor direct drive wind turbine generator", Poster presented EWEA 2014.*

[64] *Henk Polinder et. al., "Trends in Wind Turbine Generator Systems", IEEE JOURNAL OF EMERGING AND SELECTED TOPICS IN POWER ELECTRONICS, VOL. 1, NO. 3 (2013).*

[65] *A.B. Abrahamsen et. al., "Design of an MgB2 race track coil for a wind generator pole demonstration", Journal of Physics: Conference Series 507 (2014) 032001.*

[66] *D. Liu et. al., "Comparison of 10 MW Superconducting Generator Topologies for Direct-Drive Wind Turbines", Conference paper submitted to IEEE International Electric Machines & Drives Conference (IEMDC) 2015.*

[67] *D. Liu et. al.," Ripple Field AC Losses in 10 MW Wind Turbine Generators with a MgB2 Superconducting Field Winding", paper submitted as part of European Conference on Applied Superconductivity EUCAS(2015)..*

[68] *F. Deng et. al., "Converter designs tailored to SC and PDD concepts", INNWIND.EU Deliverable D3.31 (2015)..*

[69] *J. Wang et. al., "Design of a Superconducting Synchronous Generator with LTS Field Windings for 12 MW Offshore Direct-Drive Wind Turbines," IEEE Trans. Ind. Electron., vol. 0046, no. c, pp. 1-1, 2015.*

[70] *G. Shrestha, "Structural Flexibility of Large Direct Drive Generators for Wind Turbines", PhD Thesis, Delft University of Technology (2013)..*

[71] *Ewoud Stehouwer, "Mechanical Integration: Scaling to 20 MW", work-package presentation at INNWIND.EU meeting in Hamburg (2014).*

[72] *Richard Clark, Stuart Calverley, Andrew Myers, "DRAFT report, Subtask 3.2.2", INNWIND.EU deliverable D3.22 (2015).*

[73] *A. Penzkofer and K. Atallah, "Final report, Subtask 3.2.1", INNWIND.EU deliverable D3.21 (2015).*

[74] *Dong Liu, A. B. Abrahamsen, H. Polinder, et. al., "Deliverable D3.42 First assessment of performance indicators of SC and PDD generators", INNWIND.EU, WP3 internal report, Sept 2013.*

[75] "Deliverable D4.31, Design Report Reference Jacket, INNWIND.EU, 2013".

[76] "DNV-OS-J101: Design of Offshore Wind Turbine Structures, Det Norske Veritas, January 2013".

[77] "DNV-RP C203: DNV Recommended Practice – Fatigue Design of Offshore Steel Constructions, Det Norske Veritas, October 2012".

[78] "Deliverable 4.12, Innovations on component level, INNWIND.EU, 2014".

[79] S. Voutsinas, D. Manolas, F. Lemmer, Y. Wei, D. Matha, E. Grela, J. Azcona, X. Munduate and A. Natarajan, Innovative Concepts for Floating Structures, INNWIND.EU deliverable 4.33, 2015.

[80] F. Sandner and D. Matha, "Innovative Floating Platforms for Wind Turbines: Conceptual Design Stages," 10.Material cost estimation, pp.10, 4.07.2014.

[81] DNV, "DNV OS c103 Structural Design of Column Stabilised Units".

[82] DNV, "DNV OS j101 Design of Offshore Wind Turbines Structures," 2010.

[83] DNV, "DNV-OS-J103 Design of Floating Wind Turbine Structures," 2013.

[84] *Chaviaropoulos, P. K. and Douvikas, D. I., 1998, "Mean-flow-field Simulations over Complex Terrain Using a 3D Reynolds Averaged Navier–Stokes Solver," Proceedings of ECCOMAS '98, Vol. I, Part II, pp. 842-848.*

[85] *Voutsinas, S.G., 2006 "Vortex Methods in Aeronautics: How to make things work", Int. Journal of Computational Fluid Dynamics, Vol 20, No 1.*

[86] *Wilcox, D.C., 1993, "Turbulence Modelling for CFD", DCW Industries Inc., La Canada, California, IBSN 0-9636051-0-0..*

[87] *Riziotis, V.A., Voutsinas, S.,G., "Dynamic stall modeling on airfoils based on strong viscous-inviscid interaction coupling," Int. J. Numer. Meth. Fluids, 56, 185-208, 2008.*

[88] *P. Chaviaropoulos et al., "PI-based assessment of innovative concepts (methodology)", Innwind.EU Deliverable 1.23, April 2014.*

[89] "P.K. Chaviaropoulos and G. Sieros, "Design of Low Induction Rotors for use in large offshore wind farms", Proc. Scientific Track, EWEA 2014, Barcelona".

[90] O. M. Faltinsen, "Sea loads on ships and offshore structures," Cambridge Ocean Technology Series.

[91] Wamit, "Wamit User Manual 6.4".

[92] A. Robertson and J. Jonkman, "Definition of the Semisubmersible Floating System for Phase II of OC4".

[93] S. Chakrabarti, Handbook of offshore Engineering Volume 2, Elsevier, 2005.

[94] DNV, "DNV =S C101 Design of Offshore Steel Structures, General (LRFD Method)".

[95] VDI, "VDI 2221 - Methodik zum Entwickeln und Konstruieren technischer Systeme und Produkte".

[96] K. Suzuki, H. Yamaguchi, M. Akase, A. Imakita, T. Ishihara, Y. Fukumoto and T. Oyama, "Initial Design of Tension Leg Platform for Offshore Wind Farm," *Journal of Fluid Science and Technology,* vol. 6, no. 3, pp. 372-381, 2011.

[97] F. Sandner, D. Schlipf, D. Matha and P. W. Cheng, "Integrated Optimization Of Floating Wind Turbine Systems," in *Proceedings of the 33rd International Conference on Ocean, Offshore and Arctic Engineering OMAE*, San Francisco, 2014.

[98] A. Robertson, J. Jonkman, M. M, H. Song, A. Goupee, A. Coulling and C. Luan, "Definition of the Semisubmersible Floating System for Phase II of OC4," 2013.

[99] C. Molins, A. Campos, F. Sandner and D. Matha, "Monolithic Concrete Off-Shore Floating Structure For Wind Turbines," in *Proceedings of the EWEA*, 2014.

[100] M. E. McCormick, Ocean Engineering Mechanics, Oxford University Press, 2010.

[101] D. Matha, "Model Development and Loads Analysis of an Offshore Wind Turbine on a Tension Leg Platform with a Comparison to Other Floating Turbine Concepts," 2009.

[102] R. Lupton and R. Langley, "Efficient modelling of floating wind turbines," in *Proceedings of 9th PhD Seminar on Wind Energy in Europe*, Visby, 2013.

[103] T. J. Larsen and A. M. Hansen, "How to HAWC2, the user's manual.," Tech. Rep. Risø-R-1597(ver.4-3) (EN), DTU Wind Energy, Roskilde, Denmark, May 2012.

[104] M. I. Kvittem, E. Bachynski and T. Moan, "Effects of Hydrodynamic Modelling in Fully Coupled Simulations of a Semi-submersible Wind Turbine," *Energy Procedia,* vol. 24, no. January, pp. 351-362, #jan# 2012.

[105] M. Karimirad and T. Moan, "A Simplified Method for Coupled Analysis of Floating Offshore Wind Turbines," *Journal of Marine Structures,* vol. (Submitted, 2012.

[106] J.Jonkman, S.Butterfield, W.Musial and G. Scott, "Definition of a 5-MW Reference Wind Turbine for Offshore System Development," NREL Technical Report TP-500-38060, February, 2009.

[107] K. Iijima, M. Kawai, Y. Nihei, M. Murai and T. Ikoma, "Conceptual Design Of A Single-Point-Moored Fowt And Tank Test For Its Motion Characteristics," 2013.

[108] F. Huijs, J. Mikx, F. Savenije and E.-J. d. Ridder, "Integrated design of floater, mooring and control system for a semi-submersible floating wind turbine," *Proceedings of the EWEA Offshore,* 2014.

[109] S. Y. Hong, J. H. Kim, S. W. Hong and . H. J. Kim, "Design and Analysis of a Box Floater with Damping Plates for Floating Wind Turbine Platform," vol. 4, pp. 411-416, 2012.

[110] T. I. Fossen, Handbook of Marine Craft Hydrodynamics and Motion Control, vol. First Edit, John Wiley & Sons, 2011.

[111] T. Fischer, W. de Vries and B. Schmidth, "Upwind Design Basis," 2010.

[112] J. Fernandez, A. Laidler, J. Izarra, M. Innovation, D. Murueta and B. Malloape, "Design considerations of a Semisubmersible Platform for Offshore Wind Turbines," in *Proceedings of the EWEA Offshore*, 2013.

[113] R. W. Copple and C. Capanoglu, "Tension Leg Wind Turbine (TLWT) Conceptual Design Suitable for a Wide Range of Water Depths," vol. 4, pp. 396-403, 2012.

[114] P. Chaviaropoulos, H. C. Karga and B. Hendriks, "InnWind.EU D1.2.3: PI-based Assessment of Innovative Concepts," 2014.

[115] P. Chaviaropoulos and A. Natarajan, "InnWind.EU D1.2.2: Definition of Performance Indicators (PIs) and Target Values," 2014.

[116] S. Chakrabarti, Handbook of Offshore Engineering, Volume 1, Elsevier.

[117] S. Butterfield, J. Jonkman and P. P. Sclavounos, "Engineering Challenges for Floating Offshore Wind Turbines," 2007.

[118] T. Burton, N. Jenkins, D. Sharpe and E. Bossanyi, Wind Energy Handbook, 2nd ed., Wiley, Ed., Wiley, 2011.

[119] G. Betti, M. Farina, G. Guagliardi, A. Marzorati and R. Scattolini, "Development and Validation of a Control-Oriented Model of Floating Wind Turbines," *IEEE Transactions on Control Systems Technology,* 2012.

[120] A. Babarit, "NEMOH," Laboratoire de recherche en Hydrodynamique, Énergétique et Environnement Atmosphérique, [Online]. Available: http://lheea.ec-nantes.fr/doku.php/emo/nemoh/start. [Accessed 20 07 2014].

[121] E. J. Azcona, "State-of-the-art and implementation of design tools for floating structures," INNWIND D4.21, 2013.

[122] A. Aubault, C. Cermelli and D. Roddier, "Parametric Optimization of a Semi-Submersible

Platform With Heave Plates," in *Volume 1: Offshore Technology; Special Symposium on Ocean Measurements and Their Influence on Design*, 2007.

[123] Ansys, *AQWA User Manual,* vol. 15317, 2011, pp. 724-746.

[124] Norwegian Petroleum Directorate, "Norwegian Petroleum Directorate," Norwegian Petroleum Directorate, 2014. [Online]. Available: http://www.npd.no/en/. [Accessed 30 07 2014].

[125] "INNWIND.EU Project Deliverable report 4.12," Aug. 2014.

[126] F. Lemmer, S. Raach, D. Schlipf and P. W. Cheng, "Prospects of Linear Model Predictive Control on a 10MW Floating Wind Turbine," in *Proceedings of the ASME 34th International Conference on Ocean, Offshore and Arctic Engineering*, St. John's/Canada, 2015.